Dendritic integration in olfactory bulb granule cells:

Thresholds for lateral inhibition and role of active conductances upon 3D multi-site photostimulation of spines using a holographic projector module

Dissertation

Zur Erlangung des Doktorgrades der Naturwissenschaften (Dr. rer. nat.) der Fakultät für Biologie und Vorklinische Medizin der Universität Regensburg

Vorgelegt von
Max Müller
aus Nördlingen

Januar 2020

Das Promotionsgesuch wurde eingereicht am
Die Arbeit wurde angeleitet von Prof. Dr. Veronica Egger.

Unterschrift:

Kurzfassung der Arbeit

Die GABAergen inhibitorischen axonlosen Körnerzellen (GCs) bilden über lange Dornfortsätze (Spines) reziproke dendrodendritische Synapsen mit Mitral- und Büschelzellen (MC/TCs), den wichtigsten Projektionsneuronen des Riechkolbens von Säugern (*Bulbus Olfactorius*, OB), aus. Diese Synapsen vermitteln die Selbstinhibition von und laterale Inhibition zwischen MC/TCs. Diese dient der Kontrastverstärkung zwischen ähnlichen Geruchssignalen und der Synchronisation oszillatorischer Aktivität. GCs sind also wesentlich an der Geruchssignalverarbeitung beteiligt. GC-Dendriten sind auf vielfältige Weise hoch erregbar: Synaptische Inputs an einzelnen Spines können Natrium (Na^+)-vermittelte Zacken im Membranpotential (Spikes) erzeugen, die auf den Kopf des Spines begrenzt sind und zur reziproken Ausschüttung des Neurotransmitters GABA führen. Eine stärkere Aktivierung führt zu einer globalen Ausbreitung dendritischer Signale, die sowohl niederschwellige Kalzium (Ca^{2+})-Spikes als auch Na^+-Spikes umfassen.

Da das Erreichen der globalen Schwellenpotentiale gleichzeitig das Erreichen der Schwelle zu lateraler Inhibition bedeutet, war das Ziel meiner Arbeit, den genauen Übergang von der lokalen zur globalen Signalgebung zu untersuchen: Wie viele Spines, in welcher Position und Verteilung auf dem dendritischen Baum, müssen aktiviert werden, um globale Spikes auszulösen und was sind die molekularen Hauptakteure, sprich welche Ionenkanäle sind beteiligt.

Um dies optimal zu untersuchen, haben wir im ersten Teil meiner Arbeit einen holographischen Projektor in das bestehende kommerzielle zwei-Photonen (2P) Galvanometer-basierte 2D-Laser-Scanning-Mikroskop mit einer Uncaging-Einheit (Uncaging: Aktivierung photolabiler biologisch inaktiver Derivate von Neurotransmittern mittels Photolyse) implementiert, der die gleichzeitige Photostimulation mehrerer Spines in drei Dimensionen (3D) in akuten Hirnschnitten ermöglicht. 2P-Uncaging in definierten Mustern mittels holographischer Illumination ist eine leistungsfähige Methode zur Untersuchung neuronaler Funktion, da sie in der Lage ist, mehrere synaptische Inputs in verschiedenen Brennebenen gleichzeitig zu emulieren. Wie bei jedem optischen System haben jedoch auch holographische Projektoren ein begrenztes Produkt aus Raum und Bandbreite, was den räumlichen Bereich – oder das Sichtfeld (FOV) – definierter Illumination für eine gewünschte Auflösung einschränkt. Dieser Kompromiss zwischen holographischem FOV und

Auflösung schränkt die Reichweite hochauflösender 2P-Uncaging an Spines auf einzelne Teile des dendritischen Baums ein. Wir erweitern das zugängliche FOV, indem wir mit Hilfe der Galvanometer-Scannerspiegel das holographische FOV beliebig über das abbildende FOV positionieren. Das Projektor-System nutzt die im Mikroskop integrierten Bildfunktionen. Die genauen Positionen der Stimulationspunkte können innerhalb eines erfassten 3D-Bildstapels ausgewählt werden (das Volumen von Interesse, VOI). Der holographische Projektor erzeugt dann 3D-Illuminationsmuster mit Hilfe von mehreren Uncaging Fokussen. Das bildgebende FOV unseres Systems ist 800×800 μm^2, innerhalb dessen ein holographisches VOI von 70×70×70 μm^3 an beliebigen Positionen ausgewählt und auch während des Experiments bewegt werden kann, ohne die Probe selbst zu bewegen. Wir beschreiben detailliert das Design und das Laserausrichtungsprotokoll sowie das individuell angepasste Software-Plugin, das die 3D-Positionierung von Stimulationspunkten steuert. Um die neurobiologische Anwendung grundsätzlich zu demonstrieren, habe ich die Funktion des holographischen Systems zuerst durch Photolyse von „caged" Glutamat an den Spines entlang der basalen Dendriten kortikaler Pyramidenzellen (PC) in Hirnschnitten junger Ratten getestet. Über Patchpipetten am Zellkörper (Soma) wurden die Zellen mit kalziumempfindlichem Fluoreszenzfarbstoff (OGB-1) gefüllt und elektrische Potentiale aufgezeichnet. Simultanes Uncaging von Glutamat an mehreren Spines führte zur supralinearen Summation postsynaptischer Potentiale am Soma und schließlich zu Aktionspotentialen. Gleichzeitig zeigte ich die Möglichkeit einer 2P-Ca^{2+}-Bildgebung in 2D im Dendriten und ausgewählten Spines, um damit synaptischen Ca^{2+} Einfluss, sowie lokale regenerative Ereignisse wie lokale dendritische Spikes aufzuzeichnen.

Im zweiten Teil meiner Arbeit wendete ich das System zur Untersuchung dendritischer Integration in GCs an. Wir stellten fest, dass weniger als 10 simultan aktivierte dendrodendritische Spines ausreichen, um lokale und globale dendritische Signale zu erzeugen, die auch lokale Ca^{2+}-Spikes und Na^{+}-Spikes (D-spikes) beinhalten. Obwohl das GC-Ruhepotential im Vergleich zu PCs um ca. -10 mV hyperpolarisiert ist, benötigt das Erreichen des AP-Schwellenpotentials eine ähnliche Anzahl von aktivierten Spines (9,0 ± 1,6 in GCs vs 10 ± 1 in PCs), wobei 5,5 ± 2,1 aktivierte Spines bereits ausreichen, um einen lokalen Ca^{2+}-Spike auszulösen. Die dendritische Integration unterhalb der AP-Schwelle ist meist linear. Bei der Stimulation von 6,5 ±

2,7 Spines zeigten jedoch ~ 65 % der GCs supralineare Integration, wobei häufig D-spikes auftraten. Einzelne Spines können die Übergänge zwischen den drei Spikes durch schrittweise erhöhten Ca^{2+}-Einfluss erfassen, was vermutlich zur Erhöhung der Freisetzungswahrscheinlichkeit von GABA führt. Außerdem bewirken die einzelnen Spikes eine zunehmend größere Ausbreitung im Dendriten, was zeigt, dass GCs, abhängig vom Input, zu kompartmentalisierter und globaler Signalgebung fähig sind. Durch pharmakologisches Blockieren verschiedener Ionenkanäle zeigten wir, dass NMDA-Rezeptoren stark zur aktiven Integration beitragen. Morphologische Parameter und die Verteilung der aktivierten Spines auf dem Dendriten spielen dagegen kaum eine Rolle.

Zusammenfassend ist festzustellen, dass Dendriten von GCs zu komplexen Rechenleistungen fähig und Schwellenwerte für die GC-vermittelte laterale Inhibition niedrig sind.

List of Publications

This cumulative dissertation is composed of the following published or submitted manuscripts, in which I am either first or shared co-first author:

A. Go, M.A., **Mueller, M.**, Castanares, M.L., Egger, V., and Daria, V.R. (2019). A compact holographic projector module for high-resolution 3D multi-site two-photon photostimulation. PLoS One 14, e0210564.

B. **Mueller, M.**, Egger, V. (2020). Dendritic integration in olfactory bulb granule cells: Thresholds for lateral inhibition and role of active conductances upon simultaneous activation. In submission for publication, preprint on BioRxiv.

In the course of this work, I contributed to a further publication, which is not part of the dissertation:

C. Aghvami, S.S., **Mueller, M.**, Araabi, B.N., and Egger, V. (2019). Coincidence Detection within the Excitable Rat Olfactory Bulb Granule Cell Spines. J Neurosci *39*, 584-595.

Personal Contributions

Publication A

The research was designed by myself, Mary Ann Go, Veronica Egger and Vincent R. Daria. Incorporation of the holographic projector module was done by myself, Mary Ann Go and Michael L. Castañares. Development of the custom software was done by Mary Ann Go. Experimental work was done by myself. The work was supervised by Veronica Egger and Vincent R. Daria, and the publication was written by myself, Mary Ann Go, Michael L. Castañares, Veronica Egger and Vincent R. Daria.

Publication B

The research was designed and the experimental work was performed by myself. The work was supervised by Veronica Egger. The publication was written by myself and Veronica Egger.

Publication C

The research was designed by Veronica Egger and Sara S. Aghvami. The experimental work was designed and performed by myself. Simulations were done by Sara S. Aghvami. The work was supervised by Veronica Egger. The publication was written by Sara S. Aghvami and Veronica Egger.

Table of Contents

1 General Introduction

This section is intended to convey the biological principles and functions of the methods used in my thesis. It forms the basis for the introductions in *2.2* and *3.2*.

1.1 Olfaction

In most animals, olfaction plays a central role from the first seconds in life. A rat with anosmia, the loss of the sense of smell, will die as a pup as it is unable to find the mother's nipple (Galizia and Lledo, 2013). Later in life, olfaction is necessary for finding food, avoiding predators, or selecting a mate making it crucial for the survival and fitness of an individual. The human sense of smell is also better and more important than we consciously perceive. In contrast to statements of famous neuroanatomist Paul Broca or neurologist Sigmund Freud that humans are "nonsmellers" or have a "tiny smell", olfaction in humans is generally similar to other mammals in its neurobiology and sensory capabilities. Humans have fewer functional olfactory receptor genes, but our brains have more complex olfactory bulbs and orbitofrontal cortices to interpret the odor information (McGann, 2017). Recent studies suggest that humans can discriminate more than one trillion olfactory stimuli (Bushdid *et al.*, 2014). We rely on our sense of smell to detect dangers, such as fire, poisonous fumes or spoiled food but also, not less important, to enjoy pleasant smells of our environment like food or our fellow human beings. Indeed, most odorants are organic substances, i.e. produced by other living species and anosmia or hyposmia (the reduction of the sense of smell) is associated with emotional diseases like depression (Croy and Hummel, 2017). Additionally, smell dysfunction serves as marker for, or might, through respiratory infections or pollution, even be the earliest stages of neurodegenerative diseases like Alzheimer's or Parkinson's disease (Doty, 2017).

What is the stimulus of olfaction? Odorants are small chemicals released by various substrates and can be perceived by an animal. They range from small molecules such as gases (CO_2 or H_2S), simple aldehydes, esters or nucleotides, to complex molecules or even peptides. Odorants are produced for communication to benefit both, the emitter and the recipient (pheromones), only the emitter (allomone) or only the recipient (kairomone). Odors can have innate meaning or be learnt. They can be single substances or complex mixtures of hundreds of substances distributed

as plumes in a turbulent environment (Galizia and Lledo, 2013). The following chapters deal with how odorants, the stimuli, are picked up from the environment and become a perceived odor in the brain.

1.1.1 From the nasal cavity to the cortex: an overview

This section should give a rough understanding of the olfactory pathway and is not intended to be exhaustive. The sections of more importance for this thesis will be subsequently described in more detail.

Odorants get inhaled into the nasal cavity and dissolved in the olfactory mucosa of the main olfactory epithelium (OE). In mammals, inhaling or sniffing, is an active sensing mechanism that profoundly shapes nearly all aspects of the olfactory system (Wachowiak, 2011). Olfactory sensory neurons (OSNs, also olfactory receptor neuron), whose somata are located in the OE, extend a single dendrite into the nasal cavity. This dendrite carries 20-30 cilia that contain odorant receptors (ORs) (Imai and Sakano, 2008). ORs were first discovered in rodents in 1991 (Buck and Axel, 1991). Since then, ~ 400 different ORs have been identified in the human genome (Malnic *et al.*, 2004). The olfactory receptor repertoire of rats is estimated to contain 1700 to 2000 genes (Gibbs *et al.*, 2004; Quignon *et al.*, 2005). The mammalian ORs are seven-transmembrane G protein-coupled receptors. (Imai and Sakano, 2008). They are tuned to molecules or more common to specific submolecular features, odotopes, on the surface of odorants (Wilson and Sullivan, 2011; Araneda *et al.*, 2000; Galizia and Lledo, 2013). Each OSN expresses only a single OR but odorants can bind to and activate different subsets of receptors (one neuron-one receptor rule, Serizawa *et al.*, 2004). Each OR sends a single axon out of the OE through the cribriform plate into the forebrain, namely the main olfactory bulb (OB, see *1.1.2*). The entirety of OR axons form the olfactory nerve (cranial nerve one, ON). In the OB, OSNs expressing the same OR converge their axons into the same few (in rodents 1-2) glomeruli in each hemisphere of the OB (one glomerulus-one receptor rule, Imai and Sakano, 2007). Hence, an odorant activates a specific subset of ORs that in turn activate a specific subset of glomeruli with varying magnitudes. In consequence, odorant identity is represented by a unique pattern of activated glomeruli in the OB (Mori *et al.*, 2006). Glomeruli are structures of neuropil where the axons of ORs synapse onto the apical dendrites of the main projection neurons of the OB: mitral

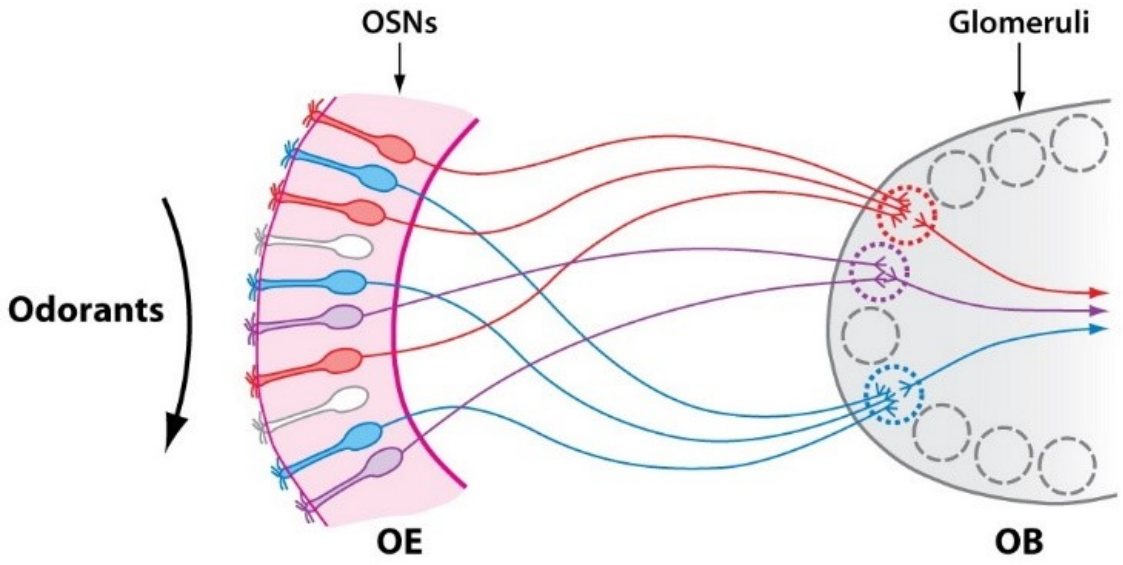

Fig 1. ***One glomerulus-one receptor rule.*** *Olfactory sensory neurons (OSNs) are located in the olfactory epithelium (OE) and express a single olfactory receptor. OSNs expressing the same olfactory receptor converge their axons into the same few glomeruli in the olfactory bulb (OB), and therefore each glomerulus represents a single odorant receptor (represented as red, blue or violet). Modified from Mori and Sakano (2011).*

and tufted cells (MCs and TCs, see *1.1.2.1*). The odor signal is shaped and processed by numerous excitatory and inhibitory interneurons located in different layers of the OB (see *1.1.2.2*) before it is transmitted to the olfactory cortex (OC) by the axons of MCs and TCs, forming the lateral olfactory tract (LOT). The OC is a three-layered paleocortical structure defined by input of OB projection neurons. It includes the anterior olfactory nucleus (AON), tenia tecta, olfactory tubercle, cortical nuclei of the amygdala, anterior and posterior piriform cortex (APC, PPC) and the lateral entorhinal cortex. Each region is differently involved in recognition, separation, and completion of odor-evoked patterns sent from the OB, enabling odor perception. A key feature of the OC is the sparse and distributed encoding of odor quality, standing in contrast to the spatial pattern of OB glomeruli described above (reviewed in Wilson and Sullivan, 2011). The cells of the OC also project axons back to the OB. These cortical feedback projections excite diverse populations of OB interneurons including GCs and are thought to contribute to oscillatory dynamics and olfactory learning in the OB and cortex (Boyd *et al.*, 2012). The main OE and the

main OB are not the only chemosensory and olfactory processing systems. In addition, most mammals have multiple chemosensory systems mediating pheromonal effects. The vomeronasal organ, located in the nasal septum, consists predominantly of ciliated olfactory sensory neurons that project to the accessory olfactory bulb, located in the dorsal-posterior region of the OB. The vomeronasal organ can detect both volatile and non-volatile pheromones (Brennan and Zufall, 2006). The Grueneberg ganglion is located at the anterior end of the nasal cavity and is specialized in detection of danger signals and alarm pheromones (Moine *et al.*, 2018). Additional distinct receptor organs are the septal organ of Masera and the guanylyl cyclase type-D system. The latter system projects to so-called "necklace" glomeruli encircling the main OB (Cockerham *et al.*, 2009). The trigeminal nerve also innervates the nasal cavity, where it is stimulated by many odorants and triggers protective respiratory, secretory, and cardiovascular reflexes (Doty *et al.*, 1978; Meredith, 1988). Another chemosensory system is obviously the gustatory system to evaluate food quality. Taste buds in the cavity sense taste in direct contact with the source of the stimulus. However, as food always liberates volatile compounds, the sense of smell has a decisive role in our taste experience (Galizia and Lledo, 2013).

The vertebrate mammalian olfactory system shows striking resemblance to the invertebrate insect olfactory system, testifying consistency over million years of evolution. In the periphery, sensory receptors are tuned to specific submolecular features to bind a specific group of odorants. Insect ORs are heteromeric ligand gated ion channels (counterpart to mammalian G protein-coupled ORs, Sato *et al.*, 2008). Sensory neurons expressing the same insect OR converge into glomeruli in the antennal lobe (counterpart to the OB), producing odor-specific signals in second order projection neurons (counterpart to MC/TCs) sending their axons to higher brain areas (mushroom body, counterpart of the OC, Wilson and Sullivan, 2011; Grabe and Sachse, 2018).

1.1.2 The main olfactory bulb

OSNs extend their axons solely to the OB, the first site of odor information processing in mammals (Nagayama *et al.*, 2014). It is part of the forebrain and divided into 6 layers: olfactory nerve layer (ONL), glomerular layer (GL), external plexiform layer (EPL), mitral cell layer (MCL), internal plexiform layer (IPL) and granule cell layer (GCL, Fig 2). The neurons of the OB are

conventionally categorized by the layers their somata are located in: juxtaglomerular cells (periglomerular cells (PGs), external tufted cells (ETs), and superficial short axon cells (sSACs)), MCs, and GCs (Nagayama *et al.*, 2014). While TCs and MCs are projection neurons, meaning they innervate brain regions outside the OB, most other neurons in the OB are interneurons that only have projections inside the bulb. OSNs send their axons from the OE in the nasal cavity into the glomeruli where they synapse on primary dendrites of MCs and TCs. The signal propagates through the primary dendrites to the cell body of MCs (in the MCL) and TCs (in the EPL), where it is not only transmitted to other brain areas via the axon, but also back-propagates through the horizontal secondary dendrites in the EPL. Of note, back-propagating action potentials (bpAPs) are not decremental in the apical, but are decremental in lateral dendrites (Margrie *et al.*, 2001). On the lateral dendrites, reciprocal dendrodendritic synapses with granule cells are formed (see *1.1.3*). As described above, each OSN expresses only a single OR and all OSNs expressing the same type of OR converge their axons into the same few glomeruli. As each MC/ TC just ramifies into one glomerulus, each glomerulus and its associated projection neurons form an OR module (also glomerular column, Mori and Sakano, 2011). The number of MCs and TCs synapsing into a single glomeruli varies greatly between studies but most report a maximum of ∼10 in mice and ∼20 in rats (Panhuber *et al.*, 1985; Liu *et al.*, 2016a). This neuronal arrangement gives rise to a certain topographic representation of odorants on the level of glomeruli in the OB. To what extend the olfactory map is truly topographical like other sensory systems, e.g. the visual system, is highly under debate. Topographic maps were proposed to be formed by OSNs located in distinct parts of the OE projecting to distinct parts of the OB or by clustered projections of different classes of ORs (fish- and terrestrial-type). Furthermore, odorant selectivity (molecular receptive range) of individual glomeruli was proposed for map formation: odorants with common molecular features, e.g. fatty acids or aliphatic alcohols, activate subsets of glomeruli that form clusters in the OB. Another approach is to organize the olfactory map in terms of functions and behavior: clusters responding to innate vs. learned responses, clusters for fear, social behaviors, aggression or aversion against spoiled food (reviewed in Mori and Sakano, 2011).

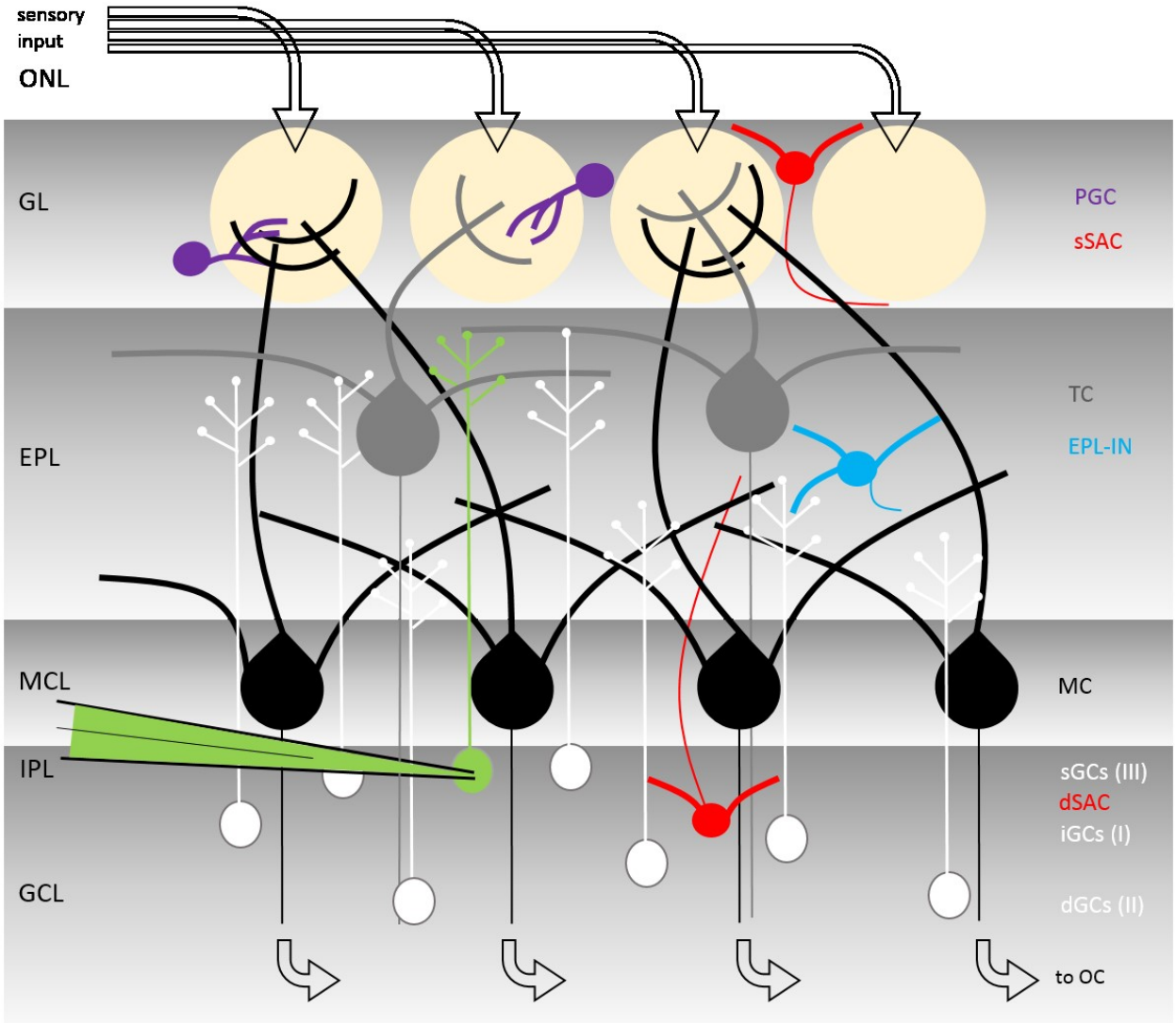

Fig 2. ***Basic model of the olfactory bulb network.***
Sensory input via the axons of olfactory sensory neurons reaches the olfactory bulb in the olfactory nerve layer (ONL) and converges into glomeruli in the glomerular layer (GL). Here, synapses with the apical dendrites of mitral and tufted cells (MC, TC) are built. Juxtaglomerular cells are represented by periglomerular cells (PGC) and superficial short-axon cells (sSAC). PGs make reciprocal synapses with the dendrites of MC/TCs. Somata of TCs are located in the external plexiform layer (EPL), while MC somata are located in the Mitral cell layer (MCL). Both have axonal projections to the olfactory cortex (OC) and elongated secondary dendrites in the EPL, where they form reciprocal dendrodendritic synapses with granule cells (GCs). In the EPL various types of EPL interneurons (EPL-IN) are located. The somata of GCs are located in the granule cell layer (GCL) and subtypes are determined based on the depth of their somata in the GCL and the sublayer to which their dendrites extend: superficial GCs (sGC, type-III), intermediate GCs (iGC, type-I), deep GCs (dGC, type-III). Various types of deep short-axon cells (dSAC) are located in the IPL and GCL and form inhibitory synapses with GCs. One GC is represented as filled with green fluorescent dye OGB-1 via a patch pipette.

Finally, axonal projections of MCs and TCs target several higher brain areas, which compose the OC (see *1.1.1*). However, this extremely simplified OB circuit does not reflect the complexity and number of neuronal cell types present in the OB. There are various other cell types present in the OB, albeit in smaller numbers and the ones described above comprise heterogeneous populations of morphologically, molecularly and functionally distinct subtypes (Nagayama *et al.*, 2014). Due to their vast amount, I will not describe each subtype's function in its entirety but only the neurons, which were of special interest for this thesis, in more detail below.

1.1.2.1 Mitral and tufted cells

The names MC and TC are often used interchangeably, but there are morphological, projection and functional differences. Both have a single apical and multiple lateral dendrites, but TC's lateral dendrites ramify preferentially in the superficial half of the EPL, while those of MCs are primarily located in the deeper half of the EPL. The total dendritic length of TCs is also significantly shorter (Igarashi *et al.*, 2012). The dendrites are smooth, meaning that they do not bear spines. The axons of MCs and TCs fasciculate and form the LOT together, but while TCs project mainly to the anterior areas of the OC and individual TCs densely target specific regions, MCs show dispersed projections to all OC areas (Takahashi *et al.*, 2018). In detail, MCs project to the piriform cortex, lateral entorhinal cortex, cortical amygdala, AON, tenia tecta and the cortical region of the olfactory tubercle. TCs project to the AON pars externa, posteroventral part of the AON, ventrorostral part of the APC and the cap region of the olfactory tubercle (Imai, 2014). Another unique feature of TCs are axon collaterals to the other hemisphere that connect glomeruli with the same identity (Mori and Sakano, 2011). TCs are classified into three subtypes: internal tufted cells (somata deep in the EPL), middle tufted cells (somata in superficial EPL), and the interneuronal external tufted cells (somata at border of EPL and GL or in GL) (Macrides and Schneider, 1982). TCs show short-latency firing (∼110 ms) in response to a wide range of odor concentrations, whereas MCs only respond to strong finer tuned signals with a latency of above 200 ms (Igarashi *et al.*, 2012). This phase shift between MCs and TCs is most likely mediated by ON-driven feedforward inhibition by periglomerular cells (see *1.1.2.2*). Rodents reportedly discriminate simple odors with high accuracy in 150 -250 ms but require ∼100 ms more to discriminate difficult and highly similar odors (Abraham *et al.*, 2010; Abraham *et al.*, 2004;

Rinberg *et al.*, 2006). This indicates a critical role of TCs in fast responses in olfactory behavior, whereas MCs are recruited for more difficult odor discrimination (Igarashi *et al.*, 2012). MCs and TCs are laterally inhibited by GCs at different firing rates and MCs receive stronger inhibition from juxtaglomerular cells (Geramita and Urban, 2017; Geramita *et al.*, 2016).

To conclude, like in other sensory systems, e.g. the visual system where motion and color are segregated (Callaway, 2005), MCs and TCs might give rise to segregated parallel processing of different odor features.

1.1.2.2 Excitation, inhibition and modulation in the OB

The sensory input to the OB is processed by a wide range of intra-bulbar connections and input from other brain regions. Synaptic inhibition critically influences sensory processing throughout the mammalian and insect brain (Burton, 2017; Ai *et al.*, 2018) and in the OB the vast amount of interneurons is of inhibitory nature, as well. Here, I describe a selection of cell types, which shows the complexity of intra-bulbar signaling, necessary for the functional context of GCs.

In the GL, juxtaglomerular cells include glutamatergic ETCs, GABAergic PGCs, and combined GABAergic and dopaminergic sSACs, that directly modulate the input from the OSN to the MCs and TCs (Burton, 2017). ETCs excite the principal neurons via robust feedforward excitation. Gire *et al.* (2012) even show that MCs are typically not activated by direct OSN input but require a multistep mechanism via ETCs. sSACs receive excitatory input directly via OSNs or secondarily via ETCs. Their name is misleading, as these cells can extend multiple axonal branches up to ~1 mm into tens of glomeruli. This predestines them for lateral inhibition (see *1.1.3.2*) and indeed, several studies found them to be involved in interglomerular lateral inhibition independent from GCs (Liu *et al.*, 2016b; Banerjee *et al.*, 2015; Whitesell *et al.*, 2013). sSACs have been shown to provide excitatory dopaminergic and gap junctional output to various cell types *in vitro* but optogenetic activation *in vivo* drove pure suppression of principal neuron activity (Burton, 2017; Liu *et al.*, 2016b; Banerjee *et al.*, 2015). A subtype of sSACs, dopaminergic clasping SACs, have been shown to densely innervate the somata of other, putatively glutamatergic juxtaglomerular cells (Bywalez *et al.*, 2016). In contrast to most sSACs, PGCs innervate just a single glomerulus. They receive, depending on the subtype, excitatory input from ETCs or directly from OSNs. PGCs' GABAergic release drives self-signaling or mixed excitation/ inhibition of other PGCs and ETCs

(Burton, 2017). Najac *et al.* (2015) identified an interesting axonless subtype that is both excited by and inhibits MC/TCs. It participates in intraglomerular lateral inhibition, a mechanism to reduce similarity of principal cells activated by the same glomerular input. Furthermore, ON-driven PGs have been shown to provide sniff-coupled feedforward inhibition onto MCs, setting the phase shift between MCs and TCs (see 1.1.4, Fukunaga *et al.*, 2014).

In the EPL, besides GCs, principal neurons synapse onto a morphologically diverse array of axonless and axonbearing EPL interneurons (EPL-IN) like so-called Van Gehuchten, multipolar, satellite, horizontal, and short-axon cells. They form both reciprocal and nonreciprocal synapses exclusively with MCs and TCs. EPL-IN get similar input like GCs but, in contrast to GCs (see *1.1.3*) this excitatory input evokes short-latency, rapid firing (Burton, 2017). One class of EPL-INs is characterized by their expression of the calcium (Ca^{2+}) binding protein parvalbumin (PV-cells). These cells are densely connected to neighboring MCs and have been proposed to mediate classical center-surround lateral inhibition (Kato *et al.*, 2013).

Deep short-axon cells (dSACs) are located in the IPL and GCL and can be divided into subtypes based on their axonal projections: GCL-, EPL-, and GL-projecting dSACs (Eyre *et al.*, 2008). One single dSAC forms hundreds of inhibitory synapses with GCs regulating their activity by rapid feedforward inhibition (Burton and Urban, 2015; Eyre *et al.*, 2009). Together with sensory input from ETCs, dSACs are heavily innervated by centrifugal piriform projections and could therefore act as hubs for centrifugal modulation of OB activity (Burton, 2017; Burton *et al.*, 2017; Boyd *et al.*, 2012). Burton *et al.* (2017) showed that dSACs also innervate the apical dendrites of TCs, mediating widespread inhibition. This makes dSACs a candidate for TC specific lateral inhibition.

Additionally, classical neuromodulatory inputs including noradrenergic inputs from locus coeruleus, serotonergic inputs from raphe nuclei and cholinergic inputs from the basal forebrain modulate sensory processing in the OB dependent on the organism's behavioral state and experience (Rothermel and Wachowiak, 2014). At the medial border of the GL, somata of glutamatergic vasopressin cells, an example for intrabulbar neuromodulation, are located. Vasopressin in the OB is associated with social discrimination via individual odor signatures (Lukas *et al.*, 2019).

1.1.3 Olfactory bulb granule cells

GCs are the most common cell type in the OB and play a central role in odor information processing. They are axonless GABAergic inhibitory interneurons with a small cell body of 6-8 µm in diameter, localized in the GCL, IPL and MCL (Price and Powell, 1970b). They usually have a single apical dendrite that extends towards the surface of the OB and branches in the EPL where they form reciprocal dendrodendritic synapses with MCs and TCs via 200-300 large spines (Fig 3). Spines are cell membrane protrusions of varying, activity-dependent morphology. They increase the cell membrane, electrically and biochemically compartmentalize synapses and reportedly influence learning and plasticity (Scheuss and Bonhoeffer, 2014; Harvey and Svoboda, 2007; Matsuzaki *et al.*, 2004; Bywalez *et al.*, 2015). Of note, a single MC/TC-GC pair forms only one or a few synaptic contacts, which conversely means that each GC reciprocally connects with hundreds of MCs or TCs (Woolf *et al.*, 1991b; Burton, 2017). The spines function as both post- and presynapse. Glutamatergic MC/TCs excite the electrically compartmentalized dendritic GC spine, locally activating voltage-gated Na^+ channels (Na_vs, see *1.2.3*) that activate classic presynaptic N/P/Q voltage-gated Ca^{2+} channels (Ca_vs, see *1.2.3*), which in turn release GABA back onto the MC/TC dendrites (Bywalez *et al.*, 2015). Recent results of our working group also demonstrate high NMDAR-dependence of fast reciprocal GABA release. Pharmacology and ultrastructural analysis using electron microscopy, proving proximity of NMDARs to the SNARE release machinery, provide evidence that GABA release from GCs is mediated by classical axonal release mechanisms with an additional NMDAR-dependence (Lage-Rupprecht *et al.*, 2019). These studies reinforce the notion of the reciprocal spine as a mini-neuron. However, whether pure local activation can indeed trigger release of GABA back onto the exciting MC/TC remains to be elucidated.

A peculiarity of GCs is that they are generated and replaced permanently throughout life. The only other brain region where new cells are integrated into the neuronal circuit throughout life is the hippocampus that is strongly associated with learning and memory. In fact, new-born neurons in the hippocampus are, like GCs, associated with pattern separation and the generation of gamma oscillations (Sahay *et al.*, 2011). The neural progenitor cells are generated in the ventricular-subventricular zone of the lateral ventricle (V-SVZ) and moved to the OB through the

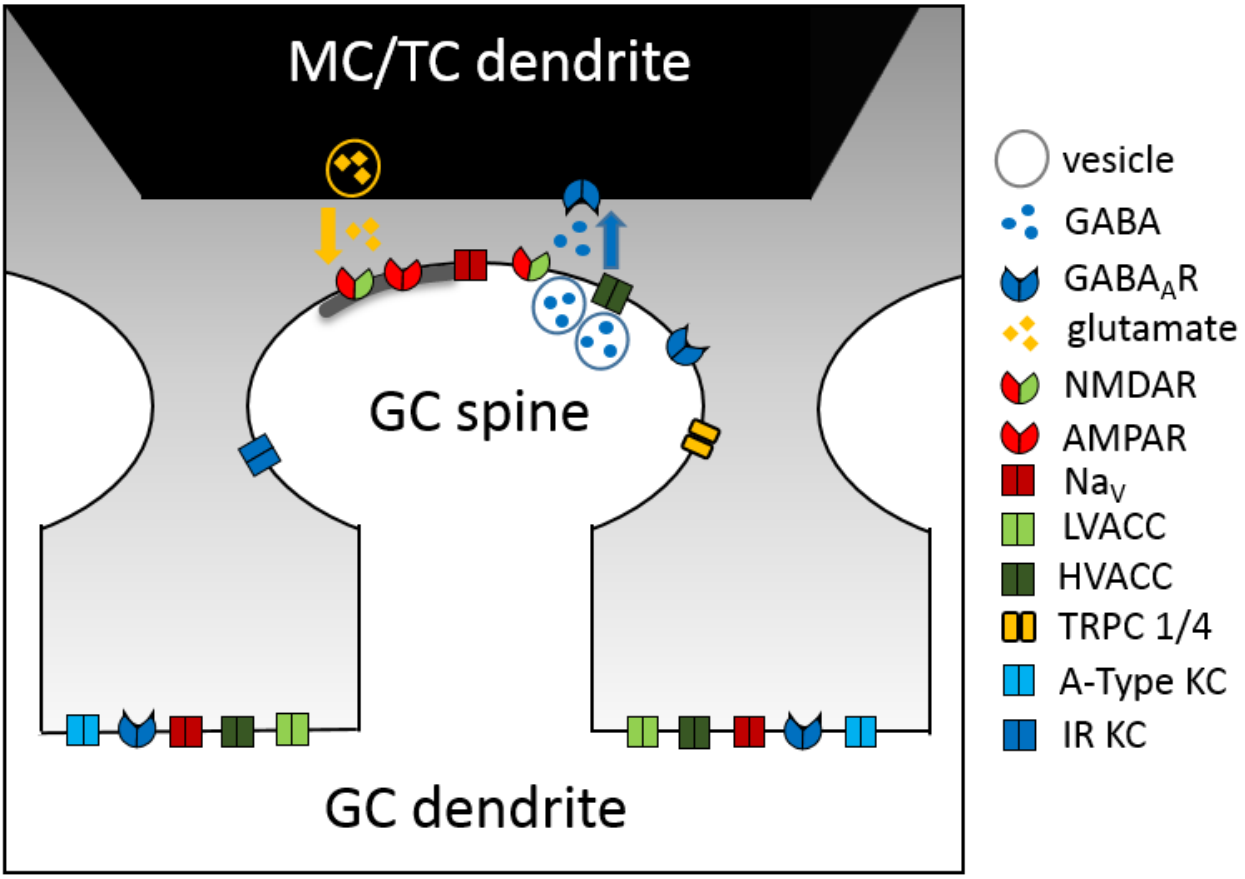

Fig 3. ***Basic model and ion channel localization of the reciprocal dendrodendritic MC/TC – GC synapse and GC dendrite.*** *This model is not intended to be exhaustive and only channels of interest for this thesis are displayed. Subcellular localization of the channels is based on the literature referred to in 1.1.3, 1.2.2 and 1.2.3, but exact localization has not been demonstrated for all channels. Excitatory glutamatergic input from the MC dendrite binds to NMDAR and AMPAR on the GC spine. Locally activated Na_vs activate classic presynaptic HVACC channels. Ca^{2+} influx via HVACC and NMDAR triggers GABA release back onto MC/TC dendrites. Coactivation of several spines can lead to dendritic spikes mediated by opening of NA_vs, HVACC, LVACC and NMDA-R. GC: granule cell, MC: mitral cell, $GABA_A$-R: ionotropic gamma-aminobutyric acid receptor, NMDAR: n-methyl-$_D$-aspartate receptor, AMPAR: alpha-amino-3-hydroxy-5-methyl-4-isoazole propionic acid receptor, Na_v: voltage-gated sodium channel, LVACC: low-voltage-activated calcium channel, HVACC: hight-voltage-activated calcium channel, TRPC 1/4: canonical transient receptor potential channel 1/4, a-type KC: a-type potassium channel, IR KC: inward rectifier potassium channel.*

rostral migratory stream (RMS), where they differentiate into GCs or PGs (Takahashi *et al.*, 2018). The V-SVZ is divided into finely patterned microdomains producing the numerous subtypes of GCs (see below, Merkle *et al.*, 2014). In this way, ~10.000 new neurons enter the OB every day of which half are integrated into the existing neuronal circuit (Yamaguchi and Mori, 2005). Interestingly, several studies showed that adult-born GCs are preferentially integrated into the

deep GCL, while most prenatally-born GCs are located in the superficial GCL (Nagayama *et al.*, 2014).

1.1.3.1 Granule cell- types

Morphologically, GCs can be divided into 3 groups based on their ramification in the whole EPL (Type-I), only the deep (Type-II), or only the superficial EPL (Type-III). Together with the location of the lateral dendrites of MCs and TCs (see *1.1.2.1*), this indicates Type-II and Type-III GCs to preferentially innervate MCs and TCs, respectively. Interestingly, their ramification pattern relative to the surface of the OB seems to be reflected, at least to some extent, in the position of their somata. Meaning that superficial GC (sGC) somata located in the IPL or MCL will mainly ramify in the superficial EPL (Geramita *et al.*, 2016; Burton and Urban, 2015). Interestingly, sGCs are reportedly more excitable than deep GCs (dGCs, Geramita *et al.*, 2016; Wellis and Scott, 1990)). Additionally, Merkle *et al.* (2014) reported four more GC types of which two (Type-IV and –V) only branch in GCL and MCL. While some molecular markers confirm the classical subtypes (e.g. calretinin is only expressed in superficial GCs), others are specifically expressed in subgroups of GCs that could not be described solely by their morphology. Ca^{2+}/calmodulin-dependent protein kinase $IIα^{+}$ is expressed in only half of GCs in the mouse OB and these GCs are preferentially activated by olfactory stimulation due to weaker inhibitory inputs. *cFOS* expression showed that both populations were also functionally distinct and activated during different behavioral tasks (Malvaut *et al.*, 2017). Type-S GCs express nestin, usually expressed during development, in the adult state and synapse on the perisomatic region of MCs, putatively regulating the generation of action potentials (APs, Naritsuka *et al.*, 2009). Another obvious feature to divide GCs into groups is to distinguish between prenatally-born, postnatally-born and adult-born neurons. Despite, both morphologically and molecularly, almost all types of GCs have been shown to be generated in the adult OB (Nagayama *et al.*, 2014), various studies show differing roles in olfactory processing and behavior (reviewed inTakahashi *et al.*, 2018).

To cover all subtypes described in the literature would go beyond the scope of this work. Nonetheless, the common features of all GCs, being GABAergic, axonless, located in GCL/MCL and spine bearing, defines them as a very distinct group and makes intrinsic functional findings translatable to other subtypes in most cases.

1.1.3.2 Functions of granule cells: recurrent and lateral inhibition

MC/TC – GC synapses are the most numerous in the OB and together with their different excitation modes (see *1.2.5*), this enables both recurrent and lateral inhibition of/between MCs and TCs. As described above, different populations of GCs preferentially synapse onto MCs or TCs or they ramify throughout the EPL (see *1.1.3.1*). Thus, GCs form both segregated and overlapping microcircuits of MCs and TCs (Takahashi *et al.*, 2018). Together with the functional differences of the two main projection neurons (see *1.1.2.1*) this gives rise to different functions of GC subpopulations. However, for simplification I will not consequently differentiate between functions of subtypes in the following.

Recurrent inhibition and thus indirect self-inhibition of MC/TCs via GCs, has been shown to mediate a shunting effect, thereby regulating AP propagation within MC/TC lateral dendrites, and short-term depression (Halabisky and Strowbridge, 2003; Dietz and Murthy, 2005; Burton, 2017). Abraham *et al.* (2010) demonstrate increased recurrent inhibition *in vitro* and *in vivo* by enhancing synaptic Ca^{2+} influx in GCs using a viral strategy in mice and Nunes and Kuner (2015) showed a similar effect by genetic disinhibition of GCs. Both studies demonstrate that this accelerates odor discrimination (see *1.1.3.3*).

Lateral inhibition is a circuit motif found throughout the whole nervous system. By decorrelation of the degree to which neurons respond to the same or overlapping stimuli, it can generate contrast enhancement or center-surround receptive fields to facilitate discrimination (Arevian *et al.*, 2008; Geramita *et al.*, 2016). In the rodent OB, a single MC's dendritic tree is connecting, indirectly via GCs, with hundreds of other mitral cells in the bulb (Arevian *et al.*, 2008; Orona *et al.*, 1984). Together with the discontinuous topography of the OB (see *1.1.2*) and the input of several other surrounding interneurons in all layers (see 1.1.2.2), this makes the principle of recurrent and lateral inhibition in the OB highly complex.

In *in vitro* paired recordings, lateral inhibitory currents have been observed between 10 - 20% of MC pairs (Isaacson and Strowbridge, 1998; Urban and Sakmann, 2002), while, when MCs were additionally activated, decreases in firing rate could be observed in ∼50% of pairs (Arevian *et al.*, 2008). Arevian *et al.* (2008) proposes activity-dependent (in contrast to subtractive or divisive) lateral inhibition independent from the spatial structure of conventional center-surround

mechanisms. They showed that “postsynaptic MCs” are mainly inhibited by strongly firing “presynaptic MCs” via overlapping populations of GCs if they are firing at intermediate rates themselves. Thus, the “postsynaptic” MC influences the effectiveness of the lateral inhibition that it receives via the recurrent dendrodendritic synapse with shared GCs. This fits to the recent findings of our working group, that GC GABA release is highly NMDAR dependent, i.e. dependent on presynaptic activity. This would achieve useful competitive interaction between only active MCs and increase contrast. Cells firing above an upper bound would be “immune” to lateral inhibition as they recruit the maximum amount of recurrent inhibition, such that additional inputs to GCs cannot trigger additional GABA release (Urban and Arevian, 2009; Arevian *et al.*, 2008). A very similar model of net inhibition of low-responding MCs but not highly excited MCs is also proposed by Alonso *et al.* (2012) and Geramita *et al.* (2016) expand this model by demonstrating different lower and upper bounds for the effective activity range for lateral inhibition in MCs and TCs. Notably, both the lower and upper bound are significantly lower in TCs. This is, at least to some extent, mediated by different excitability of the GC subtypes they are synapsing on (see *1.1.3.1*). Other recent studies support this model of randomly scattered lateral inhibition over the OB surface (Kim *et al.*, 2012a; Economo *et al.*, 2016). As sensory stimuli are encoded by altering rates and temporal patterns of spiking in projection neurons, decorrelation of spike trains of different MC/TCs via lateral inhibition causes contrast enhancement (Arevian *et al.*, 2008; Giridhar *et al.*, 2011). Tan *et al.* (2010) elegantly demonstrate odor-evoked GABA-mediated contrast enhancement in the OB *in vivo*: Recordings from OSNs, MC/TCs, PGs and GCs show that interneurons are more broadly tuned to odors than projection neurons. Upon suppressing of odor-evoked MC/TC inhibition by application of a $GABA_AR$ antagonist, the projection neurons’ odor tuning became equally broadened.

Lateral inhibition between MC/TCs has been shown to be strongly NMDAR-dependent, independent of APs fired by GCs and still persistent if the apical dendrite was truncated (Isaacson and Strowbridge, 1998; Arevian *et al.*, 2008). Nevertheless, as described above, GCs are not the only OB interneurons mediating inhibition in the OB. Classical center-surround lateral inhibition has been shown in Parvalbumin-cells (see 1.1.2.2, Kato *et al.*, 2013) and EPL-IN and PGCs have been shown to mediate recurrent inhibition of MC/TCs (Burton, 2017).

1.1.3.3 Behavioral functions of granule cells

How recurrent and lateral inhibition translate into behavior output is highly under debate. Nevertheless, numerous studies associated GCs with a wide range of functions. Sakamoto *et al.* (2014) showed that inhibition of postnatal-born OB interneurons in mice did not affect simple discrimination of a rewarded from a non-rewarded odor. Whereas, following the reward-reversal paradigm, where the previously non-rewarded odor becomes the rewarded odor, the mice showed defects, demonstrating that postnatal-born GCs are important for flexible olfactory associative learning and memory. Selective activation of adult-born GCs using optogenetics accelerated learning to discriminate difficult odor pairs while it did not affect discrimination of easy odor pairs (Alonso *et al.*, 2012). Similarly, Gschwend *et al.* (2015) showed that enhanced inhibition of MCs and TCs by optogenetic activation of GCs improved discrimination of similar odors while pharmacogenetic silencing of GCs resulted in a deterioration of odor discrimination learning. On the other hand, disinhibition of both pre- and postnatally-born GCs in mice did shorten the time required to discriminate dissimilar and highly similar odors, while discrimination learning remained unaffected (Nunes and Kuner, 2015). Fittingly, inhibition of GABA release by GCs after deletion of $Na_v1.2$ did increase the discrimination time of highly similar odorant mixtures and, again, discrimination learning remained unaffected (Nunes and Kuner, 2018). This confirmed the results of Abraham *et al.* (2010) that increased inhibition mediated by GCs accelerated discrimination and weaker inhibition decelerated discrimination of similar odor mixtures, while leaving learning and memory unaffected. Taken together, the role of GCs in rapid differentiation of highly similar odors and odor mixtures seems to be rather clear. Despite continuous progress, the role of GCs in discrimination learning and memory remains to be elucidated.

GC-mediated recurrent and lateral inhibition of/between MC/TCs is also involved in the generation of gamma oscillations that synchronize the firing of the projection neurons, which is necessary for effective transmission of odor information from the OB to higher brain areas (Mori *et al.*, 2013).

1.1.4 Oscillations in the olfactory bulb

Oscillations and temporal structure of activity is an essential aspect of communication in the brain. Already in the 1950s, OB interactions between inhibitory and excitatory neurons have been shown to underlie synchronous activities at slow, sniff cycle-coupled theta frequencies (1 – 12 Hz) as well as faster beta (15 – 30 Hz) and gamma frequencies (40 – 100 Hz) (Wachowiak, 2011; Fukunaga *et al.*, 2014; Adrian, 1950). Theta oscillation coupled spike latencies, sharpened by lateral inhibition, have been proposed to code for odor information faster and with more resolution than actual firing rates (Margrie and Schaefer, 2003). Odor-evoked gamma oscillations have been associated with successful discrimination of closely related odorants and both beta and gamma frequencies with odor learning. Theta and gamma oscillations are also present in the OC (Kay *et al.*, 2009). Both MCs and TCs are locked to different respiration phases, whereby MCs are delayed relative to TCs (Fukunaga *et al.*, 2012). Until recently, GCs were suggested to be mainly involved in shaping this respiration coupling of projection neurons, but Fukunaga *et al.* (2014) provide evidence that it is driven by feedforward inhibition from glomerular interneurons. By specific activation and silencing of GL and GCL interneurons using optogenetics and pharmacology, they show that GL interneurons drive sniff coupled theta oscillations whereas GCs drive fast gamma oscillations, nested in the sniff rhythm. Fast gamma oscillations are associated with higher task demands (Kay *et al.*, 2009). The gamma oscillation band in the OB can be further divided into two types. Fast gamma oscillations carried by TCs and slow gamma oscillations carried by MCs (Manabe and Mori, 2013). Thus, MC/TC output is highly temporally regulated on two levels mediated by two distinct inhibitory circuits: theta, sniff coupled frequencies governed by PGCs and embedded two-type gamma frequencies governed by GCs (Fukunaga *et al.*, 2014).
These results, together with doubts about specificity in activating /inhibiting GCs in many studies described above (reviewed in Burton, 2017), give rise to a change in the common belief about GCs being responsible for sniff coupled and odor evoked slow lateral inhibition. Evidence suggests that GCs are more involved at the second level generation and synchronization of gamma oscillations. Whether these recent hypotheses, the classical role of GCs or a combination is more plausible remains to be elucidated.

1.2 Excitability of dendrites

Dendrites have long been seen as simple antennas, conducting input signals to the soma, where the inputs are integrated and can trigger AP generation at the axon hillock. However, research in the past decades revealed manifold dendritic nonlinear biophysical phenomena actively participating in sophisticated computations (Payeur *et al.*, 2019). Furthermore, circuits like the OB where most synapses are dendrodendritic (Crespo *et al.*, 2013) and in particular axonless neurons like GCs demonstrate that dendrites can perform all basic tasks of a neuron: input reception, input integration and output generation.

1.2.1 Passive electrical properties of dendrites

The basis of the excitability of dendrites is the lipid bilayer forming the cell membrane. It insulates the inside from the outside of the cell and, together with the embedded ion channels and transporter proteins, enables the generation of potentials. Excitatory synaptic input leads to the depolarization of the postsynaptic membrane potential (V_m) from the resting membrane potential (V_{rest}), a so-called excitatory postsynaptic potential (EPSP). Synaptic input integration is affected by the morphology of the cell, location of the synapse and the time course of the synaptic current. The passive, or electrotonic, properties of the dendritic tree depend on the specific membrane resistance (R_m), the specific membrane capacitance (C_m), and the intracellular resistance (R_i). These three passive membrane properties, together with the neurite diameter (d), form the constants describing a dendrite's passive cable properties:

time constant: $\tau = C_m * R_m$

τ is the time for the potential to reach 1- $\frac{1}{e}$ or 63 % of its final maximum or to decrease to 37 % from its maximum. Therefore τ defines the time window over which multiple synaptic potentials can sum. τ ranges from below 1 ms in octopus cells to 50-70 ms in hippocampal CA3 pyramidal cells (PCs, Stuart *et al.*, 2016; Rall, 1969).

length constant: $\lambda = \sqrt{\frac{dR_m}{R_i}}$

λ is the distance a potential will travel along the dendrite before it decays to 37 % of its maximum. Therefore λ defines the distance along the dendrite over which multiple synaptic potentials can sum (Rall, 1969; Stuart *et al.*, 2016).

High values of R_i and low values of R_m increase the attenuation of an EPSP as it propagates along the dendrite. C_m attenuates especially short potentials as the charging of the membrane capacitance uses up most of the initial charge of potentials. The further a potential travels along the dendrite, the more charge deposited onto the dendrite capacitance is lost through the membrane resistance resulting in a smaller, slower EPSP. This **spatiotemporal filtering** enables e.g. low-pass filtering or, in combination with high-pass filtering of an active current (see below), membrane resonance crucial for network oscillations (Payeur *et al.*, 2019; Fox *et al.*, 2017). Additional attenuation is mediated by channels open at the resting membrane potential causing the membrane to be "leaky". Electrotonic attenuation can be curbed by dendritic morphology alone. Otopalik *et al.* (2019) show that strong tapering of dendrites leads to electrotonic compactness and almost linear voltage integration. Notably, the term "passive properties" is misleading as the generation and propagation of EPSPs is dependent on voltage-dependent channels open at V_{rest} that are involved in maintenance of the membrane potential, e.g. inward-rectifier potassium (K^+) channels (Stuart *et al.*, 2016; Spruston and Johnston, 1992).

EPSPs are generated by the opening of ion channels. The ion channel composition of not only different neuronal types but of each subcellular compartment such as the soma, proximal, distal dendrites, and dendritic spines, is unique and is a key determinant of their individual input-output transformation. Ion channels can be ionotropic or metabotropic (second messenger e.g. G-protein coupled, Stuart *et al.*, 2016). Here, I focus on ionotropic ion channels.

1.2.2 Neurotransmitter-gated ion channels

Chemical synapses are the most common connections between neurons. Upon AP arrival, the presynapse releases neurotransmitters into the synaptic cleft where they bind to the receiving elements of the postsynapse: neurotransmitter-gated ion channels. Upon binding of several molecules of their agonist they rapidly open their ion permeable pore leading to, depending on

charge and direction of ion flow, membrane depolarization or hyperpolarization (Hille, 2001). The numbers of channels and receptors, the maximum number of open channels, their kinetics, ion permeability, and conductance varies from synapse to synapse and determine the effectiveness of the excitatory or inhibitory signal (Stuart *et al.*, 2016). The selection of channels described here, have the common feature that they can be assembled from a variety of subunits greatly influencing these properties.

Alpha-amino-3-hydroxy-5-methyl-4-isoazole propionic acid receptors (AMPARs) form as homo- or heterotetramers from either GluA1-GluA4 subunits or GluK1-GluK5 subunits (kainate-type glutamate receptors) (Stuart *et al.*, 2016). They are excitatory ionotropic cation-selective glutamate receptors and are permeable for Na^+, Ca^{2+}, K^+, and zinc ions (Jonas *et al.*, 1994; Stuart *et al.*, 2016). AMPARs expressing specific edited forms of the GluA2, K1, or K2 subunit are impermeable to Ca^{2+} (Burnashev *et al.*, 1992; Stuart *et al.*, 2016). AMPARs are concentrated in the PSD (postsynaptic density) of glutamatergic synapses, have a fast onset and rise time and a fast deactivation within 0.5 – 1 ms (Traynelis *et al.*, 2010; Stuart *et al.*, 2016). As OB GCs express the specific edited form GluA2 subunit, they are impermeable to Ca^{2+} (Abraham *et al.*, 2010). Schoppa (2006a) show that distal input to GCs is mediated by the kainate-type while proximal input is mediated by AMPARs.

N-methyl-$_D$-aspartate receptors (NMDARs) are ionotropic glutamate receptors and nonspecific cation channels that are permeable for Na^+, K^+, and Ca^{2+}. 6-12% of total cation current are Ca^{2+} ions (Grienberger and Konnerth, 2012). They assemble as di- or triheterometric receptors from GluN1-3 subunits. NMDARs have key roles in neuronal development, sensory perception, learning and memory formation (Stuart *et al.*, 2016). Besides their slower activation time and a deactivation time from 40 ms – 2 s (Vicini *et al.*, 1998), the biggest difference to AMPARs is the voltage-dependent block of NMDARs by extracellular magnesium (Mayer *et al.*, 1984; Nowak *et al.*, 1984). Substantial current flow through NMDARs requires coincident pre- and postsynaptic activity or, in other words, simultaneous presynaptic glutamate release and postsynaptic membrane depolarization (Stuart *et al.*, 2016). The release of the magnesium block by membrane depolarization can counteract the reduction of driving force due to large depolarizations (Cash

and Yuste, 1999). With enough glutamate release, NMDARs can even generate a regenerative "NMDA spike" (Schiller *et al.*, 2000; Antic *et al.*, 2010) but, unlike a Na^+-spike, they are restricted to those sections of the dendrite that receive synaptic input (see 1.2.4, Larkum *et al.*, 2009).
Of note, metabotropic glutamate receptors are also present in the GC spine and have been shown to play powerful neuromodulatory roles (Dong *et al.*, 2009).

Gamma-aminobutyric acid receptors ($GABA_A$Rs) are the most common ionotropic inhibitory ion channel and are permeable to small anions like SCN^-, I^-, Br^- and NO_3^- and most prominently Cl^-. Binding of their agonist GABA leads to an influx of Cl^- and thus to membrane hyperpolarization from V_{rest} (Hille, 2001). In mammals they are formed from pentameric assemblies of 19 different subunit genes, allowing thousands of possible combinations in different brain regions and neuronal populations (Stuart *et al.*, 2016).

1.2.3 Voltage-gated ion channels

Na_vs and Ca_vs possess four similar subunits with an ion conducting pore. Each subunit consists of a lipophilic part (s1-4) and an aqueous part (s5-6), wherein s4 is the voltage-sensing region. This region is positively charged and mobile, therefore it can be pushed by the electric field. Thus, hyper- or depolarization leads to a conformation change and thereby closing or opening of the ion channel (Ahern *et al.*, 2016). Besides the opened and closed state, Na^+ and Ca^{2+} channels are in an inactive state for a defined time after activation. Hyperpolarization of the cell leads to reactivation of the ion channel.

Voltage-gated Na^+ channels (Na_vs), opened by a depolarization from V_{rest}, mediate an inward current of positively charged Na^+ ions and thereby further depolarize the cell. They express five different subunits in the central nervous system (Na_v1.1, 1.2, 1.3, .1.5 and 1.6) (Trimmer and Rhodes, 2004). All different Na^+ channels are activated in <1 ms, above > -45 mV, deactivated in <1ms and are inactive for ~1 ms (Stuart *et al.*, 2016). The highest concentration of Na_vs is found in the nodes of Ranvier of myelinated axons and in the axonal initial segment (Stuart *et al.*, 2016) but they are also strongly expressed in dendrites (Lorincz and Nusser, 2010). In mice, the axonal Na_v1.2 is reportedly expressed in clusters distributed throughout the cell surface including dendritic spines(Nunes and Kuner, 2018). My preliminary data, however, using the same Na_v1.2 specific inhibitor phrixotoxin-3 (Tocris), could not confirm this result in rats.

Voltage-gated Ca^{2+} channels (Ca_vs) are categorized into high- and low-voltage-activated channels (HVACCs, LVACCs). Their slower, more prolonged inward current allows prolonged single APs and bursts of multiple APs, when they are activated together with Na_vs. They also provide a pathway for Ca^{2+} influx in addition to agonist-gated ion channels (Stuart *et al.*, 2016). High-voltage-activated L-, P/Q-, N-, and R-type Ca^{2+} channels are all present in different cell types and cell compartments. N, P/Q and R-type Ca^{2+} channels mediate release from axon terminals while L- and T-type Ca_vs are mainly responsible for dendritic influx of Ca^{2+} in most neurons (Stuart *et al.*, 2016; Catterall, 2000). L-type, together with R-type Ca_vs, are predominantly present in spines of pyramidal neurons. They are effectively activated by bpAPs and synaptically mediated depolarization of dendritic spines (Grienberger and Konnerth, 2012). In GCs, despite being located on the dendrite, N/P/Q-type and T-type Ca_vs have been shown to mediate Ca^{2+} influx during different modes of activation (Bywalez *et al.*, 2015; Egger *et al.*, 2005; Egger *et al.*, 2003). Like in axonal synapses, the dendritic release of neurotransmitters at the MC/TC GC synapse relies on N- and P/Q-type Ca_vs (Isaacson and Strowbridge, 1998). N-type and P-type Ca_vs are activated fast (∼1 ms) and short (<1ms) above > -20 mV and >-40 mV, respectively. Inactivation lasts for ∼50 ms and ∼100 ms, respectively. T-type Ca_vs are activated slowly (5 ms) but already above > -70 mV lasting for ∼5 ms. Their inactivation lasts for ∼25 ms (Stuart *et al.*, 2016).

Voltage-gated K^+ channels (K_vs) are the main regulators of dendritic, somatic and axonal excitability and are the most diverse class of voltage-gated ion channels with distinct functional properties. They possess a similar activation threshold as Na_vs but their activation time is substantially slower (Stuart *et al.*, 2016). Opening of K_vs leads to an efflux of K^+ ions, thereby repolarizing the cell. A-type K_vs form clusters on GC dendrites not overlapping with synapses and have been shown to attenuate the fast AMPAR-mediated component of the EPSP, while not affecting NMDAR-mediated depolarization (Kollo *et al.*, 2008; Schoppa, 2006a; Schoppa *et al.*, 1998). A-type K_vs reportedly also regulate the ability of dendritic spikes to propagate out of a branch to infiltrate neighboring branches in CA1 PCs (Cai *et al.*, 2004). In contrast, the inward rectifier K^+-channel Kir2.3 is specifically clustered in GC spines and may be involved in formation of their resting membrane potential (Inanobe *et al.*, 2002).

Canonical transient receptor potential channels (TRPCs), a subfamily of the TRP channel family, are non-selective Ca^{2+} permeable cation channels. Their activation mechanism is poorly understood but opening leads to membrane depolarization and sustained increase in intracellular Ca^{2+} (Birnbaumer, 2009). In GCs spines, TRPC1 and 4 are activated downstream of NMDAR and contribute to long-lasting depolarizations and slow synaptic transmission (see 1.2.5, Stroh *et al.*, 2012).

Interaction between all the ion channels being present on the synapse and the dendritic shaft, together with passive properties, shape the amplitude and kinetics of the postsynaptic potential. They are also key players when it comes to the dendritic integration of multiple postsynaptic potentials.

1.2.4 Dendritic integration

In dendrites, chemical signals arriving at the input synapses are translated into electrical postsynaptic signals. They were formerly seen as simple passive conductors of this postsynaptic activity. However, already the drawings of Santiago Ramon y Cajal (1904) showed a striking diversity of dendritic patterns and suggested an equal vast diversity of computational functions (Payeur *et al.*, 2019). This was confirmed by research in the past decades, revealing that dendrites are not only capable of different types of signal integration and transformation, including interaction with bpAPs and dendritic spike generation, (Stuart and Spruston, 2015) but can also generate synaptic output in some subtypes of neurons (Ludwig and Pittman, 2003).

Dendrites are capable of sublinear, linear, and supralinear integration governed by active and passive dendritic properties that are associated with various neuronal computations like e.g. spatial and temporal pattern discrimination. It is important to note that active integration is always preceded by passive integration until the threshold of the involved voltage-gated ion channels is reached. Since each input reduces the difference between membrane potential (V_m) and reversal potential (E_{rev}) and thereby reduces the driving force, clustered input without involvement of active conductances leads to sublinear summation (passive single compartment model). More distributed input to different electrical compartments, on the other hand, will produce more linear integration. Additionally, temporal coincidence of coactivated synapses together with synaptic strength determine the gain of a dendritic operation. The absolute

location of the inputs on the dendrite can also determine their impact. Dendritic branching effectively decreases the membrane resistance, acting like a shunt for current flow. This shortens the length constant, making summation of multiple inputs less effective. The neuronal membrane impedance (resistance depending on reactance, i.e. phase differences of voltage and current; Skilling, 1965; Middendorf, 1965) determines the change of the membrane potential in response to input currents and it increases with thinning dendrites in greater distance from the soma, what leads to larger (local) EPSPs (Tran-Van-Minh *et al.*, 2015; Dewell and Gabbiani, 2018). This passive input/output relationship (I/O) is fundamentally changed by the presence of voltage-gated ion channels. While clustered input leads to sublinear summation in the passive single compartment model, it actually leads to a higher localized depolarization of the dendrite allowing to reach the threshold for active conductances. The number and distribution of voltage-gated ion channels varies greatly between neuron types and even in a single dendritic tree enabling dendritic compartmentalization. For example, fine dendrites with AMPARs and Na_vs have high impedance but a rapid membrane time constant, resulting in local dendritic EPSPs substantially larger and faster than at the soma. This makes them act as coincidence detectors, as temporally and locally coincident inputs are boosted (Losonczy and Magee, 2006; Stuart *et al.*, 2016). Starburst amacrine cells, axonless interneurons in the retina, comprise ≥20 functionally distinct dendritic compartments that release GABA triggered by different light directions. This dendritic direction selectivity is caused by their intrinsic morphological and biophysical characteristics together with non-uniform excitatory input and lateral inhibition between starburst amacrine cells (Poleg-Polsky *et al.*, 2018). In contrast, e.g. hippocampal CA1 PCs can normalize input at different dendritic locations by increasing synaptic strength with distance from the soma. This leads to so called dendritic democracy where every input has the same “vote” deciding whether to generate axonal output (Hausser, 2001; Magee and Cook, 2000). Compartmentalization leads to an **information selection** as it distinguishes between dendritic local signals and somatic communicated signals. In the classical neuron, that generates output only at the axon hillock, the information held by dendrites is different from what is communicated to other neurons. Dendritic compartments are also differentially engaged by neuromodulation and inhibitory inputs modifying the flow of information or **routing information** (Payeur *et al.*, 2019). Voltage

activation of conductances cannot only boost EPSP amplitudes but can result in threshold-dependent dendritic spikes mediated by either Na_Vs, Ca_Vs or NMDARs (Piskorowski and Chevaleyre, 2012; Tran-Van-Minh *et al.*, 2015). In PCs, dendritic Ca^{2+}-spikes have been shown to be necessary for sensory perception. They can be elicited by synaptic input or bpAPs and not only mediate plasticity via local Ca^{2+} influx but can also have a direct computational aspect (Manita *et al.*, 2017). In the hippocampus, CA1 PCs get input to distal dendrites from the entorhinal cortex, while intrahippocampal input from CA3 PC arrives more proximally. Distal inputs alone generate dendritic spikes that fail to propagate to the soma. However, if input to the proximal dendrite arrives in the same time window, it can facilitate the propagation of the dendritic spike to the soma, resulting in AP generation. This biophysical interaction is called **gating** and can function as a coincidence detector (Katz *et al.*, 2007). Dendritic spikes are required for **information multiplexing** as one spiking output can concomitantly represent multiple inputs. In this context, Friedrich *et al.* (2004) showed multiplexing in zebrafish MCs, where the odor category is encoded by wave-like gamma oscillatory population activity, whereas precise odor identity is encoded by neurons within the same population but by exactly phase-locked spikes without time shift.

Being the determinant for reaching AP threshold, dendritic integration is, together with synaptic placement and strength, and spike threshold a critical determinant of neuronal computations (Tran-Van-Minh *et al.*, 2015). It becomes particularly important when the output is also mediated by dendritic release, where, in contrast to the classical neuron described above, multiple inputs can be translated into multiple outputs directly from dendritic synapses (Ludwig, 2005). Dendritic release of various neurotransmitters is a widespread phenomenon all across the brain. GABA and glutamate, that build the focus of our research, act as retrograde transmitters in the hippocampus, cortex, cerebellum and in our region of interest, the OB (Ludwig *et al.*, 2016). The mechanisms governing dendritic release are more diverse than seen in the axon but all dendritically releasing cells of the OB, including OB GCs, show axon-like Ca^{2+}-dependent neurotransmitter release (see 1.2.2, Stuart *et al.*, 2007). To conclude, all the above mentioned mechanisms of dendritic integration leading to the opening of Ca^{2+}-permeable channels might directly influence dendritic neurotransmitter release. Especially local compartmentalized dendritic events might directly be translated into localized release, where already passive

subthreshold synaptic potentials can lead to opening of LVACCs and active conductances can lead to dendritic spike initiation triggering release of various extent. Thus, passive cable properties, as well as density and kinetics of voltage-gated channels together with dendritic morphology govern dendritic spike initiation and propagation and thereby also effect dendritic neurotransmitter release (Ludwig, 2005).

1.2.5 Dendritic integration in olfactory bulb granule cells

In contrast to their output that relies on reciprocal dendrodendritic synapses with MC/TCs (Nagayama *et al.*, 2014), input to GCs is much more diverse. Inhibitory input to GCs is equally prominent as excitatory input and targets their soma and their whole dendritic tree, including spines (Burton, 2017). This inhibitory input arises from dSACs (see *1.1.2.2*) and from centrifugal GABAergic projections from the basal forebrain, namely the magnocellular preoptic nucleus and the medial half of the horizontal limb of the diagonal band of Broca (Gracia-Llanes *et al.*, 2010). The latter also sends cholinergic projections modulating GC excitability (Pressler *et al.*, 2007). Additionally, GCs receive noradrenergic innervations from the pontine nucleus locus coeruleus that is important for neonatal odor preference learning and odor processing in mature animals. Thereby, GCs are excited via the α1 and inhibited via the α2 receptor (Nai *et al.*, 2010).

However, the by far most numerous synapses onto GCs are from MC/TC lateral dendrites. They reportedly provide kinetically slow, short-term depressing, AMPAR- and NMDAR-mediated excitatory input to the distal apical dendrites of GCs in the EPL (Balu *et al.*, 2007; Dietz and Murthy, 2005; Isaacson, 2001; Schoppa, 2006a). Additionally, GCs receive excitatory axodendritic input to their proximal somatodendritic domains (in GCL, IPL and MCL) by MC/TC axon collaterals and centrifugal fibers from the OC. This proximal spines are purely postsynaptic and inputs have been shown to be faster, facilitating and predominantly AMPAR-mediated (Schoppa, 2006a; Balu *et al.*, 2007; Boyd *et al.*, 2012; Markopoulos *et al.*, 2012; Halabisky and Strowbridge, 2003). The centrifugal inputs originate from both the AON and the APC (Markopoulos *et al.*, 2012; Boyd *et al.*, 2012; Oettl *et al.*, 2016). Several studies suggest, that this proximal input is far more effective in eliciting APs in GCs and even doubt that distal input can elicit APs at all (Halabisky and Strowbridge, 2003; Pressler and Strowbridge, 2017). All these studies are based on somatic measurements, what, due to electrotonic attenuation, causes a slowed down and attenuated

representation of distal inputs. However, as GCs are axonless, the soma is not necessarily the mainstay of dendritic integration and the impact of dendrodendritic distal inputs on localized dendritic integration might be more substantial. Ca^{2+}-imaging provides a better picture of what happens directly at the input site (see *1.3.1*). Indeed, Bywalez *et al.* (2015) describe spine spikes that are restricted to the spine head and are mediated by fast Na_vs. They even increase in Ca^{2+}-signal amplitude with distance from soma and elicit single spine EPSPs with constant amplitudes independent from input location. Stronger activation results in globally propagating dendritic signals that encompass both low-threshold Ca^{2+}-spikes (LTS) and APs (Egger *et al.*, 2003; Egger *et al.*, 2005). Dendritic Na^+-spikes, restricted to distal ramifications and measurable at the soma in the form of spikelets, have been shown in frog, turtle, rabbit and mouse (Pinato and Midtgaard, 2005; Zelles *et al.*, 2006; Burton and Urban, 2015; Mori and Takagi, 1978). Of note, being axonless, every AP in GCs is a dendritic Na^+-spike, but spikelets indicate a Na^+-spike restricted to a certain part of the dendrite. LTS and spikelets are additional and more global indicators of substantial impact of distal dendrodendritic inputs. I conclude that GC distal apical dendrites are excitable in multiple ways and describe them in more detail in the following.

GC spines have approximately a 10-fold volume of conventional spines, an unusual long neck (R_{neck}∼1.42 GΩ) and contain both presynaptic and postsynaptic machinery. They have distinct computational properties and can act as largely independent units that create synaptic output on their own via an electrically and chemically decoupled Na^+- spine spike. In more detail, local Na_v activation by AMPA conductance boosts Ca^{2+} entry into GC spines through HVACCs and NMDARs triggering synchronous and asynchronous GABA release directly from the reciprocal spine (Bywalez *et al.*, 2015; Shepherd *et al.*, 2007; Lage-Rupprecht *et al.*, 2019; Woolf *et al.*, 1991a). One pair of MC/TC and GC only have one or two synaptic contacts (Woolf *et al.*, 1991b). Therefore, the highly localized Na^+- spine spike mediates only self-inhibition, while reaching the threshold for global spikes also represents the onset of lateral inhibition between different MC/TCs. The T-type Ca_vs dependent LTS and the high-threshold Na_v-dependent AP have been shown to both spread globally throughout the dendritic tree and into the spines and are likely to boost widespread GABA release governing lateral inhibition (Egger *et al.*, 2003; Egger *et al.*, 2005). While both global activation modes seem to propagate equally well, Egger (2008) shows

that both dendritic and spine Ca^{2+} signals mediated by an AP are significantly larger, putatively triggering stronger GABA release. A very recent study calculated the AP initiation zone of GCs (in 14 – 25 days old rats) to be in the proximal apical dendrite, below the EPL in a distance of < 100 µm from the soma (Pressler and Strowbridge, 2019). Another characteristic feature of GC APs is a long lasting depolarization (LLD) following the Na^+ peak (Hall and Delaney, 2002). NMDAR-mediated activation of TRPC1/4 leads to a plateau current, mediated by the nonspecific cation conductance I_{CAN}. This triggers slow global Ca^{2+} entry most likely via T-type Ca_Vs, putatively leading to asynchronous GC neurotransmitter output (Egger, 2008; Stroh *et al.*, 2012). Of note, *in vivo*, sensory input to the OB evokes only long-latency and sparse AP firing in GCs (Burton, 2017; Cang and Isaacson, 2003; Kato *et al.*, 2012).

In conclusion, all these modes of activation could contribute to different levels and time courses of release in GCs, thus they greatly increase their computational power. One task of this thesis is to investigate the conditions and exact number of activated spines necessary for their generation and to find further evidence for the ability of distal dendrodendritic inputs to excite GCs to AP threshold.

1.3 Two-photon photostimulation

2-photon (2P) microscopy was introduced by Winfried Denk and colleagues in 1990 (Denk *et al.*, 1990) and its first use for Ca^{2+} imaging in the nervous system was described 4 years later (Denk *et al.*, 1994). In 2P microscopy, two low-energy near-infrared photons are being absorbed simultaneously within a femtosecond time window. The energy of the two photons sums up and produces a transition of the atom, ion or molecule (e.g. a fluorescent molecule or a caged neurotransmitter, see *1.3.1* and *1.3.2*) into a higher-lying state. 2P absorption is proportional to the square of the optical input intensity making 2P excitation a nonlinear process. Advantages over confocal or one-photon excitation, where excitation illuminates the specimen also above and below the focal plane, comprise less scattering in brain tissue, high-sensitivity, localization of excitation due to exclusive excitation in one diffraction-limited focal volume and therefore no out-of-focus photodamage. Additionally, as 2P allows the use of near infrared photons, there is less scattering by naturally occurring chromophores. The necessary photon density can just be reached by pulsed lasers characterized by short pulses of about 100 fs duration. 2P laser scanning

microscopy generates an image or records changes in fluorescence by scanning a laser beam over the specimen. A photon multiplier tube (PMT) collects the photons emitted by a fluorescent molecule as it falls back into a lower-lying state. The fluorescence per pixel is measured and creates the image. As excitation is highly localized (see also Fig 4b), all photons collected by the PMT, independent from tissue scattering, can be used to generate an image (Svoboda and Yasuda, 2006).

1.3.1 Ca^{2+} imaging

In virtually every cell type in all organisms, intracellular Ca^{2+}, concentrated at ~50-100nM, can rise transiently during electrical activity to levels 100 times higher (Berridge *et al.*, 2000). Ca^{2+} influx is mediated by AMPARs, NMDARs, Ca_vs, nicotinic acetylcholine receptors, and TRPC channels. Inositol trisphosphate receptors and ryanodine receptors mediate release from internal stores. Ca^{2+} efflux is mediated by plasma membrane Ca^{2+}-ATPase, Na^{+}-Ca^{2+} exchanger, and the sarco-/endoplasmic reticulum Ca^{2+}-ATPase. Mitochondria can also take up and release internal Ca^{2+}. Ca^{2+} is an ubiquitous intracellular messenger that triggers exocytosis of vesicles in the presynapse, activity-dependent synaptic plasticity in the postsynapse, or regulates gene transcription in the nucleus (Grienberger and Konnerth, 2012).

The first Ca^{2+} indicators used for cellular Ca^{2+} were bioluminescent Ca^{2+}-binding photoproteins (Shimomura *et al.*, 1962; Ashley and Ridgway, 1968). In the past decades, a wide range of Ca^{2+} indicators were discovered and engineered, from bioluminescent protein a*equorin*, derived from marine organisms over chemical Ca^{2+} indicators to genetically encoded Ca^{2+} indicators (GECIs). The different dyes and indicators enable various loading techniques depending on the specific scientific question, from single-cell loading over “acute” network loading to the generation of transgenic animal lines where the indicator is expressed in whole cell populations. (Grienberger and Konnerth, 2012; Miyawaki *et al.*, 1997). In my thesis, Oregon Green™ 488 BAPTA-1 (OGB-1, Invitrogen), a fluorescent chemical cell impermeant Ca^{2+} indicator for single-cell loading, was used. Upon binding of Ca^{2+} OGB-1 exhibits an increase in fluorescence emission intensity with little shift in wavelength (Invitrogen OGB-1 Product Information; Thomas *et al.*, 2000). Ca^{2+} transients can be measured as ΔF over the baseline fluorescence F_0 ($\Delta F/F$).

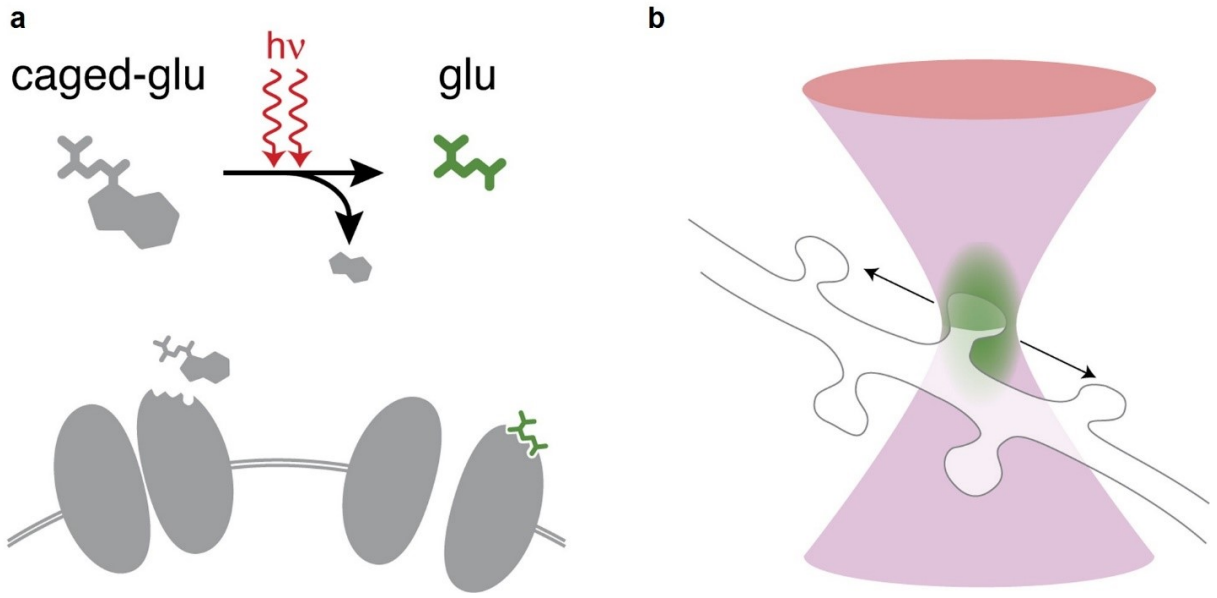

Fig 4. ***Two-photon glutamate uncaging at single spine resolution. a****: caged glutamate (glu) is photoconverted into its bioactive form by the near coincident absorption of two infrared photons. hv (planck constant x frequency) give the energy of the two photons* ***b****: because the photon density required for two-photon uncaging is only reached in a small focal volume, glutamate can be released with single-spine resolution. Modified from Judkewitz et al. (2006).*

1.3.2 Holographic glutamate uncaging

Caged glutamate has a photolabile protecting group that is removed by exposure to light, liberating the bioactive neurotransmitter and allowing it to bind to synaptic receptors (Fig 4a, Kramer *et al.*, 2009). The first caged neurotransmitter agonists were described in 1986 by Walker *et al.* (1986). They were activated by UV light leading to a broad rather global liberation. Combined with 2P illumination, neurotransmitter can be liberated at single spine level allowing precise activation of single synapses (Fig 4b, reviewed in Ellis-Davies, 2007). Here, we used DNI-glutamate●TFA [2(S)-2-amino-5-(4-methoxy-5,7-dinitro-2,3-dihydro-indol-1-yl)-5-oxo-pentanoic acid-glutamate trifluoroacetate] that has a 7.17 ± 0.84 times higher 2P uncaging efficiency than the, more widely used, MNI-glutamate. Uncaging of DNI-glutamate●TFA at single GC spines has been shown to closely mimic real synaptically evoked ΔF/F and EPSPs with respect to amplitude and kinetics (Chiovini *et al.*, 2014; Palfi *et al.*, 2018; Bywalez *et al.*, 2015). Combined with fast beam-deflecting mirrors, even multiple locations can be activated within a few milliseconds

(Judkewitz *et al.*, 2006; Losonczy and Magee, 2006). However, uncaging is still not simultaneous and restricted to a single focal plane. Simultaneous activation in 3D can be achieved by using a so-called spatial light modulator (SLM). An SLM contains computer controlled liquid crystals that can modulate the laser waveform, generating holographic light patterns or multiple beams. Holographic illumination together with 2P glutamate uncaging allows precise simultaneous multispot excitation (Lutz *et al.*, 2008; Nikolenko *et al.*, 2008; Gabor, 1948).

1.4 Aims of this study

OB GCs mediate lateral inhibition between MC/TCs implementing contrast enhancement and oscillatory synchronization across columns which respond to the same odorant (Fukunaga *et al.*, 2014; Peace *et al.*, 2017; Urban and Arevian, 2009). Understanding GC dendritic integration and determining the precise conditions that underlie global signals, up to the AP, is key to quantify the onset of lateral inhibition. Thus, the first aim of this study was, to facilitate multi-site uncaging in GCs, which allows to precisely control the number, location, and pattern of inputs and to use postsynaptic pharmacology independent of presynaptic MC/TC activation. Previous experimental work and simulation data on GCs predicted that only a high number of tightly temporally synchronized activated spines are able to elicit an AP (Pressler and Strowbridge, 2017; Bywalez *et al.*, 2015; Egger *et al.*, 2005). Together with the low spine density of OB GCs (Saghatelyan *et al.*, 2005), this yielded the need for true synchronous neurotransmitter uncaging and the possibility to target spines in different focal planes. In chapter 2, I describe the integration of a holographic projector module for synchronous high-resolution 3D multi-site 2P photostimulation into our existing 2P galvanometer-based 2D scanning microscope that meets these requirements.

Multi-site 2P neurotransmitter uncaging as a method for investigation of complex dendritic integration was already performed on principal neurons in the hippocampus (Grienberger *et al.*, 2014; Krueppel *et al.*, 2011; Makara and Magee, 2013) or cortex (Branco and Hausser, 2011) but to our knowledge never in interneurons, especially not in dendritically releasing interneurons. Thus, the aim for the second part of my thesis was to use the holographic projector to determine the transition from local to global signaling in OB GCs: (1) how many spines need to be activated to elicit non-local subthreshold spikes and APs, (2) how is spike generation influenced by dendritic

morphology and input patterns, (3) how do local and global signals interact, and (4) what are the molecular key players of dendritic integration in GCs.

2 A compact holographic projector module for high-resolution 3D multi-site two-photon photostimulation

2.1 Abstract

Patterned 2P photolysis via holographic illumination is a powerful method to investigate neuronal function because of its capability to emulate multiple synaptic inputs in three dimensions (3D) simultaneously. However, like any optical system, holographic projectors have a finite space-bandwidth product that restricts the spatial range of patterned illumination or field-of-view (FOV) for a desired resolution. Such trade-off between holographic FOV and resolution restricts the coverage within a limited domain of the neuron's dendritic tree to perform highly resolved patterned 2P photolysis on individual spines. Here, we integrate a holographic projector into a commercial 2P galvanometer-based 2D scanning microscope with an uncaging unit and extend the accessible holographic FOV by using the galvanometer scanning mirrors to reposition the holographic FOV arbitrarily across the imaging FOV. The projector system utilizes the microscope's built-in imaging functions. Stimulation positions can be selected from within an acquired 3D image stack (the volume of interest, VOI) and the holographic projector then generates 3D illumination patterns with multiple uncaging foci. The imaging FOV of our system is $800 \times 800\ \mu m^2$ within which a holographic VOI of $70 \times 70 \times 70\ \mu m^3$ can be chosen at arbitrary positions and also moved during experiments without moving the sample. We describe the design and alignment protocol as well as the custom software plugin that controls the 3D positioning of stimulation sites. We demonstrate the neurobiological application of the system by simultaneously uncaging glutamate at multiple spines within dendritic domains and consequently observing summation of postsynaptic potentials at the soma, eventually resulting in APs. At the same time, it is possible to perform 2P Ca^{2+} imaging in 2D in the dendrite and thus to monitor synaptic Ca^{2+} entry in selected spines and also local regenerative events such as dendritic APs.

2.2 Introduction

2P microscopy is now widely used in neuroscience (Svoboda and Yasuda, 2006). Its applications include structural and functional imaging (Denk *et al.*, 1994; Grienberger and Konnerth, 2012;

Fisher and Salzberg, 2015), and neuronal stimulation by photolysis of caged chemical compounds and activation of light-gated ion channels (Kramer *et al.*, 2009; Jerome and Heck, 2011). For example, the nonlinear 2P excitation process allows highly localized photolysis of caged neurotransmitters, thereby enabling targeted activation of single spines and effectively mimicking synaptic inputs onto a neuron. By activating multiple synapses with this technique, we can study how neurons integrate synaptic inputs to generate APs. Because the dendritic arbor of a neuron extends beyond a single plane, it is highly desirable to have three-dimensional (3D) access to individual synaptic sites to provide experimental flexibility. For example, 3D access to a sufficiently large volume with high spatial resolution will allow to investigate synaptic integration across dendritic bifurcations for any spatial arrangement of the dendrites of interest. Conventional laser scanning systems use galvanometer mirrors (Denk *et al.*, 1990) that deliver efficient beam steering with minimal power loss across a wide field-of-view (FOV) of the sample. The mirrors can be programmed to perform a raster scan or to follow an arbitrary path (Lillis *et al.*, 2008) and have a positioning time of ~ 100 μs. Resonant scanning systems (Fan *et al.*, 1999), which use a resonant mirror in one axis (fast axis) and a galvanometer mirror in the other axis, allow faster scan rates but are constrained to raster scans. Even faster beam steering (< 15 µs, Losavio *et al.*, 2009) is offered by two acousto-optic deflectors (AODs), which steer the laser beam without any mechanically moving parts. In these scanning systems, fast switching times from one stimulation site to another allow the near-simultaneous activation of multiple synapses in a physiologically relevant time window (~ 1 ms). While these scanning systems are constrained to two dimensions (2D), high-speed 3D scanning using a system of four AODs has been demonstrated (Duemani Reddy *et al.*, 2008; Kirkby *et al.*, 2010). However, this system is characterized by a low optical throughput (~ 18%) (Nadella *et al.*, 2016). Although such a system is useful for high-speed monitoring of neuronal activity by imaging fluorescent reporters (e.g. calcium indicators), so far it has not been applied to 2P uncaging because of this limitation in optical throughput. Simultaneous steering of multiple laser beams via holographic projection offers a solution (Go *et al.*, 2012; Go *et al.*, 2013; Nikolenko *et al.*, 2008; Nikolenko *et al.*, 2007; Dal Maschio *et al.*, 2010; Lutz *et al.*, 2008; Yang *et al.*, 2011; Anselmi *et al.*, 2011; Yang *et al.*, 2014a). High optical throughput is afforded by using a phase-only SLM to modulate the wavefront

of the laser beam to produce a target intensity distribution at the objective's focal plane. Phase holograms can produce spatial light patterns such as multiple diffraction-limited focal spots that are ideally suited for highly localized uncaging in synaptic integration studies. Such multi-focal patterns were initially used to demonstrate multi-site 2P glutamate uncaging in 2D (Nikolenko *et al.*, 2008; Nikolenko *et al.*, 2007; Dal Maschio *et al.*, 2010). Holographic projectors are inherently capable of generating multiple foci in 3D especially with computer-programmable SLMs. This has been shown with single-photon (1P) photolysis (Lutz *et al.*, 2008; Yang *et al.*, 2014a; Yang *et al.*, 2011; Anselmi *et al.*, 2011). We have also previously demonstrated holographic projection to perform multi-site 2P uncaging (Go *et al.*, 2013; Go *et al.*, 2012), which enabled us to stimulate multiple spines along dendrites in 3D with high spatial (transverse and axial) resolution. However, holographic projectors have finite spatial range or FOV for a desired resolution as quantified by the optical system's space-bandwidth product. To ensure effective 2P uncaging, we needed highly resolved focal spots and the trade-off between FOV and resolution resulted in a limited spatial coverage. Such trade-off does not necessarily apply to 1P uncaging since there is sufficient light energy (e.g. ultra-violet light) to photolyse caged molecules without requiring tight focusing. However, expanding the holographic FOV with 1P uncaging also means a less resolved uncaging system that does not necessarily target individual spines. While such a 1P uncaging system may be applicable for some applications, specific neurobiological questions that involve integration of synaptic inputs from individual spines require a highly resolved multi-site 2P uncaging system. Here, we extend the spatial coverage of a multi-site 2P uncaging system by integrating a compact holographic module into a commercial 2P laser scanning microscope. While our solution does not increase the holographic FOV, it enables us to use the microscope's scanners to reposition the holographic FOV across a wider spatial range whilst maintaining highly resolved focal spots. We integrated the hardware and software components of the module with that of the microscope's built-in functions (such as 3D rendering, arbitrary region of interest (ROI), zoom and panning functions) to perform synaptic integration experiments using the 3D image of the neuron's dendritic tree. From the 3D image of the dendrites, we can calculate an appropriate phase-only hologram to accurately produce multi-focal stimulation sites along any dendritic arborization. We demonstrate the functionality of the system with 2P glutamate uncaging

experiments at dendrites of cortical pyramidal neurons, targeting multiple spines in volumes of up to 70×70×16 μm^3 as dictated by the 3D morphology of the neurons we investigated (possible *z*-range up to 70 μm). Using the galvanometer mirrors, we can reposition the holographic FOV within an 800×800 μm^2 imaging FOV. We can stimulate a sufficient number of spines to evoke an action potential from the neurons' resting membrane potentials.

2.3 Materials and methods

Our setup consists of a holographic projector integrated into a commercial 2P galvanometer-based scanning system with an uncaging unit (Femto2D-Uncage, Femtonics Ltd., Budapest). The system is equipped with two femtosecond pulsed Ti:S lasers (Chameleon Ultra I and II, Coherent) and is capable of simultaneous uncaging and Ca^{2+} imaging at different wavelengths. We describe the design and alignment of the holographic projector, the integration of its software control into the commercial software package, and its application to 2P uncaging experiments *in vitro*.

2.3.1 Design of holographic projector attachment

The schematic of the system and the design of the holographic projector are shown in Fig 5. We inserted a polarizing beam splitter (PBS1) after the intensity attenuation optics and safety shutters, just before the entrance port of the 2P upright microscope (Fig 5a). Because the polarizations of the two lasers are perpendicular with respect to each other, PBS1 relays the uncaging beam to the holographic projector while transmitting the imaging beam. The uncaging beam is expanded by a 4*f* lens setup (L1, L2) to illuminate the 15.8×12 mm^2 window of a reflective phase-only SLM (X10468-03, Hamamatsu, Japan) at an angle of $\sim 18^{\circ}$ from the normal (Fig 5b). The SLM has a resolution of 800×600 pixels, but only the central 600×600 pixels are used to display the phase-only hologram (H0). A demagnifying 4*f* lens setup (L3, L4) reduces the uncaging beam width back to its original size setting the conjugate image of the SLM or hologram plane at the focus of L4 (H1). To efficiently couple this phase-encoded beam to the microscope, another appropriate 4*f* relay optics (L5, L6) has to be chosen such that the conjugate plane of the hologram (H1) is imaged on to the plane of the galvanometer scanning mirrors (GM) of the

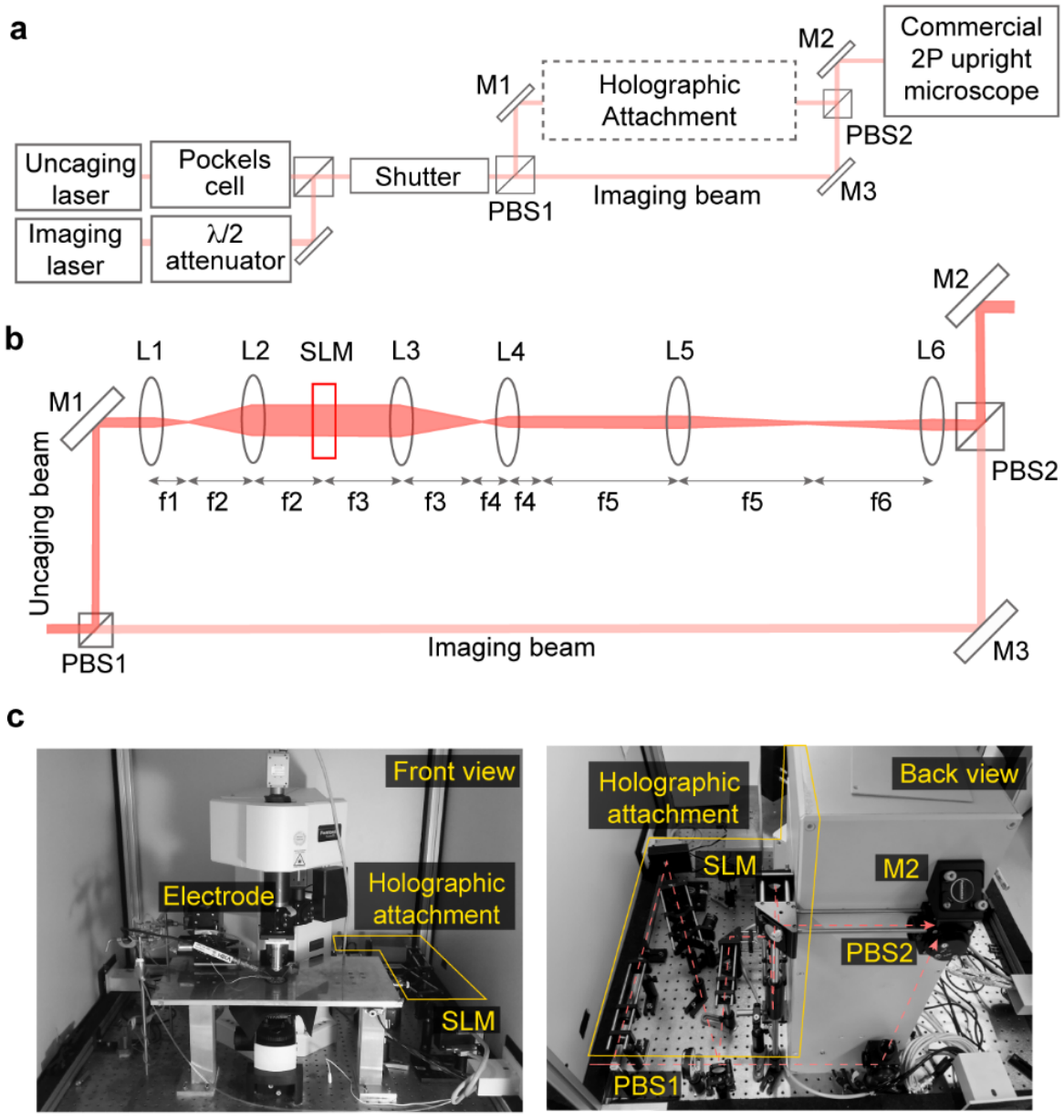

Fig 5. ***Optical setup of holographic projector attachment.***
a*: Schematic of the commercial two-photon microscope and the holographic attachment.* ***b****: Detailed schematic of the holographic projector attachment. PBS: polarizing beam splitter, M: mirror, L: lens, SLM: spatial light modulator, λ/2: half waveplate. H1: conjugate image of the SLM hologram (H0). Lenses: f1 = f4 = 30 mm; f2 = f3 = 100 mm; f5 = f6 = 500 mm.* ***c****: Photographs of the setup showing the front view of the commercial microscope (left), and the back view showing the holographic attachment (right).*

microscope. This setup ensures that all beams deflected by the phase hologram are contained within the area of the scanning mirrors. The distance from the GM unit to the entrance port of the commercial microscope is ~ 500 mm, determining the focal length of the 4*f* relay lenses L5

and L6. After lens L6, we placed a second polarizing beam splitter (PBS2) to recombine both the imaging and uncaging beams. Both beams are relayed onto the GM through the scan and tube lenses, and finally the objective lens (20×, NA 1.0, WPlan-Apo, Zeiss or 60×, NA 1.0 W, NIR Apo, Nikon). The scan lens and the tube lens of the microscope likewise image the hologram onto the back aperture of the objective lens. With the exception of L3 (diameter ⌀ = 50.8 mm), all optical components have a diameter of 25.4 mm and fit into a 30 mm cage system. As evident from Fig 5c, the holographic projector design is rather compact, requiring no more than 80×35 cm^2 base area.

2.3.2 Software control of holographic attachment

In our case, the commercial microscope comes with a MATLAB-based software package, MES (Femtonics Ltd.), which controls the microscope and acquires 3D images within the VOI set by the user. We developed a custom software plugin written in MATLAB (v2007b, Mathworks) to interface with the commercial software and to generate the corresponding hologram for the arbitrary positioning of multiple foci for uncaging. Fig 6a shows how the custom software interfaces with the commercial software and the rest of the system. For each focal plane in the VOI, the user first takes an image via the MES software, which stores the image and its metadata in the hidden global MATLAB workspace. The custom SLM software reads the acquired image and its pixel resolution. The user then positions the uncaging sites by specifying the *xy* coordinates on the graphical user interface (GUI, Fig 6b) or by positioning crosshairs on the image (Fig 6c). Next, the user adjusts the *z*-coordinates of the spots depending on their relative distance to the plane where the objective will be focused during photostimulation. These *xyz* coordinates are then used to calculate a hologram, based on the standard prism-lens superposition algorithm (Liesener *et al.*, 2000; Curtis *et al.*, 2002), which is displayed on the SLM (Fig 6d) via a digital video interface (DVI) using the PsychoPhysics Toolbox in Matlab. The phase hologram on the SLM is the phase, arg [$\psi(u, v)$], of the total input field, $\psi(u, v)$, described by

$$\psi(u,v)=\sum_{n=1}^{N} A_n \exp(2\pi i[au x_n + \beta v y_n + \gamma(x^2+y^2)z_n + \sum_{p,q} C_q^p(z_n) Z_q^p(u,v)]), \quad (1)$$

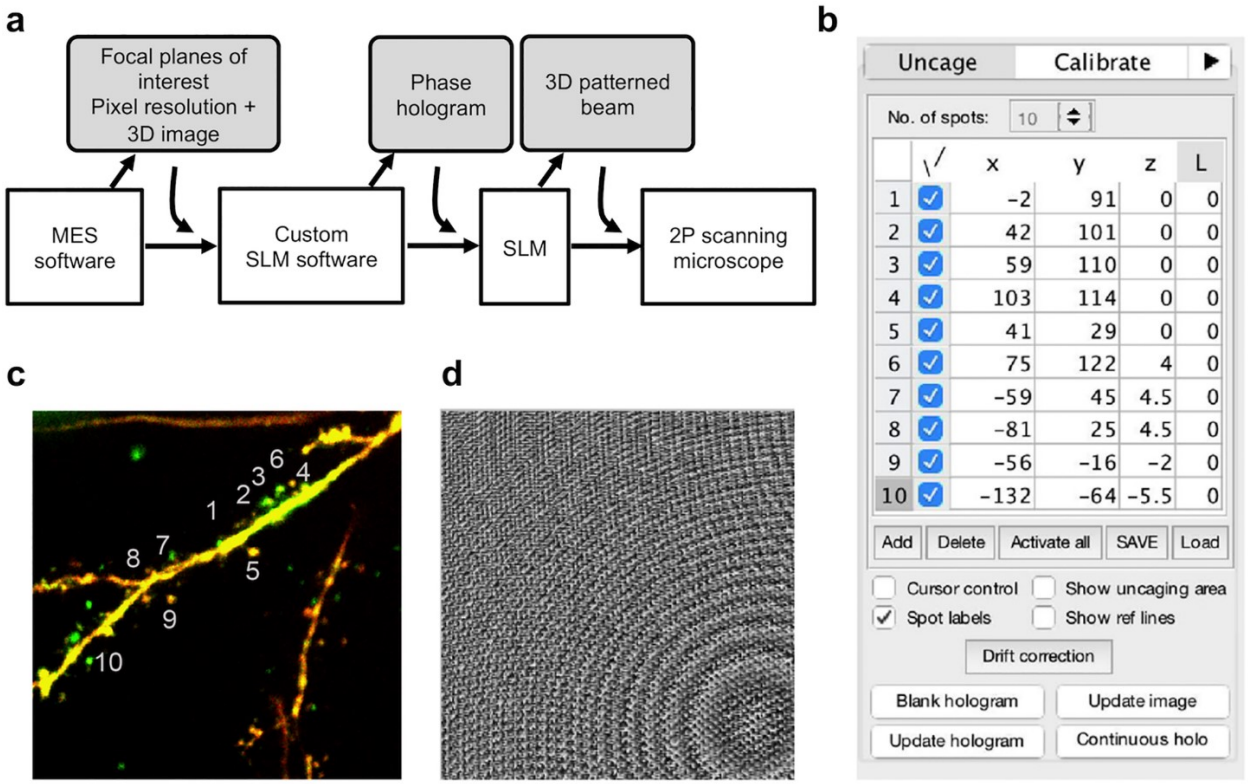

Fig 6. ***Software control of holographic projector.***
a*: Interfacing between our custom spatial light modulator (SLM) software and the rest of the system including the microscope's control software (MES), which gathers the pixel resolution.* ***b****: Custom software graphical user interface showing xyz-coordinates of uncaging spots. We use the last column to encode a Laguerre-Gaussian beam of charge "L" to align the center of the SLM with respect to the optical axis.* ***c****: Two-photon 3D image of a basal dendrite with multiple spines. Positions of uncaging sites in* ***b*** *are indicated.* ***d****: The corresponding 8-bit phase-only hologram for projecting the multiple uncaging spots in* ***b****.*

where A_n and (x_n, y_n, z_n) are the intensity weighting coefficient and 3D spatial coordinates, respectively, of the nth uncaging spot, (u, v) are Cartesian coordinates at the SLM plane with the center at the optical axis and α, β, γ are scaling factors which take into account the excitation wavelength, objective focal length and calibration adjustments (Go *et al.*, 2012; Golan *et al.*, 2009). $C_q^p(z_n)$ and $Z_q^p(u,v)$are the Zernike coefficients and polynomials, respectively, used to compensate for optical aberrations.

The SLM-generated excitation spots may be degraded due to optical aberrations introduced along the optical path. These aberrations can be mathematically represented by Zernike polynomials (Born and Wolf, 1980), which can be encoded onto the SLM in addition to the

calculated phase hologram. To correct for aberrations, the user simply has to adjust the coefficients for the Zernike polynomials in the custom software GUI (Fig S1a). The user may also correct for drift in the 2P image by adjusting the positions of the uncaging spots on the GUI.
The MATLAB code for the software plugin and details on how to use it in conjunction with MES are available at http://www.github.com/g0codes/holoMES.

2.3.3 Alignment and calibration of excitation spots

We used the imaging beam as a reference and aligned the uncaging beam to it via two alignment irises. For fine adjustment, we imaged 1 μm diameter fluorescent beads (Molecular Probes, Inc.) with the 60× objective using both lasers at 750 nm simultaneously but with a blank hologram displayed on the SLM. This double illumination produces two images of the beads if the uncaging beam is not completely aligned to the imaging beam. Fine adjustments in alignment were made by adjusting the direction of the uncaging beam via relay optics just before PBS2 in Fig 5a.
To calibrate the position of the holographic excitation spots, we used mirror images of a bead resulting from scanning a patterned uncaging beam onto the bead sample (without the imaging beam). For instance, imaging a single fluorescent bead with a two-foci uncaging beam results in two mirror images. We imaged fluorescent beads this way while adjusting the *x*, *y* and *z* scaling and rotation factors of the hologram until the mirror images of the beads on the 2P image were centered on the uncaging cross hairs on the GUI (Fig S1b).
We measured the 2P point spread function (PSF) of our system by imaging 100 nm fluorescent beads (Molecular Probes, Inc.) with the 60× and 20× objective lenses, using both imaging and uncaging lasers separately.

2.3.4 Acute brain slice preparation and electrophysiology

All experimental procedures were approved by the University of Regensburg Ethics Committee (Egger Ethics ID: AZ 55.2-1-54-2532.2-58-11). Sagittal somatosensory cortex acute brain slices (300 μm thick) from juvenile rats (postnatal days 11-18, Wistar) were incubated at 33˚C for 30 min in ACSF bubbled with carbogen and containing (in mM): 125 NaCl, 26 $NaHCO^2$, 1.25 NaH^2PO^4, 20 glucose, 2.5 KCl, 1 $MgCl^2$ and 2 $CaCl^2$. Recordings were performed at room temperature (22˚C). Patch pipettes (pipette resistance 4-5 MO) were filled with an intracellular solution containing (in

mM): 140 K gluconate, 10 HEPES, 10 NaCl, 0.5 $MgCl^2$, 4 Mg-ATP, 0.4 Na^3-GTP, 0.1 OGB-1 and 0.04-0.06 Alexa Fluor 594, pH 7.3.

Electrophysiological recordings were made using an EPC-10 amplifier with Patchmaster v2.60 software (HEKA). Layer 2/3 pyramidal neurons were patched in whole-cell configuration and held in current-clamp mode close to a membrane potential of -60 to -75 mV. Electrophysiological data were analyzed using Igor Pro (Wavemetrics). Somatic recordings of both single spine stimulations and the different combinations of multi-site uncaging were averaged for each stimulation type (n = 2).

2.3.5 Two-photon imaging and glutamate uncaging

To visualize a neuron, we loaded 100 μM OGB-1 (Ca^{2+} indicator, Life Technologies) and 40-60 μM Alexa Fluor 594 (Life Technologies) into the patch pipette and patched the cell in whole-cell configuration. After waiting for the dye to diffuse into the dendrites (~ 20 mins), a 2P image stack of the neuron was recorded by the commercial software (MES, Femtonics) with the imaging laser set to an excitation wavelength of 835 nm. We loaded 1 mM DNI-caged glutamate (DNI, Femtonics Ltd.) via a closed perfusion circuit with a total volume of 12 ml ACSF. The solution containing the caged glutamate was washed in for 10 min prior to photostimulation. The uncaging wavelength was 750 nm while exposure time was 0.5-1.5 ms and laser power was adjusted individually for each experiment to elicit physiological responses. Using the custom-written SLM software, uncaging spots were positioned in 3D at a distance of ~ 0.5 μm from spine heads. Z-positions of the uncaging spots were first estimated from the 3D image, then further adjusted to obtain an optimal EPSP response. Positions were checked before each measurement and, if necessary, readjusted to account for drift. Imaging of uncaging-evoked Ca^{2+} signals in selected spines was carried out as described earlier (Bywalez *et al.*, 2015). During simultaneous Ca^{2+} imaging and photostimulation, imaging was started 700 ms before the uncaging stimulus during which the scanning mirrors were fixed. For simultaneous multi-site photostimulation in synaptic integration experiments, the total uncaging power and the number of foci were kept constant. “Superfluous” foci, i.e. foci that were not needed as stimulation spots at a given time of an experiment, were excluded by positioning them just outside the holographic FOV, such that they would fall off the optics and not be projected onto the sample.

2.4 Results

To characterize the properties of our holographic 2P microscope, we acquired 2P images of 1 μm fluorescent beads using the uncaging beam. Fig 7a shows the normalized fluorescence F at an uncaging site as a function of the number of foci N. It follows the predicted inverse relationship, $1/N^2$ (Daria *et al.*, 2009) (fit: $F = 1/N^{1.8\pm0.02}$, $R = 0.97$). 2P excitation is a nonlinear process resulting in a quadratic relation between the fluorescence and excitation intensities (Zipfel *et al.*, 2003). We used this relationship to quantify the uncaging power at an uncaging site from the fluorescence intensity of a bead. To keep the uncaging power per focus constant despite changes in N, we fixed the power at a high level and increased N. Fig 7b shows how the uncaging power per stimulation spot remains constant as "superfluous" foci were moved outside the holographic FOV. The error in power, δP, is calculated as $\delta P = 0.5\delta F/P$. The PSF of 2P excitation with the holographic module measured by imaging 100 nm fluorescent beads shows a full width at half maximum (FWHM) of 0.49 μm (60×) and 0.64 μm (20×) in the lateral direction and 2.7 μm in the axial direction for both lenses. Fig 7c shows the measured axial and transverse PSFs for both the 60× and 20× objective lenses used in our experiments.

We next characterized the holographic FOV—the region within the ROI over which uncaging spots can be positioned in 2D. If an uncaging spot is positioned away from the center of the ROI, the uncaging beam deviates from the optical axis. Beyond a certain deviation, the beam falls off from the relay optics in between the SLM and the scanning mirrors. Fig 7d and 7e show the normalized uncaging power as a function of lateral distance along the x-axis for 60× and 20×, respectively. From these plots, we can see that the positioning range of the holographic spots is around 30×30 μm^2 when using a 60× objective and 70×70 μm^2 for the 20×. The imaging FOV for the 60× objective is 220×220 μm^2, while for the 20×, it is 800×800 μm^2. However, areas within the imaging FOV yet outside the holographic FOV can be easily accessed by steering the uncaging beam using the galvanometer mirrors. In Fig 7d and 7e, when the uncaging beam was steered to

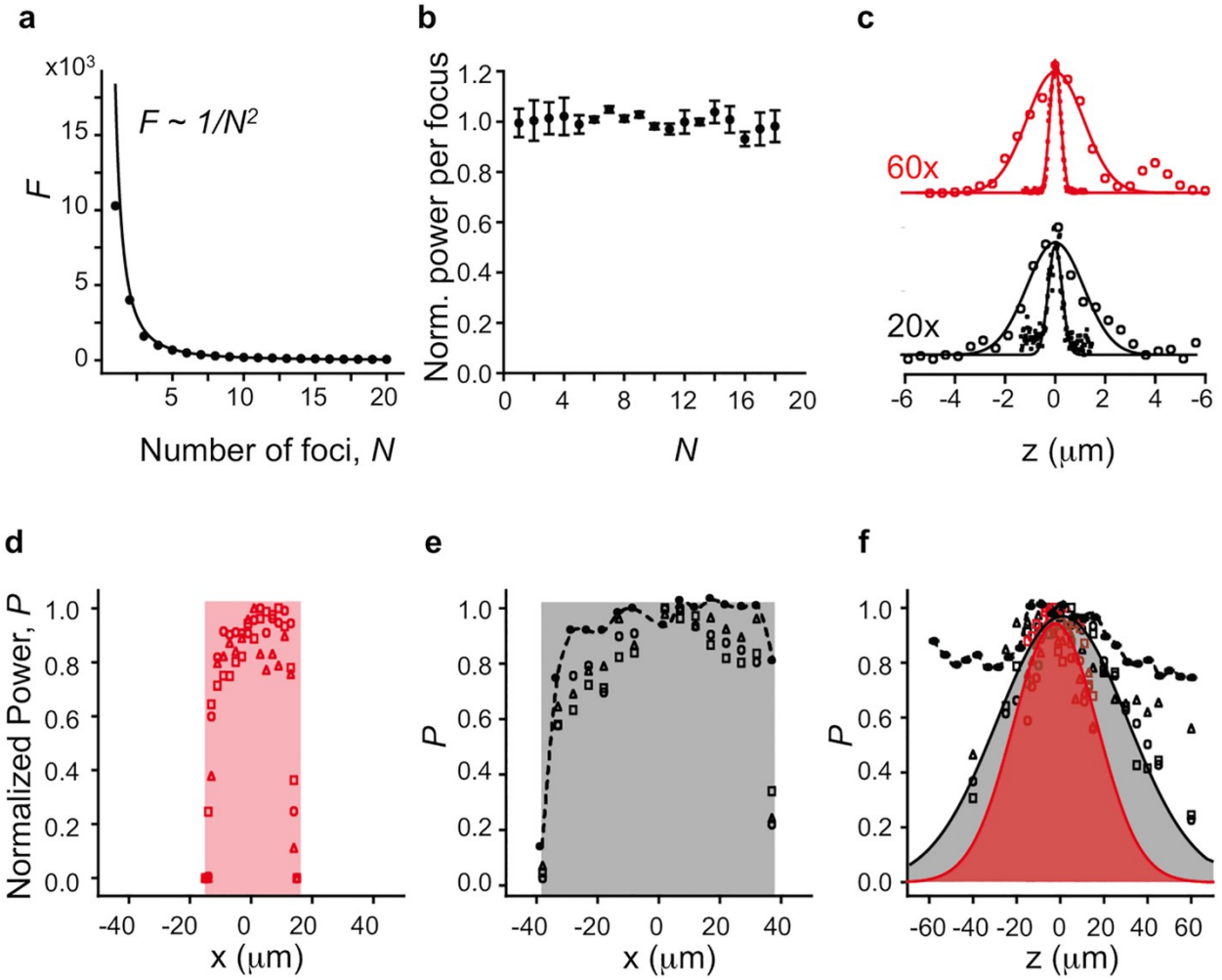

Fig 7. ***Performance of the holographic system.***
a*: Normalized fluorescence intensity of a focal spot as a function of number of spots, N* ***b****: Normalized uncaging power per spot as a function of number of stimulation spots. Number of foci is kept constant and superfluous foci are moved outside of the holographic FOV in transverse direction.* ***c****: Measured PSF of two-photon excitation in the axial (○) and transverse (●) directions for 60× and 20× objective lenses.* ***d****: Normalized power as a function of displacement along the x for 60× for FOV centered at (0, 0) (○), (−100, −100) μm (Δ) and (100, 100) μm (□).* ***e****: Normalized power as a function of displacement along the x for 20× for FOV centered at (0, 0) (○), (−300, −300) μm (Δ) and (300, 300) μm (□). Filled circles with dashed line denote power distribution after amplitude weighting for FOV centered at (0, 0).* ***f****: Normalized power as a function of displacement along the z for 60× (red markers in red area) and 20× (black markers in gray area) for FOV centered at different coordinates specified in* ***d*** *and* ***e****. Solid lines denote empirical Gaussian fit used for amplitude weighting. Filled circles with dashed line denote power distribution for 20× after amplitude weighting for FOV centered at (0, 0).*

other regions (e.g. to (-100,-100) μm and (100,100) μm for 60× and (-300,-300) μm and (300,300) μm for 20×) using the galvanometric mirrors, the holographic FOV was not significantly changed. Within the holographic FOV, spot intensity decreases with lateral displacement as a consequence

of a spatially varying diffraction efficiency due to the SLM being pixelated. The intensity decline is in the shape of a sinc-squared function (Golan *et al.*, 2009). This non-uniform diffraction can be compensated for by inversely weighting the amplitude during hologram calculation. Fig 7e shows the amplitude weighted power distribution for the 20× objective with the uncaging beam at the center of the imaging FOV.

To characterize light efficiency in the axial direction, we moved the spot along the *z*-axis and measured the decline in uncaging power. Fig 7f shows the normalized uncaging power as a function of axial distance for both 60× and 20× objectives for different positions of the uncaging beam ((-100,-100), (0,0), (100,100) for 60× and (-300,-300), (0,0), (300,300) for 20×). To counteract this attenuation, the amplitude can be inversely weighted at each position during hologram calculation. Fig 7f shows the amplitude weighted power distribution for the 20× objective with the uncaging beam at the center of the imaging FOV.

The results above show that for the parameters used in our system, photostimulation spots can be generated with a light efficiency of at least 50% (80% with power weighting) over a volume of 70×70×70 μm^3 when using a 20× objective lens. In our integration experiments (below), the power variation was not significant across the VOI we selected (*x*, *y*, *z* range ~ 16 μm) and power weighting was not implemented.

We then used the holographic projector to perform 2P glutamate uncaging at spines of layer 2/3 pyramidal neurons in brain slices of the somatosensory cortex. Fig 8 shows a representative synaptic integration experiment. A 2P image stack projection of a layer 2/3 pyramidal cell labeled with OGB-1 taken with a 60× objective is shown in Fig 8a. From the image, we selected a specific VOI containing a basal dendrite with a high density of spines. This dendrite featured an arborization with multiple bifurcations that extended to higher-order dendrites with partial overlap along the axial direction (see also Videos S1 and S2 for 3D visualization). We then selected spines and laterally positioned the uncaging sites close to the spines (~ 0.5 μm). The inset in Fig 8a shows the *z*-projection of the selected VOI displaying the basal dendrite and the locations of the uncaging sites. Fig 8b shows an *xz*-projection of the selected VOI and its 3 representative planes at $z = -5$ μm, $z = 0$, and $z = +5$ μm. Fig 8c shows the somatic EPSPs of individual uncaging events at spines spanning an axial range of 10 μm. The responses from an increasing number of

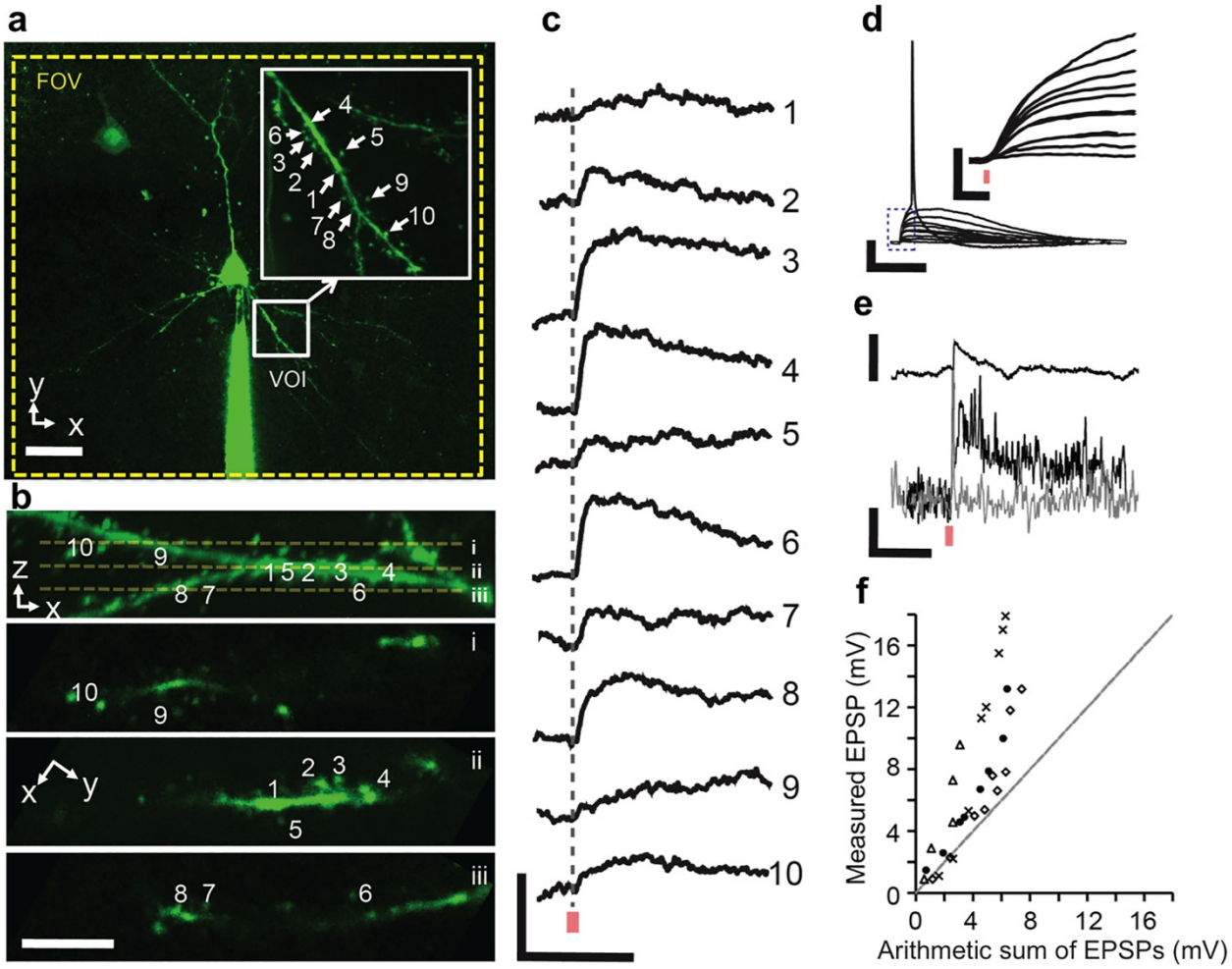

Fig 8. ***Representative synaptic integration experiment.***
a*: Two-photon image of a layer 2/3 pyramidal neuron labeled with OGB-1 taken with a 60× objective. Inset shows a high magnification flattened multi-stack image of the volume-of-interest (VOI). FOV: field-of-view. Scale bar: 20 µm.* ***b****: VOI displayed as an xz-image with 3 representative image planes (i: z = −5 µm; ii: z = 0; and iii: z = + 5 µm. Scale bar: 5 µm.* ***c****: Somatic EPSPs of individual uncaging events (red bar indicates time point of 2P glutamate uncaging). Scale bars: 1 mV, 40 ms.* ***d****: Uncaging responses with increasing number of simultaneous uncaging sites. Scale bars: 20 mV, 50 ms. (Inset) Magnified EPSP rise times for increasing number of uncaging sites. Scale bars: 5 mV, 5 ms.* ***e****: Representative individual uncaging-evoked EPSP (top) and Ca^{2+} transient (ΔF/F) (bottom) measured at spine 4 (black) and nearby dendrite (gray). Scale bars: 2 mV, 20%, 500 ms.* ***f****: Input-output plot (n = 4) of measured multi-site uncaging response against the arithmetic sum of individual uncaging events. Dashed line indicates linear summation, black circles represent data from* ***a*** *while all other markers represent data from other experiments.*

simultaneous uncaging sites are shown in Fig 8d. An AP is evoked following simultaneous uncaging at all 10 spines. The inset shows the rising phase of the responses with a higher

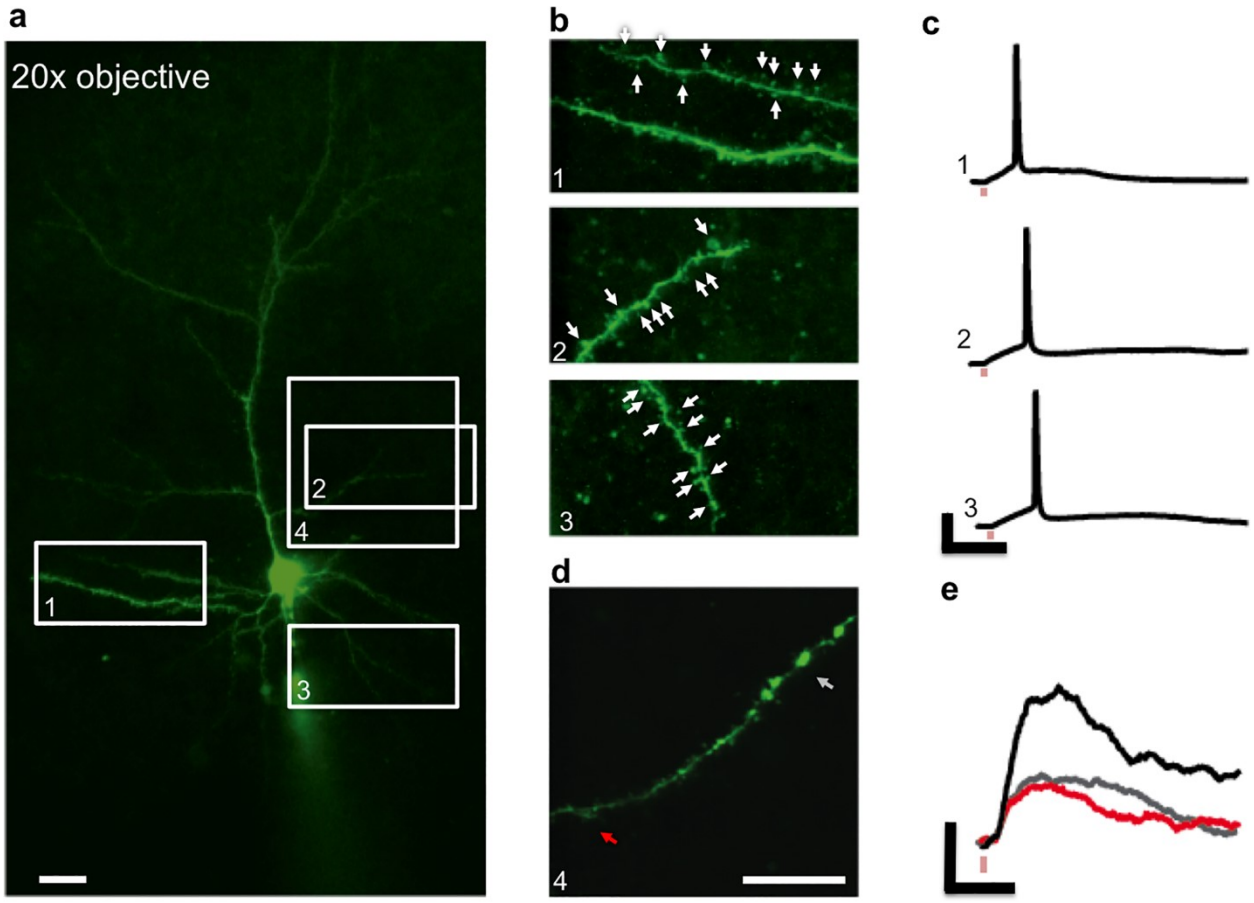

Fig 9. ***Synaptic integration experiment with a larger VOI.***
a*: Two-photon image of a layer 2/3 pyramidal neuron labeled with OGB-1 using a 20× objective lens results in a larger field-of-view. Scale bar: 20 µm.* ***b****: Uncaging volumes-of-interest (VOIs 1, 2 and 3) targeting specific dendrites corresponding to regions indicated in* ***a****. Scale bar: 20 µm.* ***c****:Somatic action potentials evoked when simultaneously uncaging at all sites (8-10) within corresponding uncaging VOIs in* ***b****. Scale bars: 20 mV, 50 ms.* ***d****: Uncaging VOI 4 (region indicated in* ***a****) showing a dendrite that extends 16 µm along the axial direction. Scale bar: 20 µm.* ***e****: Evoked EPSPs in VOI 4 when two sites are activated separately (red and grey traces) and simultaneously (black trace). Scale bars: 1 mV, 50 ms.*

temporal resolution. Note that only a slight increase of the rise time in the initial phase is observed with increasing number of activated spines.

To demonstrate simultaneous photostimulation and Ca^{2+} imaging, we imaged one plane in the VOI while uncaging with holographic spots. Fig 8e shows a representative individual uncaging EPSP and the corresponding Ca^{2+} transient at the spine (black trace) and dendrite (gray trace). While Ca^{2+} influx is detected at the spine, no change in basal Ca^{2+} concentration is detected at the dendrite. That is, upon uncaging at a single spine, Ca^{2+} invades the spine independent of the

dendrite and an individual somatic EPSP is evoked. Fig 8f shows an input-output (sI/O) plot from several experiments (*n* = 4 cells) comparing the uncaging-evoked EPSPs from simultaneous uncaging at multiple sites to the arithmetic sum of individual uncaging EPSPs. Note the supra-linear summation of simultaneous multi-site uncaging events.

Next, we show that we can use a lower magnification 20× objective lens to cover a larger VOI. In Fig 9a, we show that we are able to target multiple spines in different regions of the whole dendritic tree of a neuron by steering the uncaging beam using the galvanometer mirrors. Fig 9b shows uncaging VOIs targeting specific dendritic sections as indicated by the ROIs in Fig 9a. By uncaging at 8-10 sites in 2-4 *z* planes in each VOI (1 to 3), we can evoke an AP as shown in Fig 9c. A representative synaptic integration experiment in the 1st VOI is also shown in Fig S2. Fig 9d shows the 4th VOI, where we demonstrate a substantial functional *z* range by selecting two spines with an axial distance of 16 μm and activating them separately and simultaneously (Fig 9e).

2.5 Discussion

2.5.1 Characteristics of the holographic projector module

We have integrated a holographic projector module into a commercial galvanometer-based 2P microscope to introduce arbitrary multi-foci patterns in 3D. This is achieved by encoding a hologram on the excitation laser with a phase-only SLM. To relay the conjugate image of the hologram onto the back focal plane of the objective lens, we needed to use long focal length relay lenses (L5 and L6 in Fig 5b) to match the distance (≈ 500 mm) from the scanning mirrors to the input aperture of our commercial 2P laser scanning system. In the current setup, the positioning range of the holographic spots is limited (70×70 μm^2 for a 20× objective and 30×30 μm^2 for 60× objective) due to beam fall-off at the relay lenses. This range can be improved with the use of larger diameter lenses (e.g. ⌀ = 50.8 mm). A microscope with a shorter distance between input aperture and scanning mirrors will require relay lenses with shorter focal length, which can accommodate wide-angle steering of holographic beams and consequently increase the effective holographic FOV.

The current optical design of the holographic projector presents an advantage over our previous configuration (Go *et al.*, 2013; Go *et al.*, 2012) where the uncaging beam was not steered by the

galvanometer mirrors. In such a configuration, without a relay lens to limit the aperture, the holographic FOV is fundamentally limited by the diffraction efficiency of the SLM. When the SLM image is matched to the size of the back aperture of the objective, the holographic FOV is limited to $2dx_{max} \times 2dx_{max}$

$$dx_{max} = \frac{\lambda N_{pix}}{4NA}, \tag{2}$$

where N_{pix} is the pixel count in the $N_{pix} \times N_{pix}$ SLM display (Horst and Forde, 2008)[30]. Using the parameters of our system, we get a holographic FOV of 220 × 220 μm^2. Although this FOV is wide, the efficiency of first-order diffraction spots decreases with lateral displacement from the optical axis and follows a sinc-squared-shaped envelope (Horst and Forde, 2008; Golan *et al.*, 2009). This non-uniformity can be corrected via inverse amplitude weighting, but this correction in turn reduces the average diffraction efficiency. With the current system, a wide holographic window is conserved in the sense that the holographic FOV can be easily repositioned across the entire imaging FOV with the galvanometer mirrors, allowing for targeted positioning of off-center holographic spots without repositioning the sample. Moreover, the average diffraction efficiency across the smaller holographic FOV is higher. In addition, power loss to far off-axis regions which will have lower average diffraction efficiency can be compensated for by increasing the laser power (or total power of the multiple foci).

The SLM has the unique capability to correct for optical aberrations. We found our holographic system to be primarily affected by oblique astigmatism due to the oblique incidence of the laser on the SLM. However, the amount of aberration was minimal and the improvement brought by correction was insignificant (Fig S3). Nonetheless, aside from the aberrations introduced by the optics, this functionality is useful for improving the uncaging efficiency when accessing dendrites in deep regions of the brain tissue (Choy *et al.*, 2017).

2.5.2 Application of the holographic module: investigation of synaptic integration in 3D

We have used the system to perform targeted 2P uncaging in spines of L2/3 pyramidal neurons while recording the somatic responses with a patch electrode. Simultaneous uncaging at 8-10 spines across an axial range of up to 16 μm within 0.5-1.5 ms evoked an AP. We have also shown simultaneous holographic photostimulation and Ca^{2+} imaging in a single plane to study Ca^{2+} dynamics and monitor a physiological evoked Ca^{2+} response at the spine. Highly resolved 2P uncaging and Ca^{2+} imaging at the level of single spines complements the work by Anselmi *et al.* (2011), where they introduced remote focusing to perform low resolution 1P uncaging and Ca^{2+} imaging over a long dendrite that tilts with respect to the optical axis.

The supra-linearity of integration we observed (Fig 8f) in proximal synapses is dependent on the synchrony of inputs (Branco and Hausser, 2011). Even in a single plane, the commercial galvanometer-based 2P microscope cannot achieve as many uncaging sites within this time window; despite its fast positioning time ($\sim$ 100 μs), the rate-limiting factor is the dwell time required to release a sufficient amount of glutamate to evoke an EPSP with good signal-to-noise ratio ($\sim$ 200-500 μs) (Losavio *et al.*, 2009; Losonczy *et al.*, 2008).

The capability of our system to position stimulation sites in 3D offers flexibility in targeting a sufficient number of spines to evoke an AP or otherwise trigger local regenerative events within dendrites. That is, the required number of spines do not all have to be localized within a single focal plane, an otherwise typical experimental limitation with 2D scanners. While triggering of action potentials has been demonstrated before in 2D for cortical and hippocampal pyramidal neuron dendrites with a high spine density (Branco *et al.*, 2010; Makara and Magee, 2013), an accessible volume for simultaneous stimulation is particularly desirable for low-density synapse distributions. For example, some spinous cell types feature a much lower spine density than the $\sim$ 20 spines/10 μm reported for hippocampal or cortical pyramidal cells (Harris and Stevens, 1989; Ballesteros-Yáñez *et al.*, 2006). Cortical spinous inhibitory neurons can have as few as 0.3 spines per 10 μm depending on the neuron subtype (Kawaguchi *et al.*, 2005). Likewise, OB GCs feature $\sim$ 1-2 spines per 10 μm (Saghatelyan *et al.*, 2005). Moreover, such flexibility can be useful in studies of integration within highly ramified branched structures such as apical tufts of PCs or

of OB MC/TCs. The possibility of moving the VOI without moving the sample could be advantageous for studies of integration across various branch compartments of a cell such as basal versus apical dendrites, in particular for situations where more than one pipette/electrode is positioned in the brain slice such that movement of the sample is limited.

Because the uncaging laser path is integrated into the scanning path, during simultaneous holographic photostimulation and Ca^{2+} imaging, the scanning mirrors are fixed in position for the duration of the uncaging stimulus. The uncaging pulse is 0.5 - 1.5 ms. This pulse disrupts the Ca^{2+} imaging which is started 700 ms before uncaging but it does not significantly affect the temporal resolution of the imaging as the 10 % - 90 % rise time of the Ca^{2+} indicator we used (OGB-1) is ~100 ms (Tada *et al.*, 2014). Note that even with 10 stimulation sites, the pulse duration remains the same. In contrast, sequential uncaging with the galvanometer mirrors would require up to 5 ms. Thus, there is a shorter disruption to the Ca^{2+} imaging signal with simultaneous multi-site uncaging.

2.5.3 Comparison with other systems for holographic photostimulation

Holographic photostimulation has been demonstrated previously with 1P uncaging (Lutz *et al.*, 2008; Yang *et al.*, 2014a; Yang *et al.*, 2011; Anselmi *et al.*, 2011; Yang *et al.*, 2014b; Tanese *et al.*, 2017). The energy of light used for 1P uncaging (e.g. ultra-violet light) does not require tight focusing and therefore does not suffer in terms of trade-off between FOV and resolution. A 1P uncaging system with extended FOV, however, will have lesser resolution and may not be able to target individual spines. Moreover, 1P uncaging lacks localized photolysis along the axial direction and could uncage unnecessarily at off-target planes. This can be a problem when dendrites are overlapping along the optical axis. Intrinsic localized uncaging in 3D provided by non-linear 2P excitation is preferred in such situations.

To precisely position excitation spots in 3D, multi-site 2P uncaging must also be used in conjunction with high-resolution imaging systems such as confocal or 2P microscopes. Nikolenko *et al.* (2008) demonstrated 3D localization and depth focusing of the photostimulation spot using 2P excitation but showed multi-site stimulation only within a single focal plane. We extended this capability to multiple planes (Go *et al.*, 2013; Go *et al.*, 2012) by applying a different lens function to the phase hologram of each spot thereby independently focusing each photostimulation spot

to a different depth. Both these previous demonstrations of 2P holographic photostimulation employed fully customized microscope systems, while the system described here is modular and can be added into any 2P commercial system with an accessible uncaging light path.

Dal Maschio *et al.* (2010) developed a holographic module and integrated it with a commercial scanhead to steer holographically structured illumination patterns for 2P uncaging in 2D. These patterns were used to follow specific contours of cultured neurons similar to the work by Lutz *et al.* (2008). However, a holographically projected shape that covers a larger illumination area results in a poor localization of 2P excitation along the optical axis and is therefore not applicable for stimulating spines along complex dendritic arborizations that overlap along the beam path. While this problem can be solved via temporal focusing (Oron *et al.*, 2005; Hernandez *et al.*, 2016; Tanese *et al.*, 2017), the use of diffraction-limited 2P stimulation remains a preferred method for multi-site photolysis where each focus stimulates a synaptic input in 3D in a highly localized fashion.

Yang *et al.* (2015) also integrated the hologram onto the laser beam of a custom-built 2P scanning microscope for Ca^{2+} imaging. They used the galvanometer scanning mirrors to sequentially reposition the holographic FOV (140 × 140 μm^2) 9 times in a tiled manner to achieve an extended FOV of 380 × 380 μm^2. This is possible for functional Ca^{2+} imaging since the temporal dynamics of Ca^{2+} response is in the order of hundreds of milliseconds. However, when used for uncaging over an extended FOV, time-division multiplexing does not achieve simultaneous excitation. In the future, such a large-scale simultaneous excitation may be possible in conjunction with fast SLMs such as those with binary phase shifts using ferroelectric liquid crystals, which can be operated at ~ kHz refresh rates and which could be used to achieve simultaneous multi-site photostimulation in an extended FOV in a biologically relevant time window (a few milliseconds). Beyond multi-foci uncaging in 3D, our holographic module could also be used for 2P optogenetic activation of neuronal populations with a standard commercial 2P laser scanning microscope (Yang *et al.*, 2018). For this application structured illumination (rather than multi-foci patterns) could be used to stimulate and recruit a sufficient number of light-activatable ion channels distributed within the somatic membrane to induce a detectable neuronal response (Rickgauer and Tank, 2009).

2.5.4 Conclusion

We incorporated a holographic projector into a commercial 2P scanning microscope to extend the spatial range of multi-site 2P uncaging. With proper integration of the microscope's built-in 3D rendering, zoom and arbitrary ROI function, simultaneous 2P uncaging at multiple sites can be performed at highly resolved sections targeting spines of dendritic trees branching in 3D, with a number of inputs sufficient for eliciting action potentials from rest. Moreover, the combination allowed the positioning of the holographic VOI arbitrarily across the entire imaging FOV without repositioning the sample. Attaching a holographic projector to a commercial 2P microscope offers 3D multi-site photostimulation with the advantages of versatility and straightforward implementation over custom 2P holographic systems and will be an important tool in the study of synaptic integration.

2.6 Supporting information

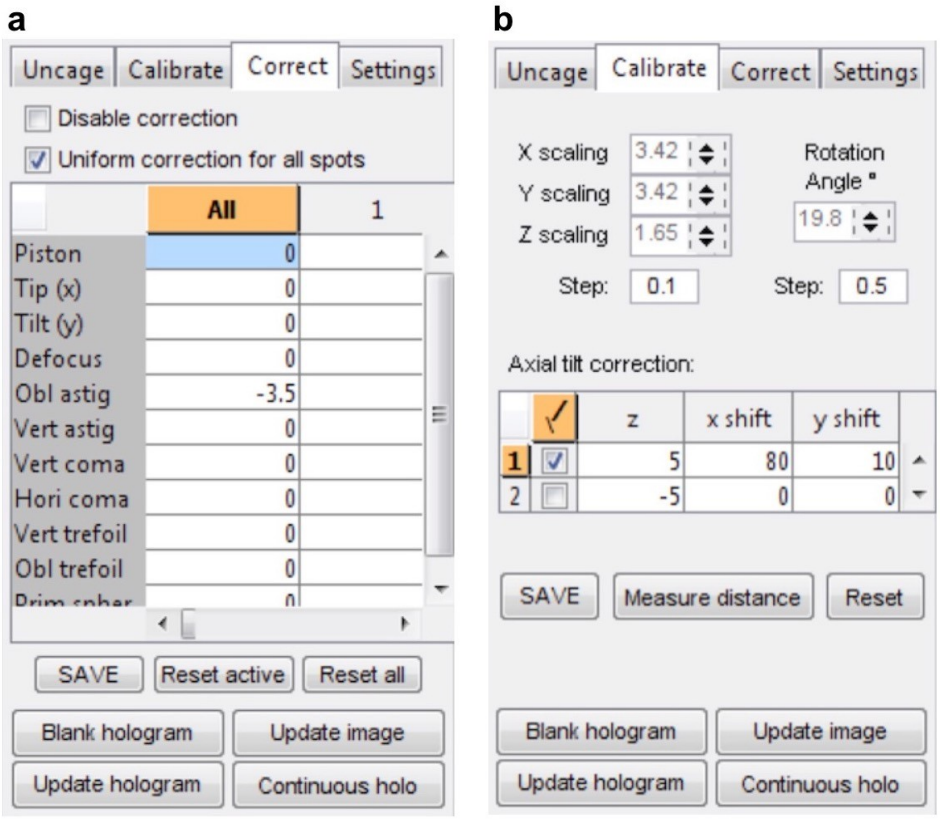

Fig S1. ***Calibration and aberration correction of excitation spots.***
Custom SLM software GUI for ***a****: aberration correction and* ***b****: calibration of uncaging spots.*

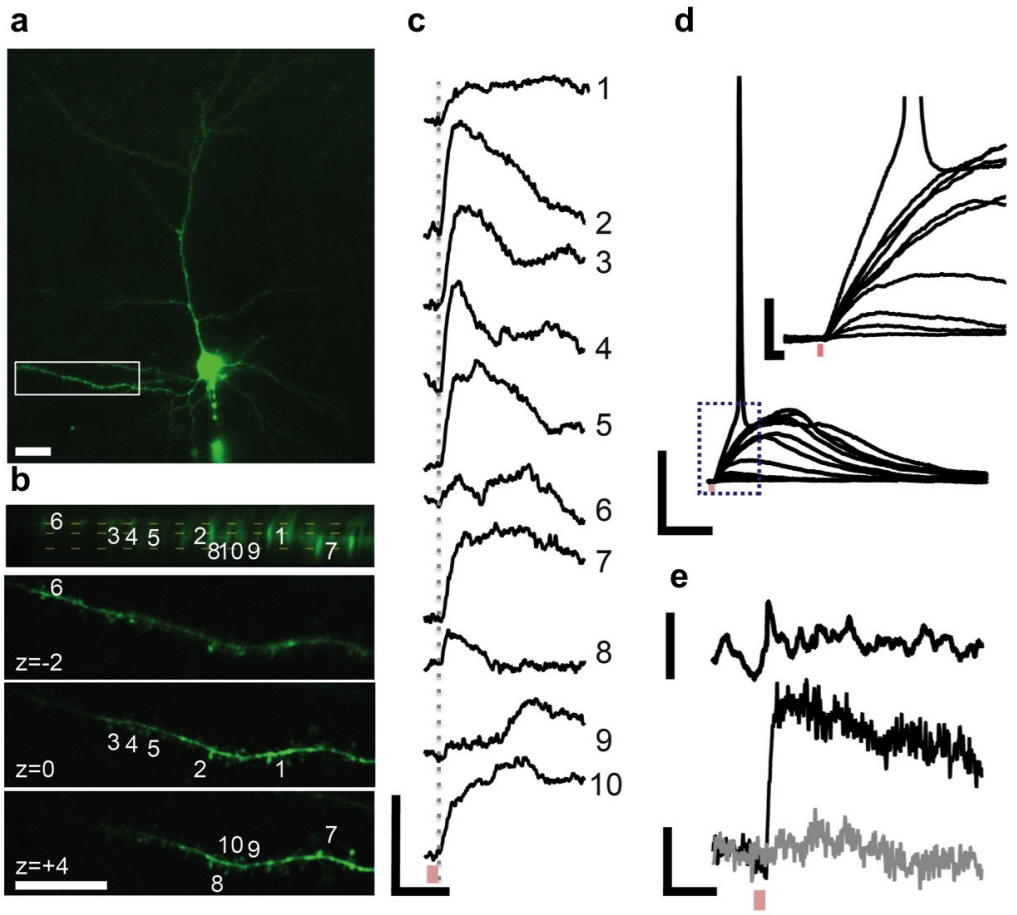

Fig S2. ***Synaptic integration experiment with a 20× objective lens.***
a*: Two-photon image of a layer 2/3 pyramidal cell labeled with OGB-1. Scale bar 20 µm.* ***b****: The VOI displayed as an xz-image with 3 representative image planes (i: z = –2 µm; ii: z = 0; and iii: z = + 4 µm. Scale bar: 20 µm.* ***c****: Somatic EPSPs of individual uncaging events (red bar indicates time point of 2P glutamate uncaging). Scale bars: 1 mV, 40 ms.* ***d****: Uncaging responses with increasing number of simultaneous uncaging sites. Scale bars: 20mV, 50 ms. (Inset) Magnified EPSP rise times for increasing number of uncaging sites. Scale bars: 5 mV, 5 ms.* ***e****: Representative individual uncaging-evoked EPSP at spine 4 and corresponding Ca^{2+} transient (ΔF/F) in spine (black) and nearby dendrite (gray). Scale bars: 2 mV, 20%, 500 ms.*

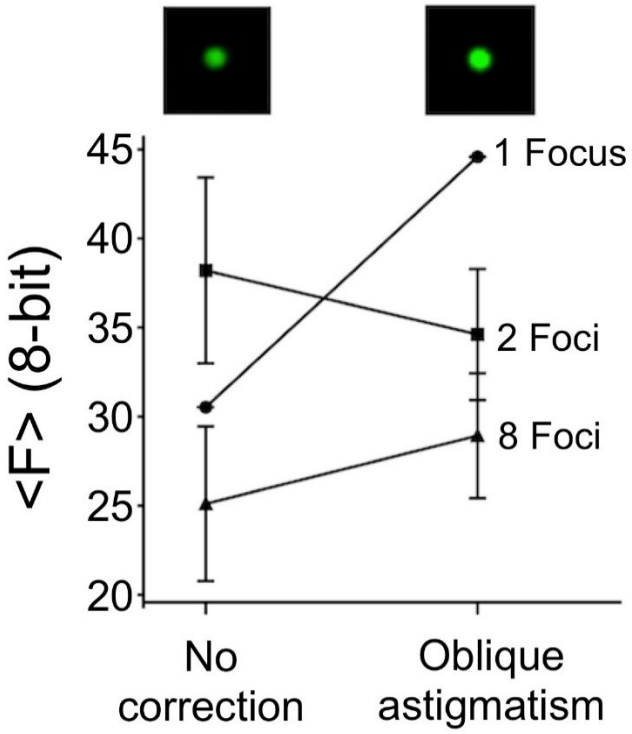

Fig S3. ***Aberration correction.***
Effect of correction for oblique astigmatism on the 2P fluorescence intensity (8-bit gray level) of a fluorescent bead for different numbers of foci. (Inset) 2P images of a fluorescent bead with no correction and with correction for oblique astigmatism.

Video S1. ***3D rendering of VOI.***
Video showing rotation of the VOI used in the experiment in Fig 8 along the y-axis. Shown is the 3D extension of the segment of dendrite targeted for multi-site uncaging.
https://doi.org/10.1371/journal.pone.0210564.s004

Video S2. ***3D rendering showing various planes of VOI.***
Video showing different axial planes of the segment of dendrite targeted for multi-site uncaging in the experiment in Fig 8.
https://doi.org/10.1371/journal.pone.0210564.s005

3 Dendritic integration in olfactory bulb granule cells: thresholds for lateral inhibition and role of active conductances upon simultaneous activation

3.1 Abstract

The inhibitory axonless OB GCs form reciprocal dendrodendritic synapses with MCs and TCs via large spines, mediating recurrent and lateral inhibition. Rat GC dendrites are excitable by local Na^+ spine spikes and global Ca^{2+}- and Na^+-spikes. To investigate the transition from local to global signaling without Na^+ channel inactivation we performed simultaneous holographic 2P uncaging in acute brain slices, along with whole-cell recording and dendritic Ca^{2+} imaging. Less than 10 coactive reciprocal spines were sufficient to generate diverse regional and global signals that also included local dendritic Ca^{2+}- and Na^+-spikes (D-spikes). Individual spines could sense the respective signal transitions as increments in Ca^{2+} entry. Dendritic integration was mostly linear until a few spines below global Na^+-spike threshold, where often D-spikes set in. NMDARs strongly contributed to active integration, whereas morphological parameters barely mattered. In summary, thresholds for GC-mediated bulbar lateral inhibition are low.

3.2 Introduction

The classical role of dendrites is to receive synaptic or sensory inputs and to conduct the ensuing electrical signals towards the site of AP initiation at the axon hillock. While this conduction is passive for smaller membrane depolarizations, recent decades have revealed the presence of active dendritic conductances, most importantly Na_vs, Ca_vs and NMDARs, that can amplify locally suprathreshold electrical signals and thus generate dendritic spikes in many neuron types; dendritic Na_vs also facilitate backpropagation of axonal APs into the dendritic tree (Stuart and Spruston, 2015).

The dendritic integration of multiple excitatory inputs - as detected at the soma - is usually linear for small numbers of coactive synapses but then frequently transitions into regimes of sublinear or supralinear summation with respect to the arithmetic sum of the individual synaptic potentials. The mode of integration depends on dendritic input impedance, the density of active

conductances and the distribution of synaptic inputs, both in the spatial and temporal domain (Tran-Van-Minh *et al.*, 2015).

For example, supralinear integration occurs in cortical and hippocampal PC dendrites, carried by Ca^{2+}-spikes, so-called NMDA-spikes and dendritic Na^{+}-spikes (D-spikes) which show as spikelets at the soma (Losonczy and Magee, 2006; Major *et al.*, 2013; Larkum *et al.*, 2007; Remy *et al.*, 2009; Makara and Magee, 2013; Kim *et al.*, 2012b). Such active integration mechanisms have been shown to e.g. boost axonal AP initiation, enable local coincidence detection and therewith contribute to the induction of synaptic plasticity.

Conversely, sublinear integration is performed by e.g. GABAergic cerebellar stellate cell dendrites, that is mainly determined by passive cable properties and reductions in driving force for large dendritic depolarizations (Abrahamsson *et al.*, 2012). In contrast to supralinear integration, this type of integration will favor sparse and/or distributed inputs.

Aside from such computations that ultimately convert analogue signals into binary code at the axon initial segment, another functional outcome of dendritic integration is the (possibly graded) release of transmitter from the dendrites themselves. Dendritic transmitter release occurs in many brain regions and is particularly well known from the retina and the OB (Ludwig and Pittman, 2003). In the bulb, axonless inhibitory GCs release GABA exclusively from their apical dendrite. These release sites are located within spines that contain reciprocal dendrodendritic synapses with the excitatory MCs and TCs. Unlike principal neurons in the cortex and hippocampus, MC/TCs that belong to different glomerular columns do not communicate directly via axon collaterals or otherwise. Rather, their only interaction happens via lateral inhibition, mediated by GCs and other local interneurons. Although MC/TC-GC synapses are the most numerous in the bulb (Shepherd, 1972; Egger and Urban, 2006), so far it is unknown how many coinciding MC/TC inputs are required to generate global GC activity and with it Ca^{2+} entry also in non-activated spines, possibly invoking lateral inhibition. The properties of dendritic integration in GCs thus critically determine the onset and degree of lateral inhibition.

What is known so far about GC dendritic processing? A single MC/TC input triggers a local Na^{+}-AP that is restricted to the spine head because of a high spine neck resistance (Bywalez *et al.*, 2015). This spine spike can cause reciprocal release of GABA via gating of HVACCs (Lage-

Rupprecht *et al.*, 2019). Activation of larger numbers of spines results in global LTS which are mediated by T-type Ca_Vs (Egger *et al.*, 2005; Pressler and Strowbridge, 2019; Pinato and Midtgaard, 2005). Synaptically evoked Na^+ spikelets have been reported from mouse, turtle and frog GCs, causing regional Ca^{2+} entry (Pinato and Midtgaard, 2005; Zelles *et al.*, 2006; Burton and Urban, 2015), while somatic full-blown synaptic Na^+ APs can be elicited by stimulation of a single glomerulus (Schoppa *et al.*, 1998) and result in substantial Ca^{2+} entry throughout the GC dendrite that was larger than LTS-mediated Ca^{2+} entry in the same location (Egger, 2008; Stroh *et al.*, 2012).

If we assume that LTS-mediated Ca^{2+} entry is sufficient to trigger lateral GABA release from at least some reciprocal spines, then the threshold for the generation of dendritic LTS is equivalent to the onset of lateral inhibition, whereas Na^+-spikes are likely to cause lateral inhibition with greater efficiency than LTS. Pressler and Strowbridge (2017) have predicted that at least 20 coactive MC/TC inputs (within a time window of 1 ms) are required to achieve Na^+ AP generation in 50% of trials. Because of the rather hyperpolarized GC resting membrane potential of – 80 mV and median unitary EPSP amplitudes ≤ 2 mV (Egger *et al.*, 2005; Bywalez *et al.*, 2015), we expected a similar outcome.

Another question is whether the local spine spikes contribute to dendritic integration in GCs. Is it conceivable that activation of neighboring spines causes an invasion of the dendritic segment associated with this spine cluster by the spine spike(s)? Could this scenario result in a D-spike? Conventional sequential uncaging (that involves moving the 2D xy-scanner from one uncaging spot to the next) would preclude any observations of such effects because of the inactivation of Na_Vs during the stimulation sequence. Therefore, we implemented a holographic stimulation system to simultaneously stimulate spines in 3D (Go *et al.*, 2019). This paradigm is also coherent with physiological activation, since the firing of MC/TCs within a glomerular ensemble is precisely locked to the sniff phase and thus can be synchronized within 1 ms (Shusterman *et al.*, 2011). Holographic stimulation also enabled us to target sufficient numbers of inputs, a problem in 2D because of the low GC spine density (1-2 spines per 10 µm, Saghatelyan *et al.*, 2005).

3.3 Material and methods

3.3.1 Animal handling, slice preparation and electrophysiology

All experimental procedures were done in accordance with the rules laid down by the EC Council Directive (86/89/ECC) and German animal welfare legislation. Rats (postnatal day 11-21, Wistar of either sex) were deeply anaesthetized with isoflurane and decapitated. Horizontal olfactory bulb brain slices (thickness 300 µm) were prepared and incubated at 33°C for 30 min in ACSF bubbled with carbogen and containing (in mM): 125 NaCl, 26 $NaHCO_3$, 1.25 NaH_2PO_4, 20 glucose, 2.5 KCl, 1 $MgCl_2$, and 2 $CaCl_2$. Recordings were performed at room temperature (22 °C). Patch pipettes (pipette resistance 5-7MΩ) were filled with an intracellular solution containing (in mM): 130 K-methylsulfate, 10 HEPES, 4 $MgCl_2$, 2.5 Na_2ATP, 0.4 NaGTP, 10 Na-phosphocreatine, 2 ascorbate, 0.1 OGB-1 (Ca^{2+} indicator, Invitrogen), 0.04-0.06 Alexa Fluor 594 (Life Technologies), at pH 7.3. The following pharmacological agents were bath applied in some experiments: TTX (0.5 – 1 µM, Alomone), D-APV (25 µM, Tocris), mibefradil (10 µM, Tocris), and cadmium chloride (Cd^{2+}, 100 µM, Sigma). Drugs were washed in for at least 10 min before starting measurements. Electrophysiological recordings were made with an EPC-10 amplifier and Patchmaster v2.60 software (both HEKA Elektronik). GCs were patched in whole-cell current clamp mode and held near their resting potential of close to –75 mV (Egger *et al.*, 2003). If GCs required >25 pA of holding current, they were rejected. In order to provide optimal optical access to the GC apical dendritic tree, patched GCs were located close to the MCL.

3.3.2 Combined two-photon imaging and multi-site uncaging in 3D

Imaging and uncaging were performed on a Femto-2D-uncage microscope (Femtonics). The microscope was equipped with a 60× water-immersion objective used for patching (NA 1.0 W, NIR Apo, Nikon) and a 20× water-immersion objective used for 2P imaging and uncaging (NA 1.0, WPlan-Apo, Zeiss). Green fluorescence was collected in epifluorescence mode. The microscope was controlled by MES v4.5.613 software (Femtonics). Two tunable, verdi-pumped Ti:Sa lasers (Chameleon Ultra I and II, respectively, Coherent) were used in parallel, set to 835 nm for excitation of OGB-1 and to 750 nm for uncaging of DNI-caged glutamate (DNI, Femtonics; Chiovini *et al.*, 2014). DNI was used in 0.6 mM concentration in a closed perfusion circuit with a total

volume of 12 ml and was washed in for at least 10 min before starting measurements. To visualize the spines and for Ca^{2+} imaging we waited at least 20 min for the dyes to diffuse into the dendrite before starting measurements.

Imaging and uncaging beam were decoupled before the entrance of the galvanometer-based 2D scanning microscope using a polarizing beam splitter to relay the uncaging beam to a spatial light modulator (SLM X10468-03, Hamamatsu). Using our custom-written Matlab based SLM software, we next positioned multiple uncaging spots/foci in 3D at a distance of 0.5 μm from the spine heads. Our system allowed for a maximum number of 12 spots in a volume of 70x70x70 μm^3, usually spines no deeper than ~ 30 µm were imaged because otherwise uncaging laser power was too much attenuated. The positioning was checked before each measurement and, if necessary, readjusted to account for drift. The holographic projector module is described in detail in Go *et al.* (2019). The uncaging pulse duration was 1–2 ms and the laser pulse power was adjusted individually for each experiment to elicit physiological responses, depending on the depth of the spines (Bywalez *et al.*, 2015). For simultaneous multi-site photostimulation, the total uncaging power and the number of foci/spots were kept constant. “Superfluous” foci, i.e. foci that were not needed as stimulation spots at a given time of an experiment, were excluded by positioning them just outside the holographic FOV, such that they would fall off the optics and not be projected onto the sample (Go *et al.*, 2019). Imaging of uncaging-evoked Ca^{2+} signals in selected spines and dendritic positions within one 2D plane (see below) was carried out as described earlier (Bywalez *et al.*, 2015). During simultaneous Ca^{2+} imaging and photostimulation, imaging was started 700 ms before the uncaging stimulus. During uncaging the scanning mirrors were fixed.

In each experiment, single spines were consecutively activated and somatic uncaging EPSPs (uEPSPs) were recorded for each spine separately. Next, successively increasing # of these spines were simultaneously activated and somatic compound uEPSPs (cuEPSPs) were recorded until the GC fired an AP or, in the experiments with focus on subthreshold integration, until a maximum # of 10 activated spines was reached. A subset of spines and dendritic locations located within the same focal plane were chosen for 2P line-scanning to gather Ca^{2+} imaging data. At least one spine, termed S1 in the following, was always located in this imaging plane to gather complete data

from activation of a single spine to activation of n spines. Due to the spine density being higher in distal regions and Ca^{2+} imaging being restricted to one focal plane, most dendritic measurements in a distance from the center of the stimulated spine set (Fig 11b) were proximal to the stimulation site. The sequence of the successively more activated spines with respect to their position on the dendritic tree was randomly chosen. However, the low spine density (see *3.2*) and the restriction to a volume of 70x70x70 μm^3 mostly determined the choice of activated spines. Both single spine stimulations and the different combinations of multi-site uncaging were, if possible, performed at least twice and recordings were averaged for analysis.

As such experiments were performed with up to 40 different stimulation conditions, we decided to increase the spine # by increments of two for some experiments (in particular for pharmacology) in order to keep the experiment duration short and thus to ensure a good recording quality.

3.3.3 Data analysis

Changes in Ca^{2+} indicator fluorescence were measured relative to the resting fluorescence F_0 in terms of ΔF/F as described previously (Egger *et al.*, 2005). Electrophysiological and Ca^{2+} imaging data were analyzed using custom macros written in IGOR Pro (Wavemetrics). Traces contaminated by spontaneous activity were discarded. As described above, multiple (2 or more) recordings of the same stimulation type were averaged and smoothed (box smoothing) for analysis. uEPSP and $(\Delta F/F)_{TPU}$ rise times were analyzed in terms of the interval between 20% and 80% of total uEPSP/$(\Delta F/F)_{TPU}$ amplitude; uEPSPs and $(\Delta F/F)_{TPU}$ half times of decay (τ_1/2) were analyzed in terms of the interval between the peak and 50% of the total EPSP or $(\Delta F/F)_{TPU}$ amplitude. The uEPSP maximum rate of rise was determined by the peak of the first derivative of the uEPSP rising phase. The AP threshold was detected via the zero point of the 2nd derivative of the AP rising phase.

Integration was quantified by plotting the arithmetic sum of the respective single spine uEPSP amplitudes versus the actually measured multi-spine cuEPSP amplitude for increasing numbers of coactivated spines, yielding a subthreshold input-output (sI/O) relationship (Tran-Van-Minh *et al.*, 2015). If the cuEPSP amplitude consistently exceeded the arithmetic sum of the single spine

uEPSPs beyond a certain stimulation strength by at least a factor of 1.2, we classified these sI/O patterns as supralinear. If the factor fell consistently below 0.8, we classified these sI/O patterns as sublinear, and the patterns falling between these categories were considered to be linear. The factors were set at 0.8 and 1.2 to exceed potential undersampling errors in cuEPSP amplitudes (see below) and were empirically confirmed by concurrent characteristic changes in cuEPSP kinetics (see Fig 12e).

As criterion for the presence of a Ca^{2+}-spike, dendritic Ca^{2+} transient amplitudes $(\Delta F/F)_{TPU}$ had to exceed a value well above noise level (≥ 8% ΔF/F or factor 1.5 above noise level of 5% ΔF/F) and be detectable at every dendritic line scan located within the section of the dendrite carrying stimulated spines (Fig 11, Fig 13e; Egger *et al.*, 2005).

3.3.4 Data sampling, normalization and alignment

Since for any particular number of coactivated spines we could not perform more than 2 -3 stimulations in the interest of finishing experiments within the average lifetime of GC recordings, the individual cuEPSP measurements might differ from the mean for that particular spine number due to undersampling. For single uEPSPs, a previous data set allows to estimate the variance at the average EPSP amplitude of 1.40 mV in the experiments in this study as 0.39 mV or ~ 30% (n = 18 spines, linear regression on data with at least 6 uEPSP measurements per spine on the same system from Bywalez *et al.*, 2015). On the other hand, stimulations of larger numbers of spines n can be expected to reduce this sampling problem by a factor of √n, since the variabilities of the single spine responses should cancel out, similar to the effect of averaging across repeated stimulations of the same spine. Therefore, we expect a fairly consistent reporting of cuEPSP amplitudes above 5 costimulated spines, even with a low number of stimulations. Still, we set the criterion for supra-/sublinearity in V_m rather high (± 20 %), to prevent any erroneous classifications, also since the undersampling errors further propagate to the calculation of O/I ratios.

Similarly, the variance in single spine $(\Delta F/F)_{TPU}$ is on the order of 6% ΔF/F or ~ 20% (again derived from Bywalez *et al.*, 2015). To compare S1 spine ΔF/F amplitude data across experiments relative to solely local activation of S1, we intended to normalize these to the spine ΔF/F amplitude for local, unitary activation. Because of the undersampling problem, we tested for up to which spine

number there was no significant increase in ΔF/F, which was 4 spines (Friedman repeated measures ANOVA on ranks: $X^2_F(3)=4.802$, p=0.187). Therefore, we averaged S1 (ΔF/F) for (co)stimulations of 1, 2, 3, 4 spines and used the mean as basal unitary ΔF/F for normalization. Thus, undersampling could be compensated for by this means.

Since dendritic $(\Delta F/F)_{TPU}$ was usually detectable only in stimulations above 4 spines in most cases, $(\Delta F/F)_{TPU}$ in the dendrite was normalized to the mean of all stimulations below global Na^+ AP threshold, or the average size of the dendritic Ca^{2+}-spike mediated Ca^{2+}-signal.

Since each GC required its individual spine number to reach the threshold for the non-local events Ca^{2+}-spike, D-spike and global Na^+-spike (for the respective pattern of stimulation), we aligned the data in relation to the onset of the non-local event (e.g. Fig 11d, e relative to Ca^{2+}-spike). Such realignments allow to reveal effects across the sampled cells that otherwise would be smeared out because of cell-specific thresholds, such as recruitment of active conductances near thresholds (Losonczy and Magee, 2006).

3.3.5 Morphological analysis

GC apical dendrites were reconstructed from 2P fluorescence z-stacks gathered at the end of each experiment, using Neurolucida (MBF Bioscience). Distances were measured along the dendrite. Mean distances of a spine set were analyzed in terms of the average distance of all stimulated spines from e.g. the MCL. The distribution of a stimulated spine set across the dendrite was analyzed in terms of the mean distance of each spine from all other stimulated spines along the dendrite. Spine neck lengths were estimated as described before (Bywalez *et al.*, 2015).

3.3.6 Statistics

Statistical tests were performed in Sigmaplot 13.0 (Systat Software, Inc) or on vassarstats.net. To assess statistical significance levels across spine numbers or threshold V_m values for Ca^{2+}-spike versus global Na^+-spike (Fig 11c), data sets were compared using paired t-tests for dependent data sets. Not normally distributed data sets (Shapiro-Wilk Normality Test) were compared using Wilcoxon signed rank tests. To assess statistically significant differences from linear summation in sI/O relation data sets, the distribution of ratios of the measured uEPSP amplitudes/arithmetic

sums (O/I ratio) was tested against a hypothesized population mean/median of 1.0 (corresponding to linear summation), using one-sample t-tests or one-sample signed rank tests for not normally distributed data. To assess variation in repeated measure data sets (Fig 12c) repeated measures ANOVA together with all pairwise multiple comparison procedure (Holm-Sidak-method) was performed. For pharmacology experiments (e.g. Fig 14) repeated measures two-way ANOVA together with all pairwise multiple comparison procedure (Holm-Sidak-method) was performed. For statistical analysis of dendritic $(\Delta F/F)_{TPU}$ before and after pharmacological treatment just stimulations of ≥ 4 spines were taken into account, since for lower numbers of spines usually no signal was detectable under control conditions.

3.3.7 Tests of parameter changes at threshold

Due to the increase of spine numbers by increments of 2 in some experiments, averaged data points for a given spine number do not contain the same n of individual measurements across different spine numbers. Even more so when the data were aligned relative to individual spike thresholds (e.g. alignment relative to Ca^{2+}-spike threshold in Fig 11d, e), since not all experiments contained data points for the more remote spine numbers +2 or -3.

In addition, in experiments with data gaps just before a global spike threshold at spine number x, it is not possible to know whether the spike threshold could have already been reached at x-1 spines (e.g. alignment relative to Ca^{2+}-spike in Fig 11 d, e). We accounted for this uncertainty by averaging the data in the continuous experiments for -2 and -1 and used these averaged data for paired comparison of parameters below and at threshold (non-parametric Wilcoxon test). Fig S4 shows the individual data points for all these comparisons normalized to -2/-1. If there was a significant linear increase or decrease with spine number in the parameter in the subthreshold regime (grey dashed lines in Fig 11d, e; 12d, e; 13c-f), the expected increment based on this change was subtracted from the parameter values at threshold before statistical testing for a difference.

To assess statistical significance for linear increase and decrease (Table S1) we performed a linear regression analysis. Given r^2 values are adjusted r^2 values.

3.4 Results

To study synaptic integration within GC apical dendrites we mimicked simultaneous MC/TC inputs to a defined number and arrangement of GC spines in the EPL by 2P uncaging of DNI-caged glutamate (Palfi *et al.*, 2018; Bywalez *et al.*, 2015) at multiple sites in 3D using a holographic projector (Go *et al.*, 2019). GCs in juvenile rat acute brain slices were patch-clamped and filled with Ca^{2+}-sensitive dye OGB-1 (100 µM) to record somatic V_m and Ca^{2+} influx into a stimulated spine and several dendritic locations by 2P Ca^{2+} imaging within a 2D plane (see *3.3*).

3.4.1 Subthreshold dendritic integration

To characterize subthreshold dendritic integration in terms of somatic V_m we first consecutively stimulated single GC spines to obtain single synapse uEPSPs, followed by simultaneous activation of the same spines, resulting in compound cuEPSP. The number of coactivated spines was increased until either AP threshold or the available maximum were reached (10-12 spines, see *3.3.2*). Under the given experimental conditions, we succeeded to elicit an AP in 35 out of 111 GCs, 8 of which fired 2 or more APs (e.g. Fig 10a), with an average latency of 41 ± 40 ms (average ± SD, also below). The average single spine uEPSP across all spiking GCs was 1.4 ± 0.8 mV. Integration was quantified by plotting the arithmetic sum of the respective single spine uEPSP amplitudes versus the actually measured multi-spine cuEPSP amplitude for increasing numbers of coactivated spines, yielding a sI/O relationship for each GC.

Fig 10a shows a representative GC where 9 coactivated spines generated an AP in 4 out of 7 trials. This stochastic behavior at AP threshold was also observed in all other spiking GCs in our sample. The sI/O plots of all spiking GCs (Fig 10b) indicate that:

(1) For low numbers of coactivated spines, the average sI/O relationship across GCs was linear.

(2) In most GCs the cuEPSP amplitude exceeded the arithmetic sum of the single spine uEPSPs beyond a certain stimulation strength by an O/I ratio of at least 1.2 (O/I: output/input; n = 19 of 29 GCs). We classified these sI/O patterns as supralinear (for further validation of the supralinearity criterion see below and *3.3.3*). In this subset of cells, supralinearity was attained at an average of 6.7 ± 2.6 stimulated spines and maintained beyond this threshold until AP generation (except for 1 cell where the last added uEPSP was very large).

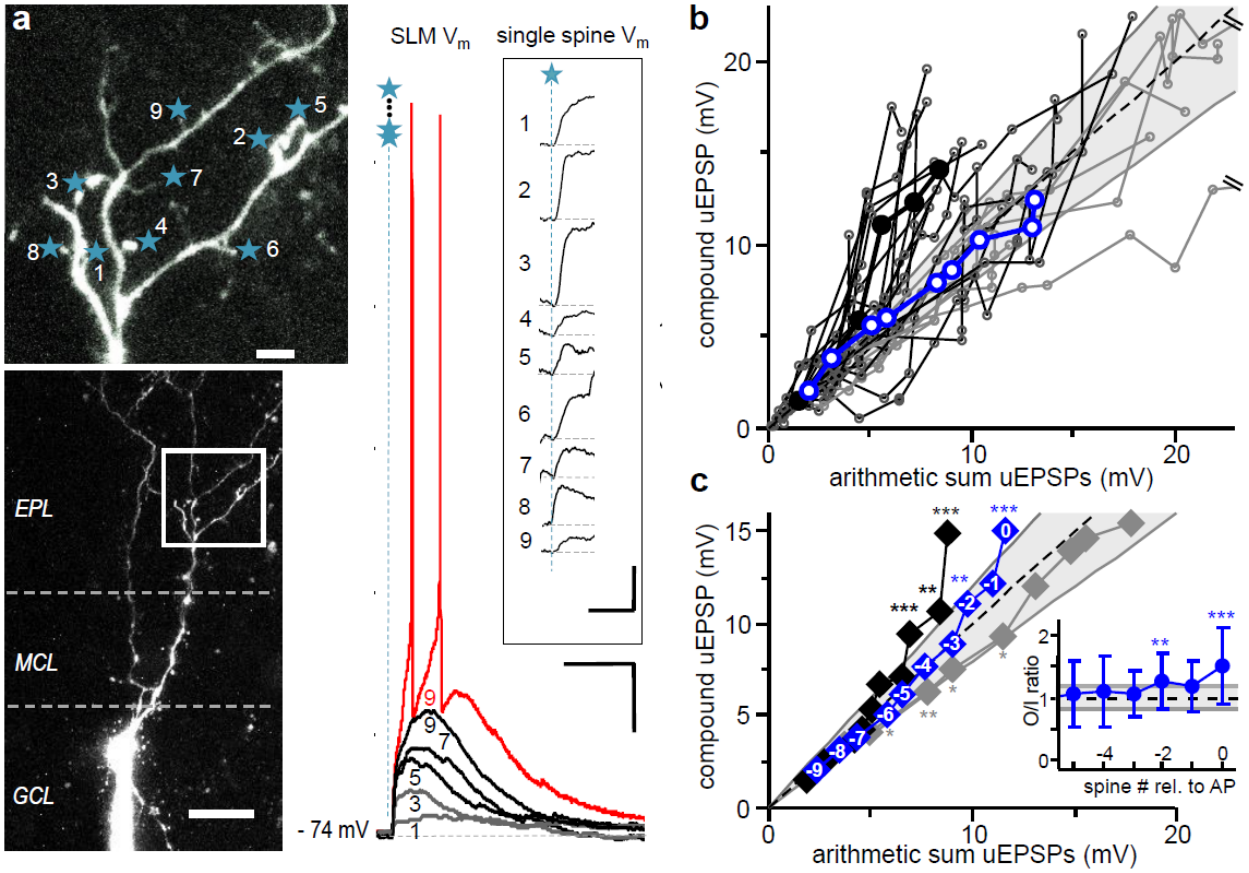

Fig 10. ***Subthreshold dendritic integration in GCs.***
a: *Left: 2P scan and z-projection of representative GC, inset shows enlarged part. Stars represent uncaging spots. Scale bars: 2 µm (inset), 20 µm. Right: Somatic compound uEPSPs and APs generated by simultaneous activation of 1,3,5,7,9 spines (● in b). Scale bars: 10 mV, 250 ms. Inset: Single spine uEPSPs recorded at the soma (see 3.3). Scale bars: 1 mV, 50 ms.* ***b:*** *Subthreshold input/output relationships (sI/O) of n=29 individual experiments in 28 GCs. Grey lines and ○: Sublinear to linear integration. Black lines and circles ○: Supralinear integration. Blue lines and* ***o****: Averaged sI/O of 1 to 9 coactivated spines across all GCs. Dashed line: linear y = x. Grey lines: Cut-off supra- and sublinear regime for classification of cells (y = 1.2x, y = 0.8x, see 3.3.3). 2 data points of 2 experiments exceed the scale.* ***c:*** *sI/O cumulative plot of experiments in b with data arranged from -9 to 0 spines relative to global AP threshold. Significance levels refer to O/I ratio distributions with means beyond the linear regime (0.8-1.2) tested against linearity (see inset, 3.3.3). ◆: average sI/O of all experiments, statistically significantly supralinear beyond -3 spines (see inset; average O/I ratios for supra- and linear/sublinear sI/Os not shown for clarity): -2 (p = 0.006) and 0 spines (p < 0.001, mean O/I ratio 1.53 ± 0.63). ◆: average of supralinear sI/Os only (n = 19), statistically significantly different from linear summation beyond -3 spines: -2 spines (p < 0.001), -1 (p = 0.007), 0 (p<0.001, mean O/I ratio 1.86 ± 0.52), n=19. ◆: average of sublinear to linear sI/Os only (n = 10), significantly below linear summation below -3 spines: -7 spines (p=0.027), -6 spines (p = 0.008), -5 spines (p=0.02), -4 spines (p=0.021, mean O/I ratio 0.79 ± 0.37), n = 10. In all figures, * p<0.05, ** p<0.01, *** p<0.001. GCL: granule cell layer, MCL: mitral cell layer, EPL: external plexiform layer.*

(3) Consistent sublinear integration (O/I ratio < 0.8) was observed in only 1 GC, while the remaining 9 GCs did not show any consistent deviations from linear behavior. In this subset of cells, the average single EPSP amplitude was larger than for supralinear cells (2.1 ± 0.6 mV vs 1.1 ± 0.6 mV, $p < 0.001$).

Since each GC required its individual spine number to reach the threshold for AP generation (for the respective pattern of stimulation), we next aligned the sI/O relations to the onset of the global AP before averaging (Fig 10c; see *3.3.4*). The ensuing average sI/O relationship was essentially linear until AP threshold ([0], corresponding to the number of spines that in a subset of stimulations triggered an AP) where it turned supralinear. The O/I ratios averaged across cells became significantly supralinear for the first time already at -2 spines below threshold (see Fig 10c inset; see *3.3.3*). If only the sI/Os classified as supralinear (see above) were averaged in this way, the average O/I ratio was highly significantly supralinear from 2 spines below AP threshold upwards. The average of the remaining linear/sublinear sI/Os was essentially linear, with a tendency towards sublinearity for lower numbers of coactive spines.

Thus, we find that dendritic V_m integration is by and large linear at the GC soma, with a supralinear increase in V_m close to global Na^+-spike threshold in the majority of cells.

3.4.2 Transition from local spine spikes to non-local signals (Ca^{2+}- and Na^+-spikes)

Since GCs are known to feature global LTS and LTS generation had been associated with an increase in EPSP amplitude and duration (Egger *et al.*, 2005), we investigated whether the onset of the supralinearity in somatic V_m observed in the majority of GC sI/Os coincided with Ca^{2+}-spike generation. We detected the transition from local spine spikes (which do not cause detectable dendritic calcium transients, Egger *et al.*, 2005; Bywalez *et al.*, 2015) to Ca^{2+}-spike generation via 2P Ca^{2+} imaging in dendritic shafts that were on average 4.4 ± 3.3 µm remote from the base of the closest stimulated spine, thus not directly adjacent to the spines (e.g. Fig 11a, 13a). Dendritic Ca^{2+} transients were considered to indicate the presence of a Ca^{2+}-spike if their amplitude was well above noise level ($\Delta F/F \geq 8\%$, see *3.3.3*). We also always imaged a spine that was photostimulated throughout all spine combinations (termed S1 in the following).

Fig 11a shows a representative experiment with somatic V_m and concurrent Ca^{2+} transients within the S1 spine and at several dendritic locations with increasing numbers of stimulated spines.

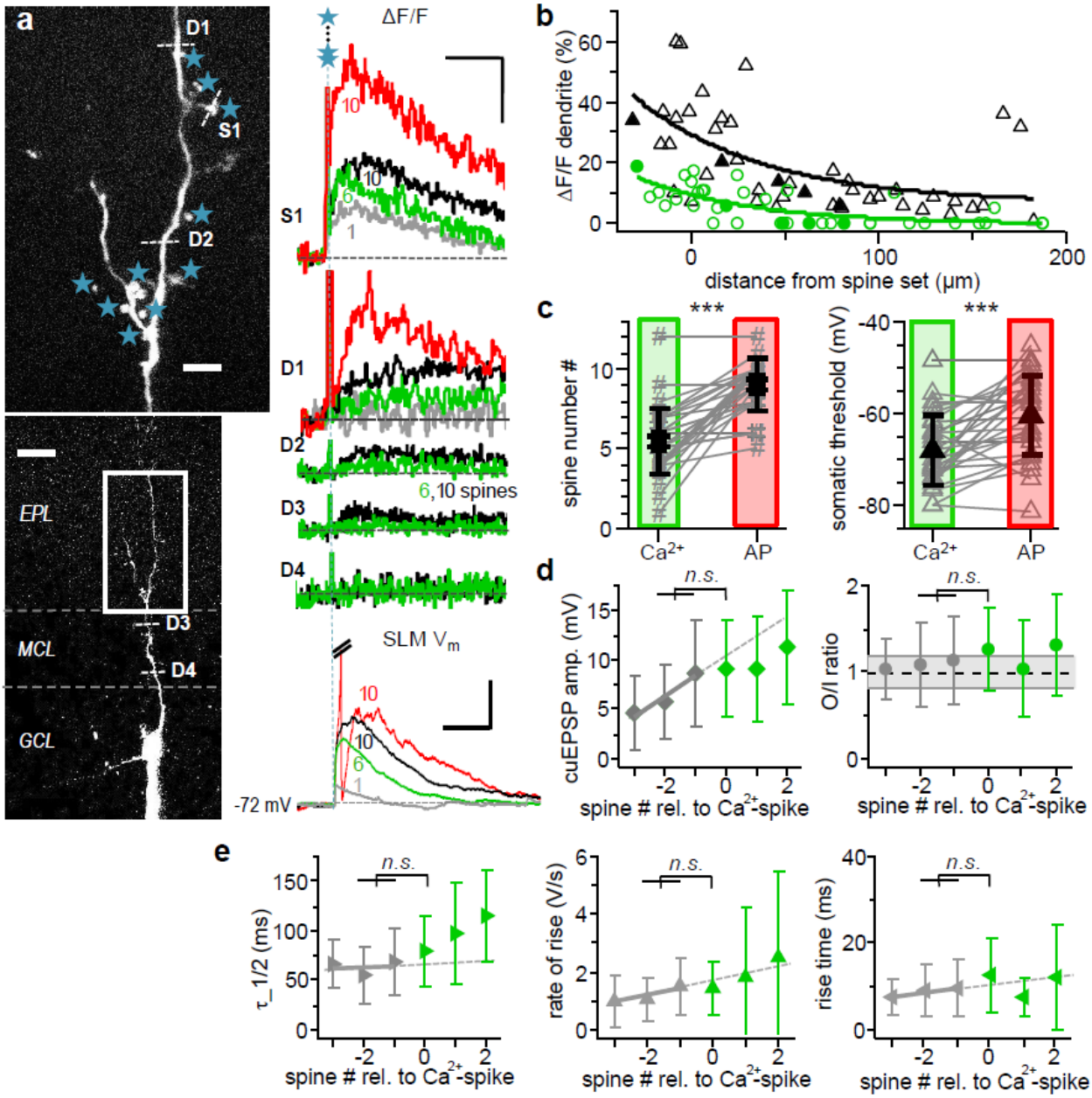

Fig 11. ***Dendritic Ca^{2+}-spikes: A non-local mode of dendritic activation. a:*** *Scan of representative GC (left, S1 and D indicate line scan sites, stars indicate uncaging spots, scale bars: 5 µm, 20 µm) with somatic V_m traces of single spine and multisite uncaging (bottom right, Na^+-AP truncated, scale bars: 10 mV, 100 ms) and averaged $(\Delta F/F)_{TPU}$ in the spine and dendrite (top right, scale bars: 50 %, 1 s) upon activation of 1,6,10 and 10 spines. Averaged $(\Delta F/F)_{TPU}$ in the dendrite measured at increasing distance from the activation site upon subthreshold activation of 6 and 10 spines (middle right). Grey: signals subthreshold for Ca^{2+}-spike, green: at Ca^{2+}-spike threshold, black: EPSPs and associated ΔF/F signals at AP threshold, red: suprathreshold for global Na^+-AP, S1: line scan spine S1, D1-4: line scans dendrite D1-4.* ***b:*** *Dendritic Ca^{2+} signals versus distance from the center of the stimulated spine set.○: responses at Ca^{2+}-spike threshold, Δ: responses for EPSPs at Na^+-spike threshold. Data from 12 GCs with ΔF/F data imaged at various distances from the set of stimulated spines. Filled symbols: Data from cell in* ***a****. Green and black lines: Exponential fits to respective data sets (at Ca^{2+}-spike threshold: decay constant ± SD: λ = 61 ± 30 µm, ΔF/F(200 µm) = 0 %, n = 38 data points; at Na^+-spike threshold: λ = 69 ± 47 µm, ΔF/F(200 µm) = 8 %, n = 44 data points).* ***c:***

Comparison of spine numbers (left) and somatic thresholds (right; both n = 27, p < 0.001, paired t-test) for Ca^{2+}-spikes and Na^{+}-spikes. ***d:*** *Left: Mean somatic cuEPSP amplitudes with spine numbers aligned relative to Ca^{2+}-spike threshold (0; n = 25). Difference between -2/-1 and 0 not significantly different from extrapolated linear fit (p = 0.29; Wilcoxon test, see 3.3.7, see Fig S4a for data points from individual experiments). Right: Mean O/I ratios aligned relative to Ca^{2+}-spike, not significantly different from subthreshold (p=0.78, n = 25). Grey symbols: subthreshold Ca^{2+}-spike, green symbols: suprathreshold Ca^{2+}-spike, dashed line: linear fit of subthreshold mean amplitudes, also for* ***e****.* ***e:*** *Kinetics of cuEPSPs (n = 25 GCs, see Fig S4a for data points from individual experiments): No significant increase above extrapolated linear fits at Ca^{2+}-spike threshold for half duration (left, p = 0.42, n = 22), rate of rise (middle, p = 0.052, n = 25) or rise time (right, p = 0.49, n= 25). GCL: granule cell layer, MCL: mitral cell layer, EPL: external plexiform layer.*

Across all GCs that could produce both Ca^{2+}- and global APs under our experimental conditions, stimulation of on average 5.5 ± 2.1 spines sufficed for Ca^{2+}-spike generation (at an average somatic threshold of -67.8 ± 7.6 mV), whereas activation of 9.0 ± 1.6 spines was required to elicit an AP (at a somatic threshold of -60.2 ± 8.8 mV; both spine number and threshold: $p < 0.001$ Ca^{2+}- vs Na^{+}-spike, Fig 11c). We also investigated Ca^{2+}-spike thresholds in 25 GCs that did not yet fire a Na^{+}-spike at the maximum number of stimulated spines, which showed no significant difference to those in spiking GCs (5.3 ± 2.3 spines and -72.1 ± 4.3 mV, respectively).

Thus, Ca^{2+}-spike generation required substantially lower numbers of coactive excitatory inputs than global AP generation. However, when cuEPSPs were aligned to Ca^{2+}-spike threshold spine number before averaging (Fig 11d), there was no discontinuous increase in amplitude at threshold (i.e. not significantly different from linear fit to subthreshold regime, see *3.3.7*), and also no significant increase in O/I ratio. Thus, the onset of a Ca^{2+}-spike as reported by dendritic $\Delta F/F$ is not substantially involved in the generation of V_m supralinearity.

Kinetics of the cuEPSP also did not change significantly at threshold (Fig 11e). Aside from the lack of EPSP boosting and broadening, there was another discrepancy between the Ca^{2+}-spike reported here and earlier observations, since the LTS generated by glomerular or external electrical field stimulation (Pinato and Midtgaard, 2005) was an all-or-none event that spread evenly throughout the GC dendrite, whereas here dendritic Ca^{2+}-spikes attenuated substantially while propagating from the activated spine set along the dendrite towards the soma (Fig 11b). Thus, the Ca^{2+}-spike reported here is mostly a regional signal, which also explains the lack of effects on somatic cuEPSP amplitude and kinetics. Beyond the Ca^{2+}-spike threshold, higher

numbers of activated spines resulted in larger dendritic ΔF/F signals with increased extent (Fig 11a, b; see also Fig 13a), which can be explained by the recruitment of additional voltage-dependent conductances (see below).

3.4.3 Transition to supralinear behavior due to dendritic Na^+-spikes (D-spikes)

Since Ca^{2+}-spike onset did not coincide with the transition to supralinear integration, we investigated the transition between linear and supralinear regimes in more detail in the GCs with supralinear sI/Os (n = 18). This transition happened at an average of 6.5 ± 2.7 spines, significantly higher than the spine number required for Ca^{2+}-spike onset and lower than the spine numbers for Na^+-spikes (Fig 12c). Arrangement of the data relative to the transition spine number (Fig 12d) show a significant discontinuous increase in cuEPSP amplitudes at threshold (i.e. significantly different from linear fit to subthreshold regime, see *3.3.7*), and a concomitant increase in mean O/I ratios. The alignment of cuEPSP kinetics to the spine number at the transition in amplitude also revealed highly significant increases of half duration $\tau\_1/2$, maximal rate of rise and rise time (Fig 12a, b, e).

An increased rate of rise could indicate the occurrence of a dendritic D-spike (Losonczy and Magee, 2006; Zelles *et al.*, 2006). Indeed, in 7 GCs (out of 35 spiking cells) distinct spikelets were detected at the soma, a hallmark of attenuated D-spikes (Fig 12a; Golding and Spruston, 1998; Stuart *et al.*, 2007; Llinas and Nicholson, 1971; Smith *et al.*, 2013; Epsztein *et al.*, 2010). However, how can such D-spikes be consistent with the observed increase in overall rise time? Previously, we had observed that single spine uEPSP rise time increased upon blocking of Na_vs by wash-in of Tetrodotoxin (TTX; Bywalez *et al.*, 2015).

This apparent discrepancy can be explained by a substantial latency of D-spikes. While we could not determine the peak of the D-spike in most GCs, the latency between TPU onset and the peak of spikelets was 21 ± 19 ms (median 10 ms; n = 7 GCs). The delayed occurrence of the D-spike increases the total rise time of the ΔV_m signal and also indicates that D-spikes are unlikely to be globalized spine spikes (see *3.5*).

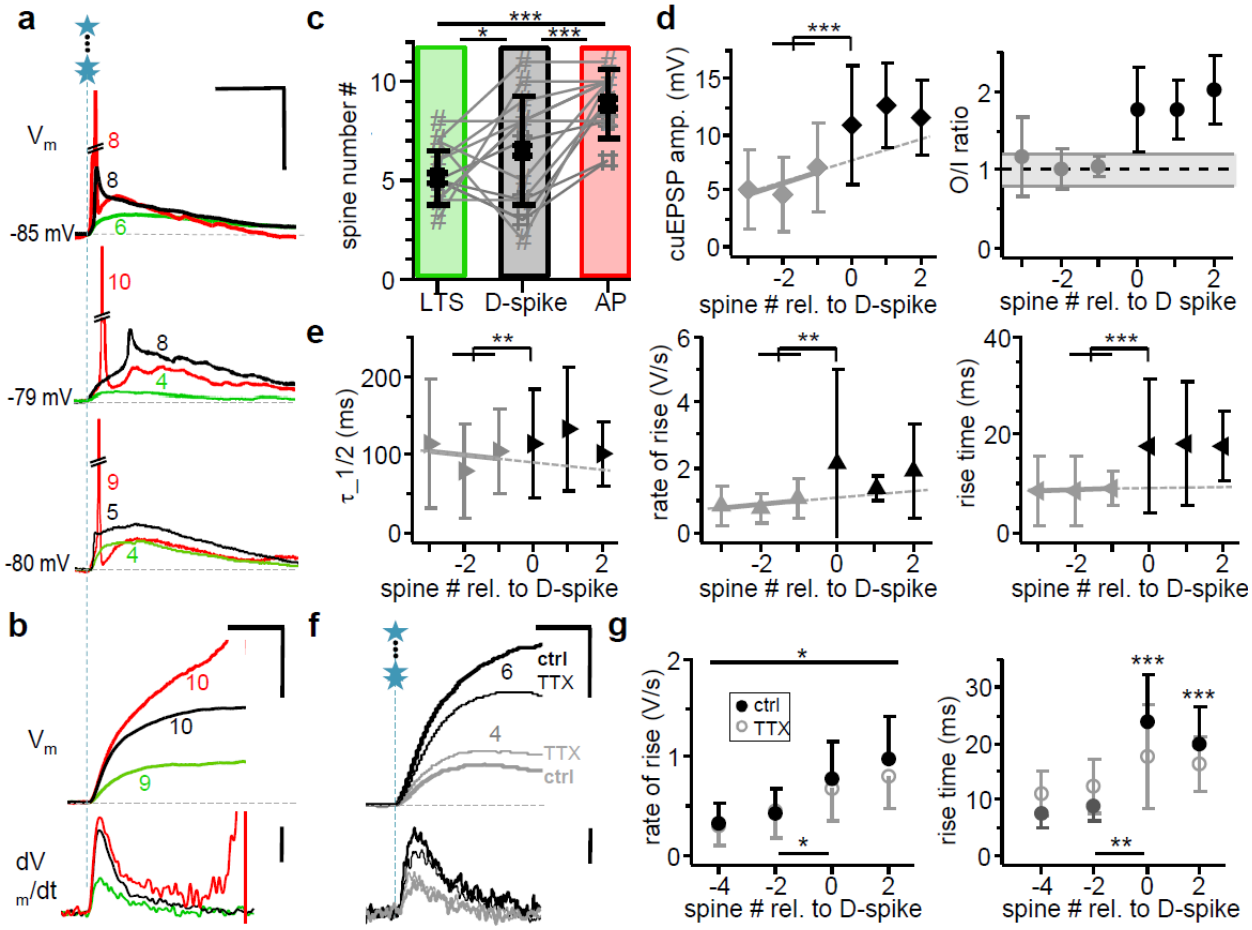

Fig 12. ***Dendritic Na^+-spikes.***

a: *Examples of somatic spikelets recorded from 3 different GCs at different number of coactivated spines. Green traces and spine numbers: Ca^{2+}-spike threshold. Black traces and numbers: Spikelets. Red traces and numbers: Full blown Na^+ APs, cut-off. Scale bars: 20 mV, 50 ms.* ***b:*** *Example cuEPSP V_m recording in rising phase (top, scale bars: 10 mV, 20 ms) and 1st derivative (bottom, scale bar: 1 V/s). Colors as in a, black here: D-spike, indicated by increase in rate of rise.* ***c:*** *Comparison of spine numbers sufficient to elicit Ca^{2+}-spike, D-spike and Na^+-AP in the same GCs (n = 18 GCs; $F_{(2,53)}$=20.753, p < 0.001, Ca^{2+}-spike: 5.1±1.4, D-spike: 6.5 ± 2.7, AP: 8.9 ± 1.7 Holm-Sidak post hoc: Ca^{2+}-spike vs D-spike: p = 0.027, Ca^{2+}-spike vs AP: p < 0.001, D-spike vs AP: p<0.001).* ***d:*** *Left: Mean somatic cuEPSP amplitudes with spine numbers aligned relative to D-spike threshold for GCs with supralinear sI/Os (n = 18). Difference between -2/-1 and 0 highly significantly different from extrapolated linear fit (p = 0.0001; Wilcoxon test, see 3.3.7, see Fig S4b for data points from individual experiments). Right: Mean O/I ratios aligned relative to D-spike. Increase from 1.03 ± 0.13 to 1.77 ± 0.54, not tested, since onset of supralinear O/I ratios was criterion for D-spike threshold.* ***e:*** *Kinetics of cuEPSPs (n = 18 GCs; spikelet data included): Highly significant increases beyond extrapolated linear fits at D-spike threshold for half duration (left, p = 0.009, n = 16), rate of rise (middle, p = 0.002, n = 18) or rise time (right, p < 0.001, n = 18). See Fig S4b for data points from individual experiments.* ***f:*** *Example for effect of TTX on cuEPSP kinetics below and at D-spike threshold (4 and 6 coactivated spines in this GC, respectively). Top traces: V_m, bottom: dV_m/dt, as in b. Grey traces: below D-spike threshold, black traces: at D-spike threshold. Thick lines: control, thin lines: in presence of 0.5 – 1 µM TTX. Note the reduction in maximal rate of rise at threshold but not subthreshold. Scale bars: 5 mV (top), 0.7 V/s*

(bottom), 20 ms. ***g:*** *Cumulative data for effect of TTX (n = 7 GCs with supralinear sI/Os) on cuEPSP rate of rise (left) and rise time (right). Repeated measures two-way ANOVA (see 3.3.6, also below): no interaction effect on rate of rise (spine # x TTX): $F_{(3,55)}$=3.058, p=0.055; TTX effect: $F_{(1,55)}$=8.249, p=0.028. Interaction effect on rise time (spine # x TTX): $F_{(3,55)}$=12.487, p<0.001. Asterisks indicate significance of differences between TTX and ctrl (* p=0.028, *** p<0.001). Asterisks at bottom indicate significance of differences of parameter increases from -2 to 0 between ctrl and TTX (Wilcoxon test; rate of rise: p < 0.05 (W = 17, n_{sr} = 6), rise time: p < 0.01 (W=28, n_{sr} = 7)). See Fig S4c for individual data points.*

Finally, we tested whether the observed changes in EPSP kinetics were indeed due to the activation of dendritic Na_Vs. Application of TTX (0.5 - 1 µM) to a set of 7 GCs with supralinear sI/Os significantly reduced both the increases in cuEPSP rise time and maximal rate of rise at supralinearity threshold (Fig 12f, g). Note that below threshold cuEPSP rise times were slowed in TTX, as expected for spine spike-mediated signals (Bywalez *et al.*, 2015).

Moreover, there was a significant increase in ΔCa^{2+} both in activated spines and in nearby dendrites associated with the transition to the D-spike in these experiments (see Fig 13d, f), which was also sensitive to Na_v blockade (Fig 13g, h). This observation further proves the presence of a Na_v-mediated D-spike, since dendritic Na_v activation will recruit both LVACCc and HVACCc and thus can further contribute to Ca^{2+}-spikes (Egger *et al.*, 2003; Isaacson and Vitten, 2003).

In conclusion, the supralinearity observed in the sI/Os of most GCs is due to the onset of a D-spike.

3.4.4 Ca^{2+}-, D- and global Na^+-spike each mediate substantial additional Ca^{2+} influxes into the spine

Apart from the D-spike, can Ca^{2+}-spikes and global APs also boost Ca^{2+} influx into spines that are already activated by local inputs? Such summation had been observed previously for both synaptically evoked APs and LTS (Egger *et al.*, 2005; Egger, 2008).

Fig 13a shows an exemplary transition from local spine activation to Ca^{2+}-spike to D-spike to full blown Na^+-AP, and in Fig 13b all normalized Ca^{2+} signals are arranged relative to Na^+-AP threshold in both spine S1 and dendrite. Since for low numbers of coactivated spines (1-4, not aligned to AP threshold, not shown) there was no significant difference in the S1 Ca^{2+} signal, we normalized S1 ΔF/F of each GC to its mean of S1 (1-4) to reduce variance (see *3.3.4*).

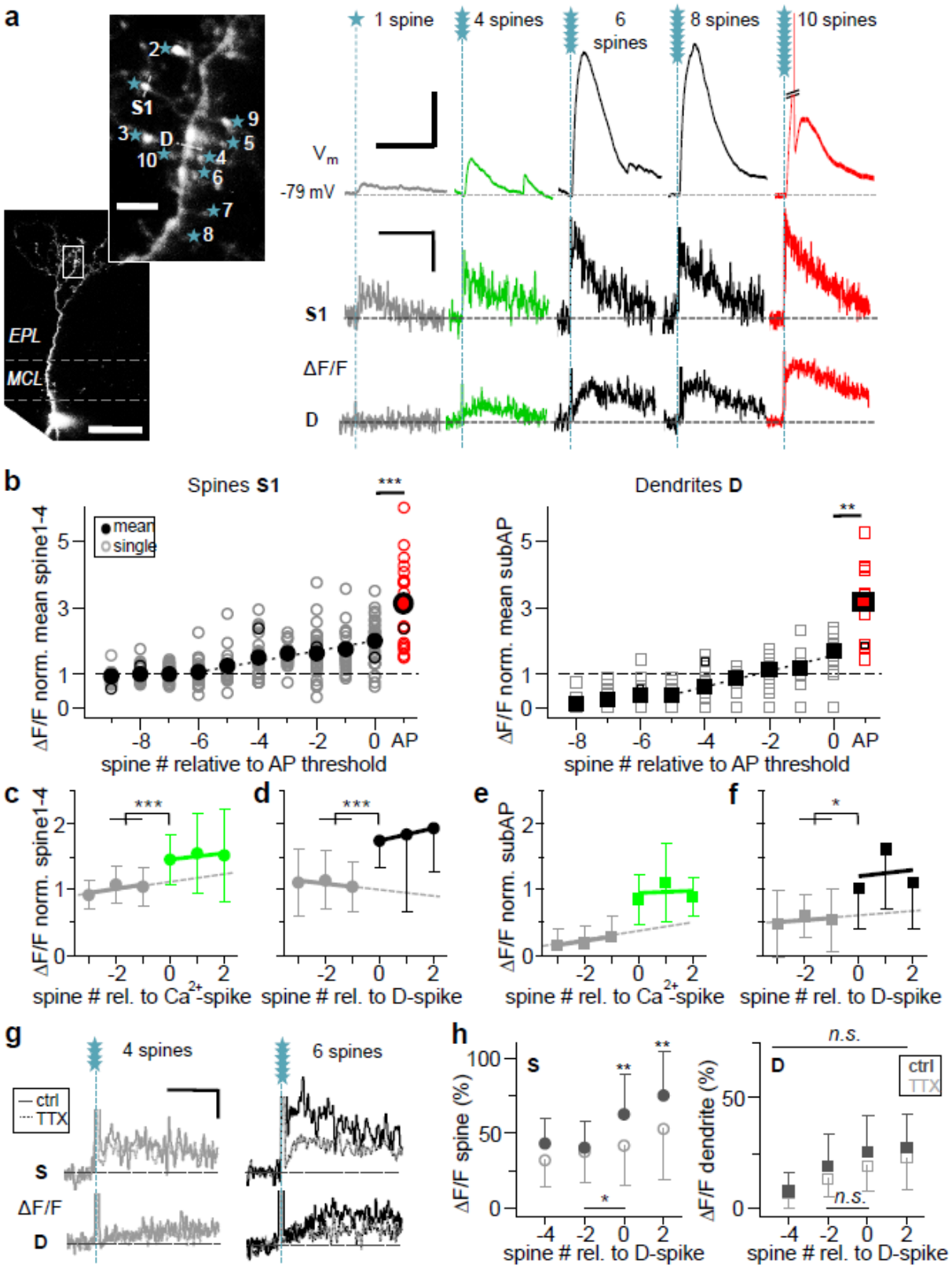

Fig 13. ***Additional ΔCa^{2+} in spine and dendrite due to non-local spikes.***

a: *Scan of representative granule cell (left, S1 and D indicate line scan sites, stars indicate uncaging spots, scale bars: 5 µm, 50 µm) with somatic V_m recordings (top right, scale bars: 5 mV, 200 ms) and line scans in spine S1 and dendritic location D for increasing spine numbers (bottom right, scale bars: 50 %, 2 s). Grey traces: below Ca^{2+}-spike, green traces: at Ca^{2+}-spike threshold; black traces: at and above D-spike threshold; red traces: suprathreshold for global Na^{+}-spike. APs cut-off for clarity.* ***b:*** *Left: Spine Ca^{2+} signals $(\Delta F/F)_{TPU}$ normalized to S1-4 (see 3.3.4) and aligned to AP threshold (n = 33 spines in 16 GCs); ○: individual spines,●: mean; ○: spine from* ***a****, ○: AP data from individual spines; ●: mean AP data (responses with more than 1 AP were not taken into account). Linear increase from -6 spines onwards (linear fit of mean values until 0: r^2 = 0.955, p < 0.001) of spine $(\Delta F/F)_{TPU}$ with highly significant additional increase upon AP generation (n = 20 pairs, Wilcoxon test, p < 0.001). Right: Dendritic Ca^{2+} signals $(\Delta F/F)_{TPU}$ normalized to mean above Ca^{2+}-spike threshold (see 3.3.4; n = 19 GCs). Symbols as in right panel, with squares instead of circles. Linear increase from -5 spines onwards (linear fit of mean values: r^2= 0.879, p<0.001) with significant additional increase upon AP generation (n = 12 pairs, Wilcoxon test, p=0.001).* ***c:*** *Spine $(\Delta F/F)_{TPU}$ normalized as above, arranged relative to Ca^{2+}-spike threshold (n = 26 in 14 GCs, Wilcoxon test, see 3.3.7, p < 0.001) and in* ***d*** *relative to D-spike threshold (n = 19 in 10 GCs, P < 0.001).* ***e:*** *Dendrite $(\Delta F/F)_{TPU}$ normalized as above, arranged relative to Ca^{2+}-spike threshold (left: n = 17, significance not tested, since increase in dendritic ΔF/F above noise level was criterion for Ca^{2+}-spike) and in* ***f*** *relative to D-spike threshold (n = 12, Wilcoxon test, p = 0.015).* ***g:*** *Example for effect of 0.5 – 1 µM TTX on ΔF/F below and at D-spike threshold (4 and 6 coactivated spines, respectively; same cell as in 12f). Grey traces: below D-spike threshold, black traces: at D-spike threshold. Solid lines: control, dotted lines: TTX. Note the reduction in spine (ΔF/F) by TTX at threshold but not subthreshold. Scale bars: 50 %, 400 ms.* ***h:*** *Cumulative data for effect of 0.5 -1 µM TTX (n = 7 GCs with D-spike) on (ΔF/F) in spines (left, n = 13) and dendrite (right, n = 7). Full symbols: control, open symbols: TTX. Repeated measures two-way ANOVA (see 3.3.6, also below): interaction effect on spine (ΔF/F) (spine # x TTX): $F_{(3,103)}$=3.195, p=0.035. No interaction effect on dendrite (ΔF/F): $F_{(3,55)}$=0.659, p=0.588; no TTX effect: $F_{(1,55)}$=5.106, p=0.065. Asterisks indicate significance of differences between TTX and ctrl (** p < 0.01). Asterisks at bottom indicate significance of differences of ΔF/F from -2 to 0 between ctrl and TTX (Wilcoxon test; spine S: p = 0.029 (W = 55, n_{sr} = 13), dendrite: not significant (W=-2, n_{sr} = 5)). See Fig S4c for individual data points. MCL: mitral cell layer, EPL: external plexiform layer.*

From 5 coactive spines below AP threshold onwards, S1 and dendritic ΔCa^{2+} increased in a linear fashion up to AP threshold. This observation seems to imply that an individual GC spine could 'know' about the number of coactive spines from 5 spines below AP threshold upwards, based on the average amount of extra Ca^{2+} entry.

However, arrangement of the data relative to Ca^{2+}-spike threshold (as detected in the dendrite, Fig 13e) revealed that below threshold spine (ΔF/F) was by and large constant, whereas at threshold a highly significant increase in ΔCa^{2+} occurred in S1 (by on average ± SD: 1.44 ± 0.80 $[0]_{Ca2+\text{-spike}}$ vs $[-1/-2]_{Ca2+\text{-spike}}$, n = 25 spines, Fig 13c).

Similarly, arrangement of the data relative to the D-spike threshold also revealed a highly significant step-like increase in S1 ΔF/F (by 1.75 ± 0.85 $[0]_{D\text{-spike}}$ vs $[-1/-2]_{D\text{-spike}}$, n = 18, Fig 13d), and a similar trend in dendritic ΔF/F (by 1.76 ± 0.74 $[0]_{D\text{-spike}}$ vs $[-1/2]_{D\text{-spike}}$, n = 9, Fig 13f). Finally,

global AP generation lead to yet more substantial, highly significant additional Ca^{2+} influx into both the spine (2.03 ± 1.11 [AP] vs [0], absolute 84 ± 59 % ΔF/F, n = 18) and the dendrite (2.03 ± 1.12 [AP] vs [0], absolute 41 ± 20 % ΔF/F, n = 11, both Fig 13b). Compared to the local spine spike, global APs increased spine Ca^{2+} entry by 3.08 ± 1.32 (Fig 13b), thus coincident local inputs and global APs are likely to summate highly supralinearly (see *3.5*).

From all these observations, we infer that all three types of non-local signals, Ca^{2+}-spike, D-spike and global AP, can mediate substantial additional Ca^{2+} influx into the spine on top of the contribution of the local spine spike, and that the apparently linear mean increase in spine ΔCa^{2+} (Fig 13b) is actually due to overlapping step-like increases due to Ca^{2+}-spike and D-spike onsets at different spine numbers in individual GCs. Thus, a GC spine 'knows' about the general excitation level of the GC, but cannot resolve individual added coactive spines. Similar step-like increases will occur in dendrites close to the activated spine set and also nearby silent spines (not receiving direct inputs), since those were found previously to respond with similar increases in ΔCa^{2+} to non-local spikes as dendrites (Egger *et al.*, 2005; Egger *et al.*, 2003; Egger, 2008).

3.4.5 Molecular mechanisms of integration: Na_Vs

We observed previously (Bywalez *et al.*, 2015) that single GC spine activation resulted in a local spine spike, mediated by Na_Vs. While most of the postsynaptic Ca^{2+} entry was mediated by NMDARs, the spine spike contributed additional Ca^{2+} by gating of HVACCs. Notably, somatic V_m was not reduced in amplitude by Na_v blockade, only slowed down in its kinetics, indicative of a strong filtering effect by the spine neck and possibly the GC dendrite (Bywalez *et al.*, 2015). A key question of our investigations was whether spine spikes themselves could eventually occur simultaneously across a few clustered spines and thus engender non-local spiking?

For all pharmacological interventions related to dendritic integration mechanisms below the global Na^+-spike threshold we stimulated 1, 2, 4, 6, 8, 10 spines before and after wash-in of the drug (see *3.3*). We blocked Na_Vs by wash-in of 0.5 - 1 µM TTX (n = 12 GCs, Fig 14 top). Amplitudes of single and cuEPSPs were unaltered (Fig 14b). However, the significant increase of average O/I ratios from 6 to 8 coactivated spines in control was blocked in the presence of TTX (Fig 14c). 4 of the 12 GCs fired an AP upon stimulation of 10 spines, which was always abolished by wash-in of TTX.

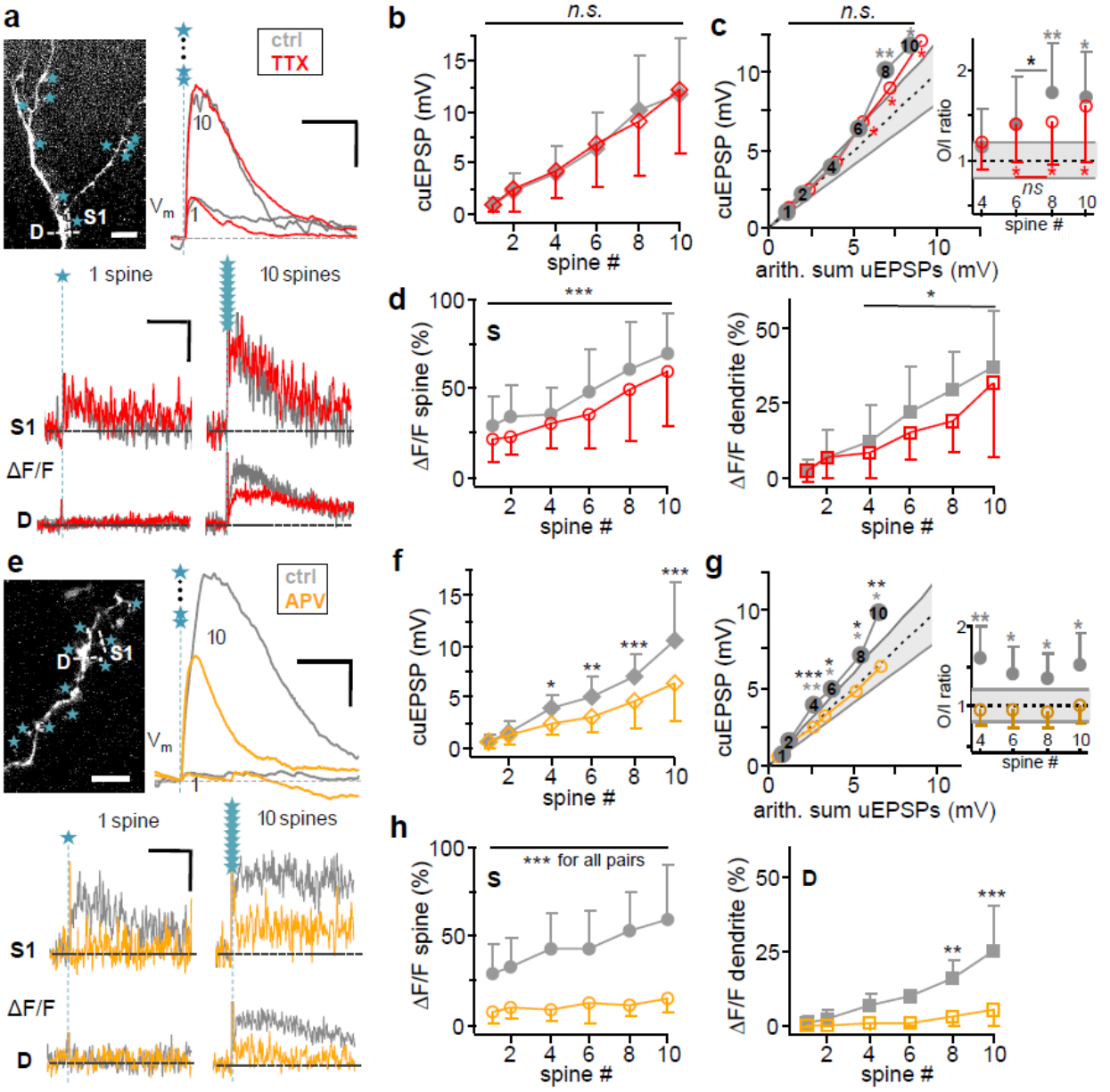

Fig 14. ***Molecular mechanisms of subthreshold integration: Na_vs and NMDARs***

a: *Example Na_v blockade experiment. Top left: Scan of stimulated spine set with indicated line scan sites S1, D and uncaging spots. Scale bar: 10 µm. Top right: Somatic V_m recording of cuEPSP for 1 and 10 coactivated spines, respectively. Scale bars: 5 mV, 100 ms. Bottom: $(\Delta F/F)_{TPU}$ in spine (S1) and dendrite (D) for 1 and 10 coactivated spines. Scale bars: 50 %, 1 s. Grey traces: Control. Red traces: TTX (0.5-1 µM).* ***b:*** *Average effect (n = 12 GCs) of 0.5-1 µM TTX on somatic cuEPSP amplitude upon activation of 1,2,4,6,8,10 spines. Repeated measures two-way ANOVA (see 3.3.6, also below): no interaction effect (spine # x TTX): $F_{(5,119)}$=2.542, p=0.091; no TTX effect: $F_{(1,119)}$=0.965, p=0.352.* ***c:*** *Effect (n = 12 GCs) of Na_v blockade on averaged sI/O upon activation of 1-10 spines. No interaction effect (spine # x TTX): F(5,99)=1.602, p=0.195; no TTX effect: $F_{(1,99)}$=0.835, p=0.385 (n.s. above data points). Dashed line indicates linear summation, solid grey lines indicate supralinearity (1.2) and sublinearity (0.8). Asterisks/ Significance levels refer to O/I ratio distributions with means beyond the linear regime (0.8-1.2) tested against linearity (as in Fig 1c; see inset,*

*3.3). The average O/I ratio for 8 spines was highly significantly supralinear in control (** above data points, p < 0.01) and significantly increased vs the O/I ratio for 6 spines (* in inset, p < 0.05, Wilcoxon test). While O/I ratios in TTX were significantly supralinear (* below data points, p < 0.05 for all), the increase from 6 to 8 spines disappeared in TTX (inset, n.s.).* ***d:*** *Effect of Na_v blockade on average spine S (left, n = 25 spines in 11 GCs) and dendrite D (right, n = 12 GCs) $(\Delta F/F)_{TPU}$ upon activation of 1-10 spines. No interaction effect on spine $(\Delta F/F)_{TPU}$ (spine # x TTX): $F_{(5,239)}$=1.686, p=0.145; TTX effect: $F_{(1,239)}$=15.164, average reduction to 0.89 ± 0.54 of control, p<0.001. No interaction effect on dendrite $(\Delta F/F)_{TPU}$ from 4 spines onwards (spine # x TTX): $F_{(3,79)}$=0.457, p=0.715; TTX effect: $F_{(1,79)}$=9.289, average reduction to 0.75 ± 0.28 of control, p=0.014. Asterisks above error bars indicate significance of differences between TTX and ctrl (* p<0.05, *** p<0.001).* ***e:*** *Example NMDAR blockade experiment with strong NMDAR signaling component. Top left: Scan of stimulated spine set with indicated line scan sites S1 ,D and uncaging spots. Scale bar: 10 µm. Top right: Somatic V_m recording of cuEPSP for 1 and 10 coactivated spines, respectively. Scale bars: 10 mV, 200 ms. Bottom: $(\Delta F/F)_{TPU}$ in spine (S1) and dendrite (D) for 1 and 10 coactivated spines. Scale bars: 50 %, 1 s. Grey traces: Control. Dark yellow traces: APV (25 µM).* ***f:*** *Average effect (n = 8 GCs) of 25 µM APV on somatic cuEPSP amplitude upon activation of 1,2,4,6,8,10 spines. Interaction effect (spine # x APV): F(5,95)=8.08, p<0.001. Black asterisks indicate significance of differences between APV and control (* p<0.05, ** p<0.01, *** p<0.001).* ***g:*** *Effect of NMDAR blockade on averaged sI/O upon activation of 1-10 spines. Interaction effect (spine# x APV): $F_{(5,95)}$= 3.37, p=0.014, n = 8. Black asterisks above data points indicate significance of differences between APV and control (* p<0.05, **p <0.01, *** p<0.001). Dashed line indicates linear summation, solid grey lines indicate supralinearity (1.2) and sublinearity (0.8). Grey asterisks/significance levels refer to O/I ratio distributions with means beyond the linear regime (0.8-1.2) tested against linearity (as in c, see inset, 3.3.6). At control, O/I ratios from 4 spines upwards were supralinear, which entirely disappeared in APV.* ***h:*** *Effect of NMDAR blockade on average spine S (left, n = 15 spines) and dendrite D (right, n = 8) $(\Delta F/F)_{TPU}$ upon activation of 1-10 spines. Interaction effect on spine $(\Delta F/F)_{TPU}$ (spine # x APV): $F_{(5,179)}$=6.36; p<0.001. Interaction effect on dendrite $(\Delta F/F)_{TPU}$ (spine # x APV): $F_{(5,95)}$=8.34, p<0.001. Asterisks indicate significance of differences between APV and control (**p<0.01, ***p<0.001).*

In 7 out of the 12 GCs summation was supralinear, and as shown above (Fig 12), supralinear integration is associated with the occurrence of D-spikes. Indeed, the supralinear increase in V_m at threshold was significantly reduced in the presence of TTX (Fig S4c).

Across all 12 GCs the S1 spine Ca^{2+} signal and dendritic Ca^{2+} signals were significantly and similarly reduced in TTX across all numbers of activated spines (Fig 14d; spine: 0.89 ± 0.54 of control, p<0.001; dendrite: 0.75 ± 0.28 of control, p=0.014). Moreover, as shown above, the stepwise increase in spine ΔCa^{2+} at D-spike threshold (Fig 13d) was abolished in TTX (Fig 13g, h).

In summary, Na_v blockade had only subtle effects on somatic V_m summation and thus spine spikes are unlikely to play a major role (see also *3.5*). Dendritic Na_v activation however underlies the D-spike and the additional Ca^{2+} entry in both spines and dendrites associated with it.

3.4.6 Molecular mechanisms of non-local spikes: key role of NMDARs

NMDARs have been shown to contribute substantially to local postsynaptic signaling in GCs (Bywalez *et al.*, 2015; Isaacson and Strowbridge, 1998; Egger *et al.*, 2005) and to also foster the generation of global Ca^{2+}-spikes (Egger *et al.*, 2005). To investigate the contribution of NMDARs to integration, we blocked NMDARs by wash-in of APV (25 µM) in n = 8 experiments (Fig 14 bottom).

The cuEPSP amplitude was substantially reduced from 4 activated spines onwards (Fig 14e, f). While under control conditions we observed supralinear integration from 4 spines onwards, blocking of NMDARs switched the average sI/O relationship to linear integration (Fig 14g). In 2 experiments cells fired an AP upon stimulation of 10 spines under control conditions and in 1 of these we could record spikelets at the soma upon stimulation of 8 and 10 spines. All were abolished by wash-in of APV.

APV also highly significantly reduced S1 spine Ca^{2+} signals for all stimulation strengths, effectively blocking the on average linear control increase in ΔCa^{2+} (e.g. at 8 costimulated spines spine $\Delta F/F$: 0.25 ± 0.18 of control, $p < 0.001$; Fig 14h). Moreover, APV strongly reduced dendritic ΔCa^{2+} and thus prevented Ca^{2+}-spike generation (Fig 14h; e.g. at 8 spines dendrite $\Delta F/F$: 0.14 ± 0.15 of control, $p = 0.003$). APV did reduce the half duration of cuEPSPs from 4 spines onwards (interaction effect (spine # x APV): $F_{(5,95)}=3.202$, $p=0.017$, absolute mean values at 8 coactivated spines: τ_1/2 control 90 ± 53 ms, APV 37 ± 21 ms, data not shown) but did not interfere with fast kinetics, e.g. the maximal rate of rise of the cuEPSP (no interaction effect (spine # x APV): $F_{(5,95)}=1.616$, $p=0.182$; no APV effect: $F_{(1,95)}=2.261$, $p=0.176$, n = 8 GCs, data not shown).

Thus, on top of the already known strong contribution of NMDARs to local postsynaptic Ca^{2+} entry, all forms of non-local spikes and their associated Ca^{2+} influxes are highly NMDAR dependent, even though NMDAR activation happens in the electrically isolated spine heads (see *3.5*).

3.4.7 Molecular mechanisms of non-local spikes: contribution of both low and high-voltage-activated Ca_Vs to dendritic Ca^{2+} entry

To verify whether distally evoked Ca^{2+}-spikes in GC dendrites are mediated by T-type Ca_Vs as observed earlier for global Ca^{2+}-spikes evoked by glomerular stimulation (Egger *et al.*, 2005), we investigated their contribution to GC multi-spine signals in n = 11 GCs. Wash-in of 10 µM mibefradil did not alter cuEPSPs upon activation of up to 8 spines. Only for 10 spines cuEPSPs were slightly but significantly reduced by on average 0.8 ± 1.4 mV (p=0.01, Fig 15b). Under control conditions activation of 10 spines also lead to supralinear V_m summation (Fig 15c), which was reduced by blockade of T-type Ca_Vs. CuEPSP kinetics were unaltered (data not shown). In one experiment an AP was generated upon stimulation of 10 spines under control conditions, which was abolished in the presence of mibefradil.

Ca^{2+} signals in spine S1 and dendrite were significantly reduced for all spine numbers (spine: average ± SD 0.74 ± 0.31 of control, $p < 0.001$; dendrite: 0.74 ± 0.38 of control, p=0.003, Fig 15d). However, mibefradil did not entirely block dendritic ΔCa^{2+} upon stimulation of 4 spines and beyond (remaining signal 16 ± 9 % ΔF/F at 10 coactivated spines).

To identify the source for the remaining dendritic $\Delta F/F_{TPU}$, we additionally washed in 100 µM Cd^{2+} to block HVACCs in 4 cells (Isaacson and Vitten, 2003). Cd^{2+} effectively abolished the dendritic Ca^{2+} signal and substantially further reduced the S1 spine Ca^{2+} signal to 0.52 ± 0.26 of mibefradil or 0.41 ± 0.22 of control (n = 8 spines), leaving the cuEPSP unaltered (Fig 15 e-g).

We conclude that T-type Ca_Vs substantially contribute to Ca^{2+} entry into the spine and dendrite during dendritic integration and mediate the onset of the Ca^{2+}-spike, but that HVACCs also contribute, most likely involving additional Ca^{2+} entry via L-type Ca_Vs or other channel types that are activated by D-spikes. Both LVACCs and HVACCs did not substantially influence somatic ΔV_m in our stimulation paradigm.

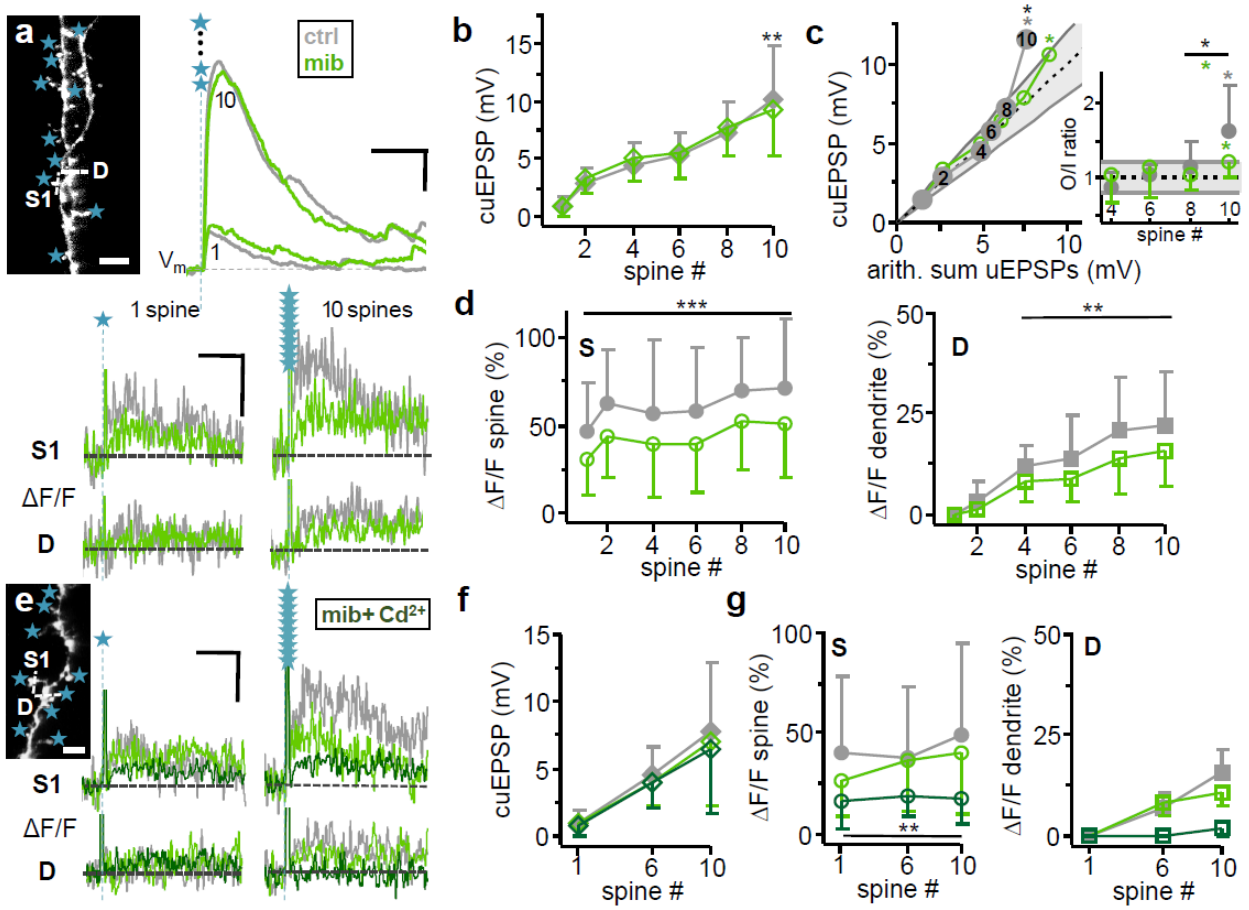

Fig 15. ***Molecular mechanisms of subthreshold integration: LVACC and HVACC***
a: *Example LVACC blockade experiment. Top left: Scan of stimulated spine set with indicated line scan sites S, D and uncaging spots. Scale bar: 5 µm. Top right: Somatic V_m recording of cuEPSP for 1 and 10 coactivated spines, respectively. Scale bars: 2 mV, 100 ms. Bottom: $(\Delta F/F)_{TPU}$ in spine (S1) and dendrite (D) for 1 and 10 coactivated spines. Scale bars: 40 %, 1 s Grey traces: control. Green traces: Mibefradil (10 µM).* ***b:*** *Average effect (n = 11 GCs) of 10 µM Mibefradil on somatic cuEPSP amplitude upon activation of 1, 2, 4, 6, 8, 10 spines. Repeated measures two-way ANOVA (see 3.3.6, also below): interaction effect (spine # x Mibefradil) $F_{(5,131)}=3.88$, $p = 0.010$. Asterisks indicate significance of differences between Mibefradil and control (** p = 0.01).* ***c:*** *Average effect (n = 8 GCs) of LVACC blockade on averaged sI/O upon activation of 1-10 spines. Interaction effect (spine # x Mib) $F_{(4,69)}=4.695$, $p=0.006$. Black asterisks above error bars indicate significance of differences between Mibefradil and control (* p<0.05). Dashed line indicates linear summation, solid grey lines indicate supralinearity (1.2) and sublinearity (0.8). Grey and green asterisks/significance levels above error bars refer to O/I ratio distributions with means beyond the linear regime (0.8-1.2) tested against linearity (*,* p<0.05, as in Fig 10c; see inset, 3.3.3). Integration was significantly supralinear at 10 spines for both control and Mibefradil, as well as the increase in O/I ratios between 8 and 10 spines. However, the O/I ratio increase between 8 and 10 spines in Mibefradil was significantly smaller than for control (inset, Wilcoxon test, * p < 0.05).* ***d:*** *Effect of LVACC blockade on average spine S1 (left, n = 26 spines in 11 GCs) and dendrite D (right, n = 11) $(\Delta F/F)_{TPU}$ upon activation of 1-10 spines. No interaction effect on spine $(\Delta F/F)_{TPU}$ (spine # x Mibefradil): $F_{(5,311)}=0.261$, $p=0.933$; Mibefradil effect: $F_{(1,311)}=60.16$, $p<0.001$. No interaction effect on dendrite $(\Delta F/F)_{TPU}$ (spine # x Mibefradil): $F_{(3,87)}=1.114$, $p=0.359$; Mibefradil effect: $F_{(1,87)}=15.84$, $p=0.003$. Asterisks indicate significance of differences*

*between Mibefradil and control (** p<0.01, *** p<0.001).* ***e:*** *Example for subsequent blockade of LVACCs and HVACCs. $(\Delta F/F)_{TPU}$ in spine (S1) and dendrite (D) for 1 and 10 coactivated spines. Top left inset: Scan of stimulated spine set with indicated line scan sites S1, D and uncaging spots. Scale bar: 5 µm. Grey traces: Control. Green traces: Mibefradil (10 µM). Dark green traces: added Cd^{2+} (100 µM). Scale bars: 20 %, 1 s.* ***f:*** *Effect of subsequent LVACC and HVACC blockade on somatic cuEPSP amplitude upon activation of 1, 6 and 10 coactivated spines (n = 4 GCs).* ***g:*** *Effect of subsequent LVACC and HVACC blockade upon activation of 1, 6 and 10 spines on spine $(\Delta F/F)_{TPU}$ (left, n = 8 spines in 4 GCs) and dendrite $(\Delta F/F)_{TPU}$ (right, n = 4). No interaction effect of Cd^{2+} wash-in after Mibefradil on spine $(\Delta F/F)_{TPU}$ (spine # x Cd^{2+}): $F_{(2,47)}$=1.514, p=0.254; Cd^{2+} effect: $F_{(1,47)}$=14.02, p=0.007. Asterisks indicate significance of differences between Mibefradil+Cd^{2+} and Mibefradil (** p<0.01).*

3.4.8 Morphology influences non-local spike generation only subtly

To determine whether the spacing of stimulated spines, the location of the stimulated spine set on the dendrite relative to the MCL, the average spine neck length and other morphological parameters influenced the efficacy of activated subsets of spines to elicit non-local spiking, we analyzed the positions of the stimulated spines relative to the GCs' dendritic tree as reconstructed in 3D (Fig 16, see *3.3.5*). Table S1 shows that only 2 out of 9 morphological parameters correlated with Ca^{2+}-spike threshold in terms of coactivated spine numbers, whereas both D-spike and global Na^{+}-spike initiation threshold spine numbers did not correlate significantly with any morphological parameter, with a weak trend for a positive correlation between spine distribution and global Na^{+}-spike initiation (Fig 16c). Ca^{2+}-spike generation was facilitated by close packing of spines that were located on the same and/or a rather low # of branches (Fig 16 c, d).

Thus, within the experimentally accessible range of parameters individual spine sets have by and large an equal impact on local and global Na^{+}-spike generation, independent from GC morphology or their relative location on the dendritic tree, which indicates a highly compact GC dendrite and strong isolation of the spines. For Ca^{2+}-spike generation clustered spines are more efficient than distributed inputs.

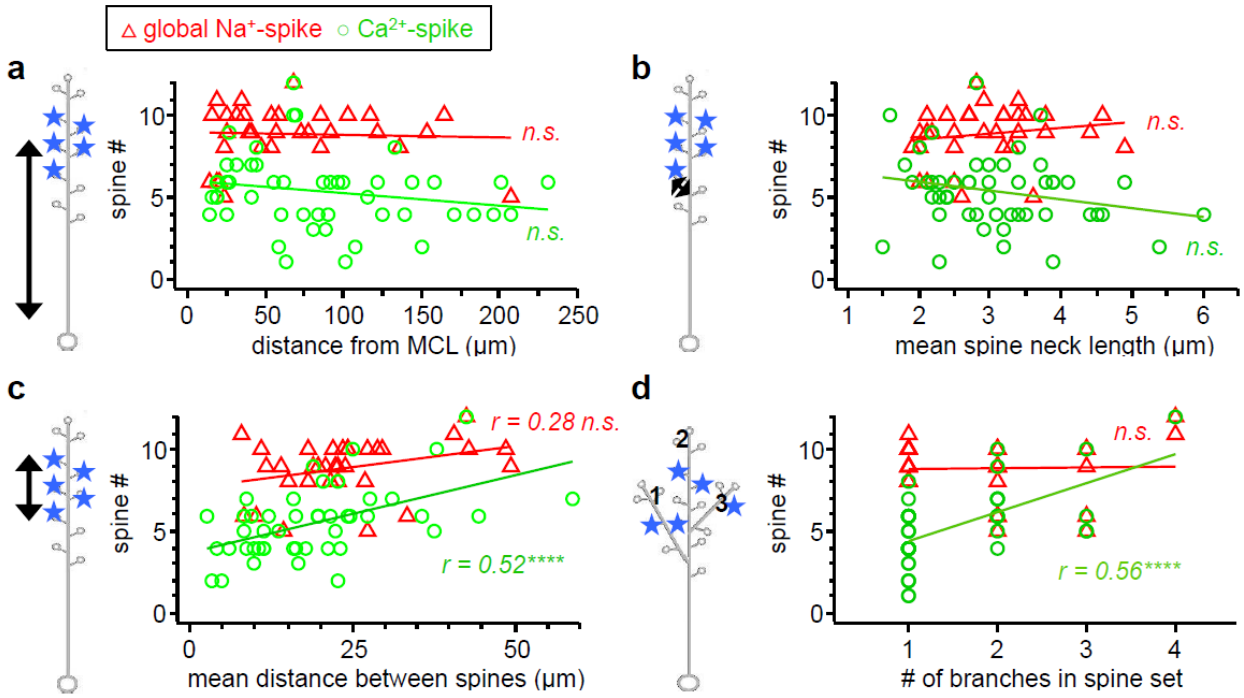

Fig 16. ***Impact of morphological parameters on threshold spine number for Ca^{2+}-spike and Na^{+}-spike generation.*** *Ca^{2+}-spike data (n = 47 spine sets) are denoted by ○ and global Na^{+}-spike data (n = 31 spine sets) by Δ. D-spike data not shown for clarity (but see Table S1). Linear correlation indicated by correlation coefficient r. See Table S1 for power of regressions.* ***a:*** *Influence of mean spine distance from the mitral cell layer (MCL) on spine # to elicit Ca^{2+}-spikes (r^2 = 0.019, p = 0.173) and global Na^{+}-spikes (r^2 = 0, p = 0.892).* ***b:*** *Influence of the mean spine neck length of activated spine sets on spine # to elicit Ca^{2+}-spikes (r^2 = 0.030, p = 0.120) and global Na^{+}-spikes (r^2 = 0, p = 0.35).* ***c:*** *Influence of the spatial distribution of activated spines on spine # to elicit Ca^{2+}-spikes (r^2 = 0.26, p < 0.001, n=47) and global Na^{+}-spikes (r^2 = 0.077, p=0.064).* ***d:*** *Influence of number of different dendritic branches that the spine set is distributed across on spine # to elicit Ca^{2+}-spikes (r^2 = 0.31, p < 0.001, n = 47) and global Na^{+}-spikes (r^2 = 0, p = 0.91).*

3.5 Discussion

3.5.1 High excitability of GC apical dendrites

Upon holographic simultaneous multi-spine stimulation, GC dendrites can generate Ca^{2+}-, D- and Na^{+}-spikes already at rather low numbers of coactivated dendrodendritic inputs (Ca^{2+}-spike ~ 5 inputs, D-spike ~ 7 inputs, global Na^{+}-spike ≥ 9 inputs). Thus, GC dendrites are highly excitable, also in comparison to cortical PCs whose AP threshold required a similar number of coactive spines using the very same holographic system (10 ± 1, n = 7 in 4 PCs, Go *et al.*, 2019) although the PCs' resting potential was depolarized versus GCs by ≥ +10 mV. This high excitability is not due to excessive photostimulation, since the average single EPSP amplitude was smaller in our

experiments than in earlier reports on MC/TC-GC synaptic transmission (Bywalez *et al.*, 2015; Pressler and Strowbridge, 2017).

Our data also demonstrate that the full set of active dendritic mechanisms known from other neurons (see *3.2*) can be triggered solely by dendrodendritic MC/TC inputs to the apical GC dendrite. Because of their location close to the MCL the GCs in our sample (see *3.3.1*) belong to sGCs (or type III), that preferentially synapse on TC lateral dendrites (Nagayama *et al.*, 2014). sGCs are reportedly more excitable than deep GCs (Burton and Urban, 2015), thus our results might not generalize to all GC subtypes, possibly explaining the discrepancy with earlier estimates of excitability (see 3.2; Pressler and Strowbridge, 2017).

The somatic AP threshold (~ -60 mV) was substantially below Na_v activation threshold, indicating a distal AP initiation zone. The threshold spine number reported here is a lower limit, since in ~2/3 of GCs in our sample full-blown APs at the soma could not yet be elicited at the maximal number of 10 - 12 co-stimulated spines (with the available laser power as bottle neck). Morphological parameters did not influence AP thresholds, indicating that the sGC's dendritic tree is electrotonically compact (see also below).

The low threshold spine number seems to match previous observations that uniglomerular stimulation can already fire GCs (Egger, 2008; Schoppa *et al.*, 1998; Geramita *et al.*, 2016). On the other hand, ~20 MC/TCs belong to a glomerular column, with a slight lower share of TCs (Panhuber *et al.*, 1985; Liu *et al.*, 2016a; Royet *et al.*, 1998). The release probability at these inputs is ~0.5 (Egger *et al.*, 2005) and thus for uniglomerular activation a given GC is unlikely to be fired solely from intracolumnar dendrodendritic inputs, requiring additional activation most likely originating from MC/TC axonal collaterals (Schoppa, 2006a). However, uniglomerular inputs - if clustered - might suffice to elicit local Ca^{2+} spikes, and MC/TC theta bursts as both observed *in vivo* (Fukunaga *et al.*, 2012) could also trigger firing of intracolumnar GCs from the distal apical dendrite.

The high excitability of GCs and the frequent supralinear subthreshold integration indicate a strong role for active conductances in dendritic integration.

3.5.2 Dendritic spiking: D-spike and localized Ca^{2+}-spike

A substantial presence of dendritic Na_v channels in GCs was already indicated by a backpropagation study (Egger *et al.*, 2003) and recently demonstrated more directly (Nunes and Kuner, 2018). Na^+ spikelets have not been reported from juvenile rat OB GCs so far; they probably emerged here due to clustered stimulation. In about 2/3 of GCs in our sample we detected D-spikes correlated with the onset of supralinear integration at the soma either as distinct spikelets or, if these were masked by electrotonic filtering, by characteristic step-like increases in the cuEPSP rate of rise, rise time, decay and spine ΔF/F (Fig 12). Significant increases in the EPSP rate of rise and dendritic ΔCa^{2+} indicated D-spikes in CA1 PCs and mouse and frog GCs (Losonczy and Magee, 2006; Burton and Urban, 2015; Zelles *et al.*, 2006). The unexpected increase in cuEPSP rise time by almost ∼10 ms can be explained by the substantial latency of spikelets of ∼10-20 ms after TPU onset. This delay indicates that D-spikes are not spatially expanded spine spikes, implying that spine spikes are unlikely to invade the dendrite even under conditions of clustered spine activation, which is further supported by the lack of a correlation between spatial clustering and D-spike or Na^+-spike threshold spine numbers. Rather, EPSPs are strongly attenuated and also temporally filtered across the spine neck, resulting in slowed integration (Aghvami and Egger 2020, unpublished simulations); moreover, A-type K^+ currents are known to delay GC firing (Schoppa and Westbrook, 1999) and thus also possibly involved in the yet longer latency of global Na^+-APs at threshold observed here (∼40 ms). Initiation of D-spikes most likely happens at dendritic Na_v hot-spots (Nunes and Kuner, 2018), whereas the existence of a dedicated global Na^+-AP initiation zone in GC apical dendrites seems probable, with its precise location a matter of speculation at this point (but see Pressler and Strowbridge, 2019).

All GCs in our sample featured Ca^{2+}-spikes (in terms of dendritic Ca^{2+} entry), which at threshold were rather regional, decreasing strongly towards the soma. Although Ca_v densities are apparently lower in the proximal apical dendrite (Egger *et al.*, 2003), Ca^{2+}-spikes evoked by glomerular stimulation occurred in an all-or-none fashion throughout the entire dendritic tree with a concomitant increase and broadening of somatic EPSPs that were not observed here (Egger *et al.*, 2005). We conclude that the main initiation zone for global Ca^{2+}-spikes is probably

not located in the distal apical dendritic tree (see also Pressler and Strowbridge, 2019). Thus, in contrast to the global Ca^{2+}-spike upon glomerular activation, input to rather densely packed spines might provide a substrate for more local lateral inhibition as suggested earlier (Woolf *et al.*, 1991a; Woolf and Greer, 1994; Isaacson and Strowbridge, 1998). Anyways, local Ca^{2+}-spikes became more global close to Na^{+}-AP threshold, along with recruitment of HVACC. Thus, GCs feature multiple levels of compartmentalization.

In contrast to AP generation, Ca^{2+}-spike generation is strongly influenced by input distribution, in line with electrotonic attenuation of subtreshhold EPSPs along the dendrite (Tran-Van-Minh *et al.*, 2015). Since the Ca^{2+}-spike precedes the D-spike and AP and its space constant of $\gtrsim 60$ µm covers the maximum spatial extent of spine sets in our experiments, its presence can reduce passive attenuation and thus explain the independence of D-spike and AP generation from input distribution within the spatial regime accessible by our system. Which in turn means that D-spike and global APs are insensitive to spatial changes in local input distributions.

3.5.3 NMDA-spikes and role of NMDARs in GC synaptic processing

NMDARs contribute substantially to supralinear integration in GCs, both at the level of V_m and ΔCa^{2+}. They are required for Ca^{2+}-spike generation and their blockade had a much stronger effect on V_m supralinearity than Na_v or Ca_v blockade alone. This higher efficiency is probably related to the slower kinetics of the NMDAR component, which therefore is filtered much less both by the spine neck and then along the dendritic tree compared to Na_v or Ca_v mediated currents (Stuart *et al.*, 2016). Conversely, strong filtering of Na_v currents explains the small influence of TTX on somatic dendritic integration observed here. The substantial impact of NMDARs on GC dendritic integration is characteristic for NMDA-spikes (Maccaferri and Dingledine, 2002; Antic *et al.*, 2010). Accordingly, GC APs evoked by synaptic stimulation are followed by NMDAR-dependent plateau potentials (Egger, 2008; Stroh *et al.*, 2012). In most GCs, EPSP half durations were > 50 ms at higher numbers of coactive spines, thus dendritic Ca^{2+}- and Na^{+}-spikes are closely intertwined with NMDA-spikes.

As a note of caution, holographic uncaging might overemphasize the role of NMDARs, since (1) APV blocks TPU-evoked spine ΔF/F slightly more than synaptic ΔF/F (to 65% vs 50% of control, Bywalez *et al.*, 2015) and (2) the axial point spread function of our multi-site uncaging system is

extended to 2.7 µm (Go *et al.*, 2019) from 1.1 µm, which might activate yet more extrasynaptic NMDARs. However, the effect on APV on single spine $(\Delta F/F)_{TPU}$ was similar as in Bywalez *et al.* (2015).

NMDARs are predicted to enable supralinear summation of ΔCa^{2+} at positive Hebbian pairing intervals of single spine spike and global APs (Aghvami *et al.*, 2019). The median latency of global Na^{+} APs at threshold of 35 ms observed here matches with the simulated regime of maximally supralinear summation efficiency, which explains the strong increase of ΔCa^{2+} in spines upon AP generation. In conclusion, NMDARs are essentially involved in all aspects of GC reciprocal synaptic processing, including release of GABA from reciprocal spines (Lage-Rupprecht *et al.*, 2019) and synaptic plasticity (Chatterjee *et al.*, 2016; Neant-Fery *et al.*, 2012).

3.5.4 Functional implications

Our findings imply that dendritic spikes and therewith possibly lateral inhibition can be invoked already at very low numbers of coactive spines. The observed stepwise increases in spine and dendrite ΔCa^{2+} at the three spike thresholds imply that release probabilities for GABA (which is ~0.3 for local stimulation, Lage-Rupprecht *et al.*, 2019) might also be increased in a step-like fashion, thus rendering both lateral and recurrent inhibition more effective. GC-mediated lateral inhibition is thought to implement contrast enhancement and synchronization of gamma oscillations across glomerular columns responding to the same odorant (Urban and Arevian, 2009; Fukunaga *et al.*, 2014; Peace *et al.*, 2017). Fast gamma oscillations in the bulb are generated at the GC-MC/TC synapse independently of global APs (Lagier *et al.*, 2004; Schoppa, 2006b) and require a fast excitatory-inhibitory feedback loop (Pouille *et al.*, 2017; Fukunaga *et al.*, 2014), that is likely to involve both reciprocal and lateral processing. D-spikes could be powering fast oscillatory lateral and recurrent output as they have shorter latencies than global bpAPs. Zelles *et al.* (2006) already proposed interaction of D-spikes and bpAPs in GCs at intervals as short as 5-6 ms and also Pinato and Midtgaard (2005) could elicit spikelets at a frequency of 150-250 Hz, whereas the maximum frequency of global GC APs is much lower (10-30 Hz). *In vivo,* GCs display only sparse, long latency AP firing (Cang and Isaacson, 2003; Kato et al., 2012), whereas spikelets have been frequently observed (Wellis and Scott, 1990; Labarrera *et al.*, 2013; Mori and Takagi, 1978; Luo and Katz, 2001). Similarly, D-spikes are associated with sharp wave-associated ripples

(120-200 Hz) in hippocampal CA1 PCs (Klausberger *et al.*, 2004; Kamondi *et al.*, 1998; Memmesheimer, 2010).

The supralinear integration in GC dendrites is at variance with that in subtypes of retinal amacrine cells who also release GABA from their dendrites. In these cells dendritic Na_Vs do not amplify EPSPs and compartmentalization is high (Grimes *et al.*, 2010), most likely because spatial organization of lateral inhibition in the retina is continuous.

Changes in GC spine and dendrite ΔCa^{2+} were not necessarily correlated with changes in somatic V_m amplitude (both for the localized Ca^{2+} spike and the attenuated D-spike), allowing for multiplexed signals as proposed for cerebellar GCs (Tran-Van-Minh *et al.*, 2016), which in bulbar GCs might implement e.g. independent plasticity induction across reciprocal spines (Chatterjee *et al.*, 2016). On a yet more speculative note, different GC spike types might encode for different types of odor information. Such multiplexing of odor information was already described for MCs in zebrafish, where wave-like, most likely GC-mediated, gamma oscillations and tightly phase-locked spiking are tied to odor category and odor identity, respectively (Friedrich *et al.*, 2004).

3.6 Supporting information

Table S1. ***Regression between coactivated threshold spine numbers for Ca^{2+}-spike, D-spike, and global Na^{+}-spike and various morphological parameters and input patterns*** *(see 3.3.5). n: number of analyzed spine sets, r^2: adjusted coefficient of determination, p-value: two-tailed significance level of regression, COF: coefficient constant. Statistically significant values are highlighted in yellow.*

	Influence on generation of											
	Ca^{2+}-spike (n = 47)				**D-spike (n = 20)**				**global Na^{+}-spike (n = 31)**			
Parameter	r^2	p	COF	power	r^2	p	COF	power	r^2	p	COF	power
Spine distribution	0.257	<0.001	0.092	0.970	0.000	0.601	0.041	0.074	0.077	0.064	0.051	0.457
Distance from MCL	0.019	0.173	-0.008	0.274	0.000	0.952	-0.001	0.029	0.000	0.844	-0.001	0.039
Distance from soma	0.022	0.156	-0.007	0.293	0.000	0.806	0.003	0.043	0.000	0.763	-0.002	0.048
# of different branches	0.310	<0.001	1.713	0.993	0.045	0.186	-0.846	0.260	0.000	0.914	0.035	0.032
# of preceding bifurcations	0.000	0.988	0.004	0.026	0.000	0.329	-0.514	0.160	0.000	0.366	0.259	0.144
spine neck length	0.030	0.120	-0.510	0.343	0.148	0.053	1.521	0.493	#: 0.000	0.355	0.361	0.149
Diameter of proximal dendrite	#: 0.000	0.895	-0.058	0.034	#: 0.017	0.266	0.864	0.196	#: 0.037	0.140	0.597	0.313
Distance 1st branchpoint from MCL	#: 0.000	0.923	0.001	0.031	#: 0.000	0.565	-0.010	0.080	#: 0.073	0.070	-0.013	0.443
Distance 1st branchpoint from soma	#: 0.000	0.462	-0.005	0.110	#: 0.000	0.828	0.003	0.040	#: 0.046	0.122	-0.009	0.339
Single spine uEPSP amplitude	#: 0.000	0.718	0.172	0.055	#: 0.074	0.130	-1.683	0.326	#: 0.000	0.406	-0.333	0.128

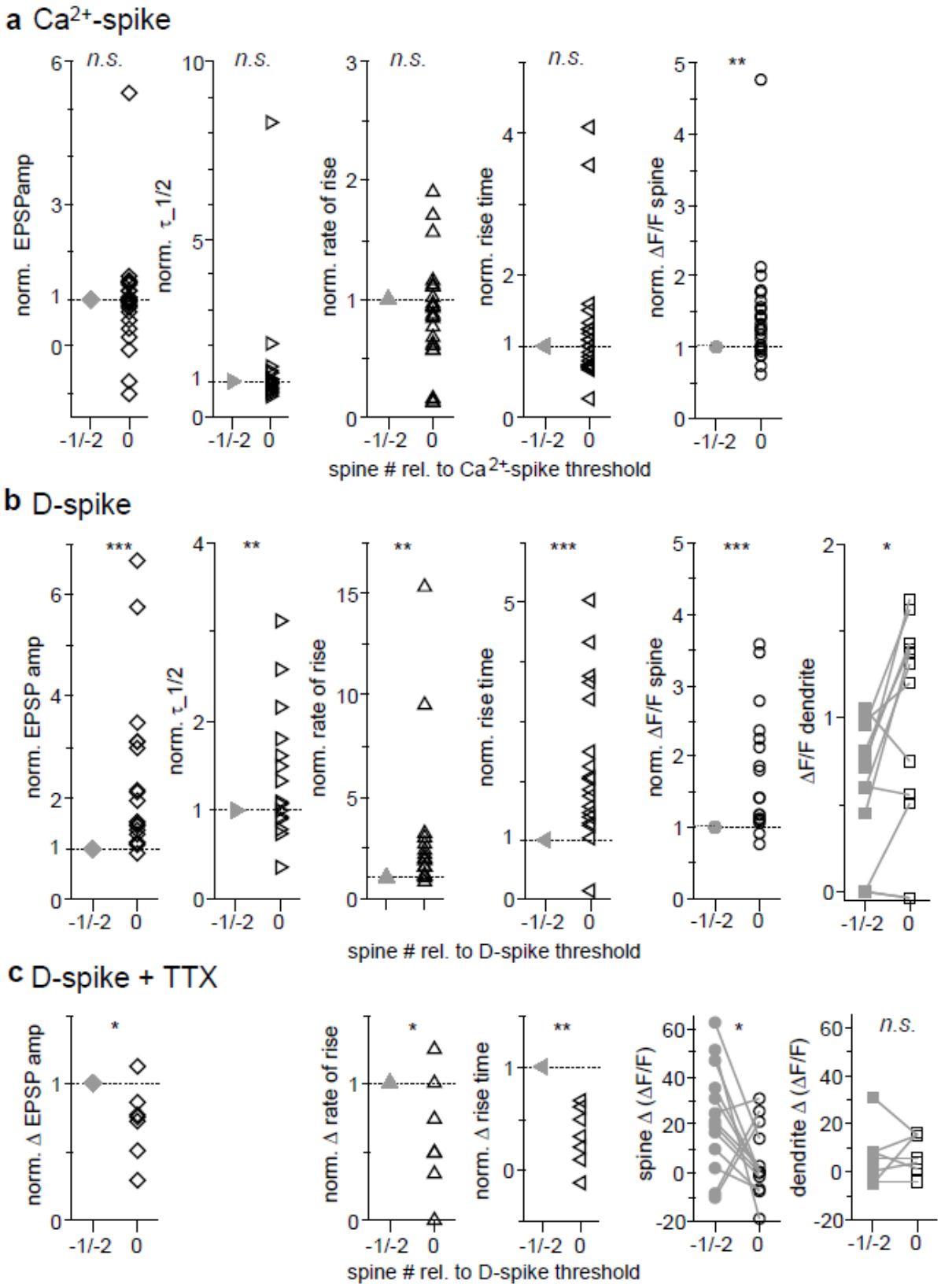

Fig S4. ***Individual data sets at threshold for Ca²⁺-spike and D-spike***

*Individual data points from paired data comparisons across threshold for Ca^{2+}-spikes (**a**), D-spikes (**b**) and effect of TTX on D-spike transitions (**c**). These data were not plotted in the main figures for sake of clarity. In **a**, **b** data are shown normalized to the average value below threshold (except for ΔF/F dendrite because of several points with value zero) and corrected for linear trend in subthreshold data (see 3.3.7). In **c**, changes Δ in parameter values across threshold in TTX are shown normalized to their increase Δ in control, thus no correction for linear trends is required. Analysis of half duration is missing because there were not enough data points for statistical analysis.*

4 General Discussion

This section aims to put the two publications (section *2* and *3*) into context. Since we were limited in the number of words, especially for publication B, this section is also intended to discuss the results of my thesis in more detail. For reasons of clarity and to give a complete picture, some passages of sections *2.5* and *3.5* are repeated.

4.1 Holographic projector

The key question of my study was to determine the precise conditions, including required numbers of activated spines, location and input pattern dependency, underlying the transition from the local spine spike to global signaling. In OB GCs, experimental work together with simulation data predicted that only a high number of tightly temporally synchronized activated spines are able to elicit an AP (Pressler and Strowbridge, 2017). Indeed, in first preliminary experiments on multi-site uncaging in GC dendrites using our commercial 2P galvanometer-based 2D scanning microscope, I did not succeed to stimulate enough spines in one focal plane to elicit global spikes. This was mainly due to the low spine densitiy of GCs (∼1-2 spines per 10 µm, Saghatelyan *et al.*, 2005). The integration of a holographic projector module for synchronous high-resolution 3D multi-site 2P-photostimulation into our existing system solved these problems. It allowed us to activate spines in 3D and to activate fast Na^+ conductances without any loss due to temporal summation (already at 10 successively stimulated spines an uncaging pulse of 0.5 – 1.5 ms would lead to a delay of >5 ms between the first and last stimulus). Simultaneous activation of GC spines is physiological, since MC firing is precisely locked to the sniff phase facilitating ensemble synchronous firing within down to 1 ms and typically prolonged clustered discharges of MCs further increase the possibility for highly synchronous input to GCs (Shusterman *et al.*, 2011). An additional advantage of multi-site 2P uncaging is that we could study the effect of pharmacological agents on dendritic integration without interfering with the input from the MC/TC presynapse, making it certain to study direct intrinsic effects in GCs. However, the current setup showed two bottlenecks: a limited number of stimulation spots and a restricted VOI size (Fig 7d-f). In holographic photostimulation, the laser beam is divided into several beams and the relay onto the SLM causes power loss. The available laser power (4 W)

limited the possible maximum stimulation spots to 12 (if the dendrite was located just below the slice surface). Thus, a stronger 2P laser could increase the number of possible stimulation spots. Beam fall-off at the relay lenses at high positioning ranges underlies the limited VOI. Therefore, the VOI size could be improved by using larger diameter lenses.

The detailed protocol together with proof of principal multi-site uncaging experiments in well-researched cortical PCs can serve as template for other laboratories to integrate this powerful tool to study synaptic integration into existing systems.

4.2 High excitability of granule cell distal apical dendrites

We provide precise numbers of inputs necessary to elicit spiking in a releasing interneuron for the first time. Already at rather low numbers of coactivated dendrodendritic inputs, GC dendrites can generate Ca^{2+}- (5.5 ± 2.1), D-spikes (6.5 ± 2.7) and global APs (≥ 9.0 ± 1.6, Fig 11 c, 12 c). Thus, although GC resting potentials are hyperpolarized compared to e.g. cortical PCs by approximately -10 mV, we find their AP threshold potential to require similar numbers of simultaneously activated spines using the very same holographic experiment (10 ± 1, Fig 8). This high excitability contradicts the hypothesis of Pressler and Strowbridge (2017) that at least ∼25 MC/TC inputs to GCs within a millisecond time course would be necessary to depolarize GCs to AP threshold, making GC firing without concurrent (more efficient) proximal input from other brain regions highly unlikely. We, on the contrary, show that the full set of computations governed by the GCs can be intrinsically triggered by the OB network via distal MC/TC dendrodendritic input without input from higher brain centers or axon collaterals to the proximal dendritic segment. We could also record D-spikes and distinct spikelets for the first time in rat OB GCs, which further underscores the impact of distal inputs. Of note, Price and Powell (1970a) showed axon collaterals from ipsilateral AON upon distal spines in GCs. Thus, it cannot be ruled out that uncaging at distal spines, at least partially, also mimics collateral input. Localized D-spikes indicate multiple initiation zones as suggested earlier by Pinato and Midtgaard (2005) rather than a single proximal initiation zone as suggested by Pressler and Strowbridge (2019). With 1.4 ± 0.8 mV, the average single spine uEPSP size of spiking cells was rather small in our experiments compared to earlier studies (1.8 mV in Pressler and Strowbridge, 2017; 3.2 ± 3.3 mV in Bywalez *et al.*, 2015) excluding excessive photostimulation as cause for low threshold spine numbers. As

note of caution, DNI has inherent interferences with $GABA_A$ receptor activation what, together with dissociated free glutamate, could possibly lead to a higher excitability of the cell (Bywalez *et al.*, 2015; Lage-Rupprecht *et al.*, 2019).

With an average somatic distance of 13.8 ± 12.3 µm from the MCL, the GCs of this study were most likely of type-III that preferentially synapse on TC lateral dendrites (Nagayama *et al.*, 2014). sGCs have been shown to be more excitable and easier to fire APs than dGCs *in vitro* and *in vivo* and are more likely to fire an AP upon stimulation of a single glomerulus. This greater excitability is at least to some extend intrinsic as they have a lower AP threshold and show greater excitability to somatic step current injections. This enables sGCs to mediate lateral inhibition of TCs already at low TC firing rates (Geramita *et al.*, 2016; Wellis and Scott, 1990). Different GC sub-populations could explain the discrepancy to the recent findings of Strowbridge and colleagues. Pressler and Strowbridge (2017) use only GC-MC pairs. Pressler and Strowbridge (2019) use GCs with an average distance of >120 µm from the MCL, thus, most likely belonging to the dGCs. A subsequent experiment easy to conduct would be the comparison of proximal vs distal excitability of GCs by repeating my stimulation paradigm to proximal spines in the MCL or to mix proximal and distal input. To take this even further, uncaging of GABA would allow bimodal control of membrane potential to additionally investigate the interaction between excitation and inhibition in GC dendritic integration (Kantevari *et al.*, 2010).

The low AP threshold of on average -60.2 ± 8.8 mV (Fig 11c) is substantially below the activation threshold of Na_vs (>-45 mV). This indicates either that the AP initiation zone is distant from the soma or the AP threshold is lowered by other active conductances. A possible candidate could be L-type Ca_vs with an activation threshold of >-60 mV (Stuart *et al.*, 2016). As described above, our experimental set-up limited the possible maximum spine number to 12. Under these given experimental conditions, I succeeded to elicit APs in 35 out of 111 cells. This raises the possibility that our data represent a subset of highly excitable GCs, or GCs stimulated at highly excitable spines or parts of the dendrite. Nevertheless, the spine number reported here represents the lower limit for AP generation in GCs. For practical reasons I did not systematically record and analyze all “non-spiking” GCs but 29 were analyzed and showed significant differences to “spiking” GCs in single spine uEPSP amplitude (0.8 ± 0.4 vs 1.4 ± 0.7 mV, p=0.001), and distance

from the MCL (112.8 ± 56.3 vs 64.5 ± 48.7, p=0.004). This preliminary data imply the possibility of functional or methodical differences between the two groups of GCs: input location and intrinsic excitability might be different but also photostimulation strength might have varied due to e.g. stronger scattering tissue above the spine set, though single spine ΔCa^{2+} were similar.

The low threshold spine number matches the findings that GCs can fire APs upon activation of a single glomerulus (Burton and Urban, 2015; Schoppa *et al.*, 1998; Egger, 2008; Geramita *et al.*, 2016). In rodents ~10-20 projection neurons synapse into a single glomerulus, with a slight lower share of TCs (Panhuber *et al.*, 1985; Liu *et al.*, 2016a; Royet *et al.*, 1998). The release probability at these inputs is ~0.5 (Egger *et al.*, 2005). Thus, a given GC is unlikely to fire solely from uniglomerular dendrodendritic inputs but requires additional activation most likely originating from MC/TC axonal collaterals (Schoppa 2006a). However, even though input patterns of this study most likely represent input from more than one glomerular column, uniglomerular inputs - if clustered - might suffice to elicit local Ca^{2+}-spikes, and MC and TC theta bursts, both observed *in vivo* (Fukunaga et al. 2012), could also trigger firing of intracolumnar GCs.

Most GCs in our study showed supralinear integration suggesting active conductances, especially Na_vs, Ca_vs and NMDARs as cause for their high spike generation efficacy.

4.3 Dendritic spiking: D-spike and localized Ca^{2+}-spike

A substantial presence of dendritic Na_vs in GCs was already indicated by reliable AP backpropagation (Egger *et al.*, 2003) and recently, 3D-immunohistochemistry in mice demonstrated clustered Na_v expression throughout the cell surface (Nunes and Kuner, 2018). Na^+ spikelets probably emerged here due to the clustered stimulation at these dendritic Na_v hot spots. We detected D-spikes in about 2/3 of GCs by either distinct spikelets measurable at the soma or, if these were masked by electrotonic filtering, by several lines of evidence: significant discontinuous step-like increases in the sO/I relationship, cuEPSP rate of rise, rise time, decay time, and ΔCa^{2+} in the spine and dendrite (Fig 12d, 13d, f). Increased EPSP rate of rise and Ca^{2+} signal have been shown to be indicators for dendritic spikes in CA1 PCs, as well as in mouse and frog GCs (Losonczy and Magee, 2006; Burton and Urban, 2015; Zelles *et al.*, 2006). We observed a maximal rate of rise of on average 1.7 ± 1.7 V/s associated with D-spikes, exceeding the criteria of Burton and Urban (2015) for spikelets in mouse GCs (0.6 V/s). The increase in rise time by

almost 10 ms can be explained by a substantial latency of spikelets of ~10-20 ms after TPU onset. If the spikelet was masked by electrotonic attenuation, latency could not be determined precisely. An approximation by means of the latency of the maximal cuEPSP rate of rise after TPU onset resulted in a latency of at least 4 ms. This delay indicates that D-spikes are not spine spikes invading the dendrite, which is further supported by the lack of a correlation between spatial clustering and D-spike or Na^+-spike threshold spine numbers (Fig 16c, Tab 1). The delay is also a condition that enables the substantial additional Ca^{2+} influx into the spine in the first place. In the case of perfect coincidence underlying conductances of the spine spike, in particular Na_vs and Ca_vs, would be inactivated preventing additional activation by the D-spike. We showed, using a compartmental GC model and experimental evidence, that a local spine spike and a global, somatically evoked AP coinciding in Hebbian sequence within ~6 ms result in sublinear summation efficiency (SE) of spine Ca^{2+} entry (Aghvami *et al.*, 2019). If I assume the respective Ca^{2+} influx of equal size, we found an increase in spine ΔF/F that would correspond to slightly sublinear SE of the Na^+ spine spike and the D-spike (0.75 ± 0.42, one-sample t-test against SE = 1.00: p=0.024, n=18). Since even full-blown AP signals alone have been shown to mediate a slightly smaller Ca^{2+} influx than spine spikes in Aghvami *et al.* (2019), the SE we observed for the D-spike is probably linear. Thus, our results match both the simulation and experimental findings on SE of spine spike and global AP. Conversely, this means that the summation of spine and D-spike has similar mechanisms to the summation of spine spike and AP. This would also explain the, compared to older findings, disproportionate additional increase of ΔCa^{2+} by ~200 % mediated by the global AP, as this reflects the summation of spine spike, D-spike and global AP that excite the spine in intervals (see also Fig 17). Additionally, the yet longer latency of APs (41 ± 40 ms) matches the latency leading to maximal coincidence detection (40-60 ms, SE value 1.22) in Aghvami *et al.* (2019). In general, it should be noted that the Ca^{2+} dye OGB-1 provides a substantial added Ca^{2+} buffer capacity, disrupting the endogenous Ca^{2+} dynamics and thereby also effecting summation (Egger and Stroh, 2009). In Aghvami *et al.* (2019), we predict the actual dynamic range of free Ca^{2+} levels following local and global activity without buffering to be substantially larger, leading to both more pronounced supra- and sublinearity.

It is known that fast dendritic signals are attenuated and filtered more (Stuart *et al.*, 2016) and D-spikes reportedly mainly influence the kinetics but not the amplitude of the somatic EPSP (Losonczy and Magee, 2006). This could explain why TTX slows the fast cuEPSP component, but just slightly decreases its amplitude (Fig 12g, Fig 14b). On the other hand, blocking of the slow NMDA-mediated component, which is filtered much less both by the spine neck and then along the dendritic tree, strongly reduced cuEPSP amplitude (Fig 14f) but did not influence the fast component of the cuEPSP (no interaction effect on max. rate of rise (spine # x APV): $F_{(5,95)}$=1.616, p=0.182; APV effect: $F_{(1,95)}$=2.261, p=0.176, n=8 GCs). On a speculative note, blocking of Na_vs should increase the membrane resistance and decrease spontaneous network activity mediating local dendritic V_m depolarizations that reduce the driving force (see *1.2.4*). Both would counteract TTX effects on EPSP amplitudes.

Interestingly, in the subset of GCs not showing supralinear integration, the average somatic single spine uEPSP amplitude was significantly larger (2.08 ± 0.64 vs 1.14 ± 0.57 mV, p<0.001) and faster (max. rate of rise: 0.63 ± 0.28 vs 0.35 ± 0.16 V/s, p=0.004). This phenomenon persists, at least as a trend, until the subthreshold activation of 4 spines (cuEPSP amplitude: 6.99 ± 3.67 vs 5.14 ± 2.78 mV, p=0.169; rate of rise: 1.54 ± 0.87 vs 0.78 ± 0.49 V/s, p=0.037). Both indicate less electrotonic filtering, i.e. less electrical isolation of the input site from the soma. I speculate that these differences in electrical isolation, at least partially, explain why 1/3 of GCs did not show D-spikes. Since in axonless GCs the D-spike and global AP are both dendritic Na^+-spikes, somatic recordings show a D-spike/spikelet or a full blown AP dependent on the electrical isolation of the soma from the initiation zone of the Na^+-spike. Therefore, for less electrically isolated input sites, generation of a dendritic Na^+-spike might be directly detected as full-blown AP at the soma, while Na^+-spikes from more isolated input sites attenuate and result in a somatic spikelet. Conversely, this means that D-spike and global AP, as recorded at the soma, are not necessarily different signals. Taken further, the sI/O relationship does not reliably indicate dendritic integration at the actual input site, as it is calculated using single spine uEPSP amplitude and is greatly influenced by electrotonic filtering. Especially in axonless and dendritically releasing neurons, somatic recordings are indicators of but cannot fully reflect, what is actually happening in the dendrite.

All GCs in our sample featured low-threshold Ca^{2+}-spikes elicited on average >1 spine more below AP threshold compared to D-spikes (~3.5 vs ~2.4 spines below AP threshold, Fig 12c). Ca^{2+}-spikes were not accompanied by an increase in the sI/O relationship or by any discontinuous steps in cuEPSP amplitude or kinetics. At threshold, we observed the dendritic Ca^{2+} signal to be rather localized and to decrease to zero with distance from the stimulation site and approximation to the soma (Fig. 11b).

Ca_v densities are apparently lower in the proximal apical dendrite and smaller dendritic Ca^{2+} signals with approximation to the soma are consistent with earlier experiments using somatic current injections to elicit APs (Egger *et al.*, 2003). However, synaptically evoked Ca^{2+}-spikes by electrical stimulation of glomeruli have been shown to invade the whole dendritic tree in an all-or-none fashion and their main initiation zone was probably not located in the distal apical dendritic tree (Pressler and Strowbridge, 2019; Egger *et al.*, 2005). The localized Ca^{2+}-spike observed here, on the other hand, is independent from input location and probably emerged due to rather dense input compared to global input all along the dendritic tree upon glomerular stimulation. Activation of rather densely packed spines is most likely also the cause for activation of HVACC and therefore lower contribution of T-type Ca_vs compared to earlier studies (~ 74 vs <20% of control in both spine and dendrite, Fig 15d; Egger *et al.*, 2005). Additionally, the localized Ca^{2+}-spike is highly NMDAR-dependent (see below). Compared to the single spine spike, additional Ca^{2+} influx into the spine caused by either LTS or AP, was described as being linear and supralinear, respectively (Egger, 2008; Pinato and Midtgaard, 2005; Egger *et al.*, 2005). Again, considering both local spine spike and Ca^{2+}-spike-mediated signals to be similar in size (Egger *et al.*, 2005) we observed highly sublinear additional Ca^{2+} influx by ~57 % caused by the Ca^{2+}-spike (Fig 13c). LTS data upon glomerular stimulation in Egger *et al.* (2005) possibly also included dendritic Na^{+}-spikes, not identifiable at the soma. Indeed, as described above the generation of a D-spike mediated an additional Ca^{2+} influx close to linear summation and activation of additional spines above Ca^{2+}-spike threshold, possibly eliciting D-spikes, also caused a more globally spreading Ca^{2+} signal in our experiments (Fig 11b).

I conclude that in contrast to a global LTS upon distributed input, input to rather densely packed spines might indeed be a substrate for local lateral inhibition as suggested earlier (Woolf *et al.*,

1991a; Woolf and Greer, 1994; Isaacson and Strowbridge, 1998). The D-spike adds another level of GC activation, which is stronger and more global than the Ca^{2+}-spike but still more localized than the AP (see also Fig 17). Thus, GCs display multiple levels of compartmentalization.

4.4 Morphology and input location influence non-local spike generation only subtly

The location of the input site, with respect to soma or MCL, did not influence spike generation, further pointing towards multiple initiation sites and high excitability of the whole dendritic tree (Fig 16a, Tab 1). Input distribution together with the distribution of the spine set across different branches influenced Ca^{2+}-spike generation substantially (multiple regression analysis: r^2=0.416, $p<0.001$, Fig 16 c, d). This is in line with textbook knowledge, that subthreshold passive potentials are strongly attenuated especially by dendritic branching and that clustered input is more likely to recruit active conductances (Tran-Van-Minh *et al.*, 2015). The Ca^{2+}-spike can reduce passive attenuation and precedes the D-spike and AP. Its space constant of ≥ 60 µm is greater than the maximum distribution of spines in our experiments. Together with a high Na_v excitability of the whole dendrite, this could explain the independence of D-spike and AP generation from input distribution. The limitation of our system to 70x70x70 μm^3 (Fig 7e) did not allow us to investigate farther distributed inputs. Thus, the distribution limit of inputs to successfully generate APs remain to be elucidated. The independence from spine neck length is consistent with earlier findings in single spine activation (Bywalez *et al.*, 2015). Ona-Jodar *et al.* (2017) found varying Na^+ transients, putatively due to different Na_v densities with distance from soma, in subtypes of GCs separable by the diameter of their proximal dendrite and the distance of their 1st branchpoint from MCL. In this study, we could not find any influence of these parameters on Na^+-spike generation.

4.5 NMDA-spikes and role of NMDARs in granule cell synaptic processing

Blockade of NMDARs abolished the Ca^{2+}-spike and had stronger effects on supralinear integration in GCs than blockade of Na_vs or Ca_vs. This higher efficiency is probably related to the slower kinetics of the NMDAR component compared to Na_v- or Ca_v- mediated currents, as discussed above. Strong impact of NMDARs on GC dendritic integration together with EPSP decay times > 50 ms recorded in most GCs is typical for NMDA-spikes (Maccaferri and Dingledine, 2002; Antic

et al., 2010). In one particular GC we stochastically observed distinctive somatic NMDA plateau potentials lasting for up to 500 ms. In the event of a NMDA spike, cuEPSP amplitude was doubled and spine as well as dendritic ΔF/F was roughly tripled. Thus, even though NMDARs are only located in the electrically and chemically isolated spine head, NMDA-spikes are closely intertwined with dendritic Ca^{2+}- and Na^{+}-spike generation. We observed a substantially higher NMDAR contribution to Ca^{2+}-spike generation compared to earlier studies (25 µM D-APV, dendrite ΔF/F: 14 ± 15 (8 activated spines) vs 58 ± 12 % of control, Fig 14h; Egger *et al.*, 2005). Again, more closely packed spines could lead to a more efficient NMDAR activation together with activation of HVACCs, as described above. This interaction of HVACCs with NMDARs leading to a boost of dendritic Ca^{2+} influx has already been demonstrated upon near-synchronous stimulation of groups of synapses in CA1 pyramidal neurons (Losonczy and Magee, 2006; VanDongen, 2009). LTS upon glomerular stimulation in Egger *et al.* (2005) potentially also involved proximal input by MC/TC axon collaterals masking the NMDA-dependence of distal dendrodendritic input (Schoppa, 2006a). Another explanation could be a stronger activation of extrasynaptic NMDA autoreceptors present on MC dendrites caused by glutamate uncaging (Isaacson, 1999). Reportedly, TPU results in a slightly larger NMDAR-mediated component of the postsynaptic Ca^{2+} signal than true synaptic activation via glomerular stimulation (to ~ 50 % vs ~ 65 % of control; Bywalez *et al.*, 2015; Egger *et al.*, 2005). Additionally, the integration of the SLM into the uncaging laser beam caused an increase of the axial point spread function from 1.1 to 2.67 µm (Fig 7c). This could lead to an even more widespread activation of extrasynaptic NMDARs. However, we observed similar D-APV effects in single spine activation compared to glutamate uncaging in the same system but without the use of a SLM by Bywalez *et al.* (2015): 37 ± 17 % vs 41 ± 57 % of control, whereby the high standard deviation is attributable to two D-APV insensitive spines (Balu *et al.*, 2007). Substantial variance in NMDAR contribution across synapses has already been described in previous Ca^{2+} imaging studies (Aghvami *et al.*, 2019; Bywalez *et al.*, 2015; Egger *et al.*, 2005). Intriguingly, unitary GABA release from the GC spine is also highly NMDAR-dependent (Lage-Rupprecht *et al.*, 2019), supralinear summation at positive Hebbian pairing intervals is carried by NMDARs (see above, Aghvami *et al.*, 2019) and NMDARs are known to mediate synaptic plasticity (Chatterjee *et al.*, 2016; Neant-Fery *et al.*, 2012).

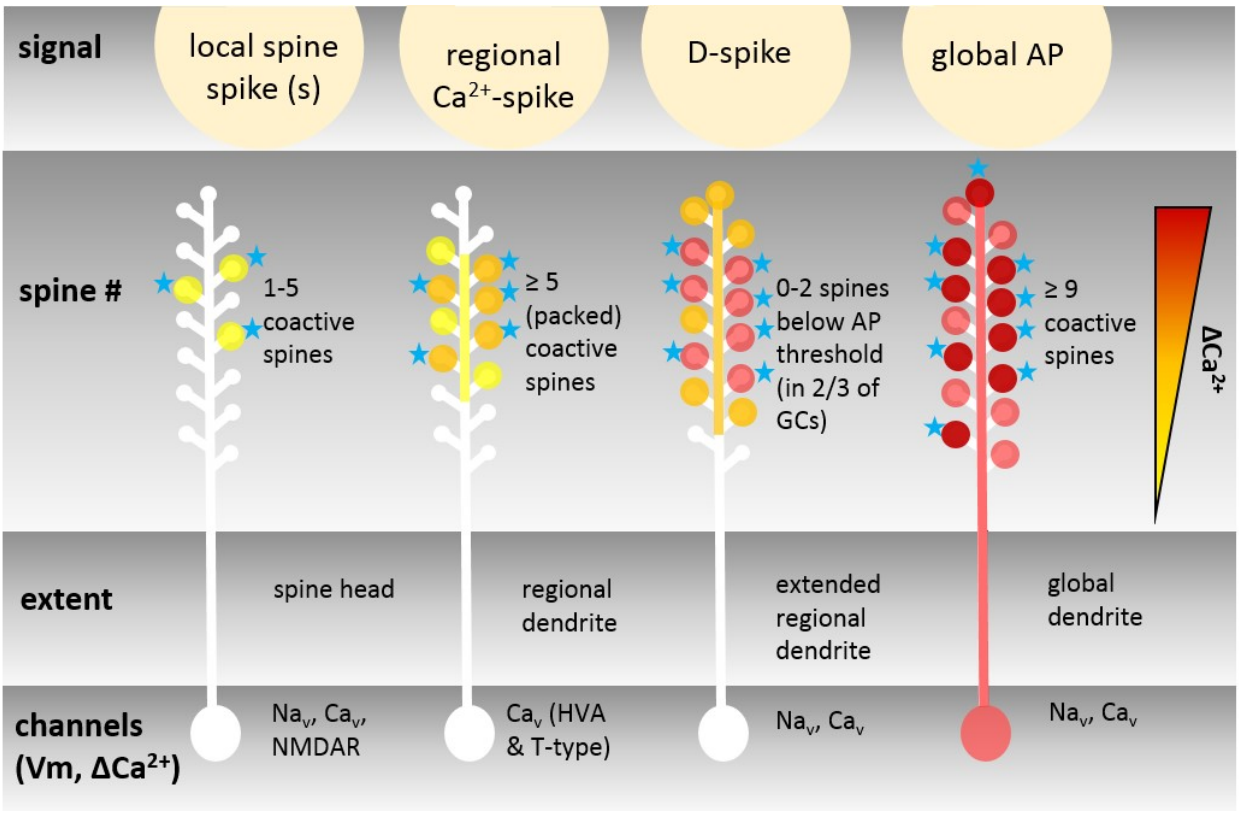

Fig 17. ***Summary of GC dendritic spikes mediating substantial additional Ca^{2+} influxes into the spine.*** *Activation of a single spine leads to a Na^+ spine spike restricted to the spine head. ≥5 coactive spines elicit a regional T-type- and HVA Ca_v mediated Ca^{2+}-spike with Ca^{2+} influx into the dendrite and additional Ca^{2+} influx into spines. Coactivation of >6 spines elicits a regional dendritic Na^+-spike (D-spike) mediating further increase of dendrite and spine ΔCa^{2+}. Activation of ≥9 spines leads to the generation of a global AP that invades the whole cell mediating further Ca^{2+} influx. Successive increase of spine ΔCa^{2+} in increments with generation of each spike, putatively determines the degree of GABA release and thereby the onset and degree of lateral inhibition. Note the interaction of local input and global signals, the influx of Ca^{2+} into non-activated spines, and the increasing globality of the dendritic spikes. Channels indicate active conductances that primarily mediate the generation of the spike. Note that conductances of preceding spikes (especially for spine spikes in activated spines) are still activated and involved in reaching following spike thresholds and Ca^{2+} influx is always heavily NMDAR dependent. Dendrites are displayed without branches for simplification. Stars represent uncaging spots/synaptic input. Na_v: voltage-gated sodium channel, Ca_v: voltage-gated calcium channel, HVA: high-voltage-activated, NMDAR: N-methyl-D-aspartate receptor.*

In conclusion, NMDARs are essentially involved in all aspects of GC reciprocal synaptic processing and dendritic integration.

4.6 Functional Implications

We show that (superficial) GCs can fire APs by relatively low numbers of non-proximal dendrodendritic inputs independent from centrifugal inputs, implicating that they can generate rapid (maximal) GABAergic output and therewith lateral inhibition.

Fast gamma oscillations in the OB are associated with the successful discrimination of closely related odors (Kay *et al.*, 2009), are mediated by the GC MC/TC reciprocal synapse and arise the need for a fast excitatory-inhibitory feedback loop (Pouille *et al.*, 2017; Fukunaga *et al.*, 2014). Localized D-spikes could be a source of fast lateral output as they have shorter latencies than global (bp)APs (see above). In fact, upon observing D-spikes in frog GCs, Zelles *et al.* (2006) proposed interaction of D-spikes and bpAPs, or even trains of D-spikes, at intervals as short as 5-6 ms (150 - 200Hz) circumventing long interspike intervals of somatic APs. Pinato and Midtgaard (2005) could elicit spikelets at a frequency of 150-250 Hz in frog GCs, while stronger current injections could evoke only much lower maximal frequencies of APs (10-30 Hz). Gamma frequency has been shown to be exerted by the GC reciprocal synapse but did not require somatic APs in GCs (Lagier *et al.*, 2004; see also Schoppa, 2006b). So, while GCs display only sparse, long latency AP firing *in vivo* (Cang and Isaacson, 2003; Kato *et al.*, 2012), spikelets have been frequently observed (Wellis and Scott, 1990; Labarrera *et al.*, 2013; Mori and Takagi, 1978; Luo and Katz, 2001) and could serve as basis for fast inhibitory release necessary for the generation of gamma oscillations. Also *in vitro* Burton and Urban (2015) show that GCs spontaneously fire spikelets more frequently than APs. Notably, fast signaling is of particular importance for sGCs, as TCs have shorter latencies and carry faster gamma oscillations than MCs (Manabe and Mori, 2013). Dendritic spikes are associated with oscillations in various other brain regions. For example, the LTS has been shown to be involved in sleep-related slow oscillations (Contreras and Steriade, 1996; Connelly *et al.*, 2015). Fast dendritic Na^+-spikes are strongly associated with sharp wave-associated ripples (120-200 Hz) in CA1 PCs (Klausberger *et al.*, 2004; Kamondi *et al.*, 1998; Memmesheimer, 2010). *In vivo* somatic and dendritic recordings by Kamondi *et al.* (1998) revealed dendritic Na^+-spikes at higher frequencies than APs at the soma. Moreover, the dendritic interspike intervals were shorter than expected based on AP refractoriness of CA1 PCs. They hypothesize that spikes may be generated at other dendritic locations while one dendritic

spike initiation zone is refractory. On the basis of these findings, Memmesheimer (2010) describe a model, where fast sharp wave-associated oscillations are generated by fast nonlinear dendritic Na^+-spikes. I hypothesize that D-spikes in GC dendrites could be involved in the generation and synchronization of gamma oscillations in the OB in a similar way.

Local activation of the single GC spine results in rather low release probability of on average < 0.3 (Lage-Rupprecht *et al.*, 2019). The observed stepwise increase in spine ΔCa^{2+} at the three dendritic spike thresholds putatively mediates increasingly higher GABA release probabilities. It is tempting to speculate that different spike identities encode for different odor information, enabling multiplexing. Intriguingly, multiplexing of odor information was already described for MCs in zebrafish, where wave-like, most likely GC-mediated, gamma oscillations and tightly phase-locked spiking encodes for odor category and odor identity, respectively (Friedrich *et al.*, 2004). The changes in GC spine and dendrite ΔCa^{2+} independent from somatic V_m amplitude (both for the localized Ca^{2+}-spike and the attenuated D-spike, Fig 11-13) also allow for multiplexed signals as proposed for cerebellar GCs (Tran-Van-Minh *et al.*, 2016), which in OB GCs might implement e.g. independent plasticity induction across reciprocal spines (Chatterjee *et al.*, 2016). It remains to be elucidated whether different local and global activation modes directly influence GC dendritic release. Of note, reciprocal GABAergic release from somatically stimulated GCs onto MC/TCs has never been directly proven (Burton, 2017). Dual patch-clamp recordings of GCs and MC/TCs together with multi-site uncaging at GCs could give direct proof, whether different modes of GC activation mediate different levels of self and lateral inhibition between MC/TCs.

5 Abbreviations

µM	Micromolar
µm	Micrometer
µs	Microsecond
1P	One-photon
2D	Two dimensions
2P	Two-photon
2P	Two-photon
3D	Three dimensions
AMPAR	Alpha-amino-3-hydroxy-5-methyl-4-isoazole propionic acid receptor
AON	Anterior olfactory nucleus
AP	Action potential
APC	Anterior piriform cortex
A-type KC	A-type potassium channel
bpAP	Back-propagating action potential
Ca^{2+}	Calcium
Ca_vs	Voltage-gated calcium channels
Cd^{2+}	Cadmium
Cl^-	Chloride
CO_2	Carbon dioxide
Ctrl	Control
cuEPSP	Compound uncaging EPSP
D-APV	D-(2R)-amino-5-phosphonovaleric acid
dGC	Deep granule cell

dSACS	Deep short axon cells
D-spike	Dendritic Na^+-spike
E.g.	For example (exempli gratia)
EPL	External plexiform layer
EPSP	Excitatory postsynaptic potential
ET	External tufted cell
Fig	Figure
FOV	Field of view
fs	Femtosecond
$GABA_AR$	Ionotropic gamma-aminobutyric acid receptor
GC	Granule cell
GCL	Granule cell layer
GL	Glomerular layer
H_2S	Hydrogen sulfide
HVACC	High-voltage-activated calcium channel
Hz	Hertz
I.e.	That is (id est)
IPL	Internal plexiform layer
IR KC	Inward rectifier potassium channel
K^+	Potassium
LOT	Lateral olfactory tract
LTS	Low-threshold calcium-spike
LVACC	Low-voltage-activated calcium channel
MC	Mitral cell
MCL	Mitral cell layer

mM	Millimolar
ms	Millisecond
mV	Millivolt
Na^+	Sodium
Na_v	Voltage-gated sodium channel
NMDAR	N-methyl-$_D$-aspartate receptor
OB	Main olfactory bulb
OC	Olfactory cortex
OE	Olfactory epithelium
ON	Olfactory nerve
ONL	Olfactory nerve layer
OR	Odorant receptor
OSN	Olfactory sensory neuron (also olfactory receptor neuron)
pA	Picoampere
PBS	Polarizing beam splitter
PC	Pyramidal cell
PG	Periglomerular cell
PN	Projection neuron
PPC	Posterior piriform cortex
RMS	Rostral migratory stream
SE	Summation efficiency
sGC	Superficial granule cell
sI/O	Subthreshold input-output relation
sO/I	Subthreshold output-input relation
sSAC	Superficial short axon cell

Tab	Table
TC	Tufted cell
TPU	Two-photon uncaging
TTX	Tetrodotoxin
uEPSP	Uncaging EPSP
V_m	Membrane potential
VOI	Volume of interest
V_{rest}	Resting membrane potential
V-SVZ	Ventricular-subventricular zone of the lateral ventricle
W	Watt

6 References

Abraham, N. M., Egger, V., Shimshek, D. R., Renden, R., Fukunaga, I., Sprengel, R., Seeburg, P. H., Klugmann, M., Margrie, T. W., Schaefer, A. T. and Kuner, T. (2010) Synaptic inhibition in the olfactory bulb accelerates odor discrimination in mice. Neuron, 65, 399-411.

Abraham, N. M., Spors, H., Carleton, A., Margrie, T. W., Kuner, T. and Schaefer, A. T. (2004) Maintaining Accuracy at the Expense of Speed: Stimulus Similarity Defines Odor Discrimination Time in Mice. Neuron, 44, 865-876.

Abrahamsson, T., Cathala, L., Matsui, K., Shigemoto, R. and DiGregorio, D. A. (2012) Thin Dendrites of Cerebellar Interneurons Confer Sublinear Synaptic Integration and a Gradient of Short-Term Plasticity. Neuron, 73, 1159-1172.

Adrian, E. D. (1950) The electrical activity of the mammalian olfactory bulb. Electroencephalogr Clin Neurophysiol, 2, 377-388.

Aghvami, S. S., Muller, M., Araabi, B. N. and Egger, V. (2019) Coincidence Detection within the Excitable Rat Olfactory Bulb Granule Cell Spines. J Neurosci, 39, 584-595.

Ahern, C. A., Payandeh, J., Bosmans, F. and Chanda, B. (2016) The hitchhiker's guide to the voltage-gated sodium channel galaxy. J Gen Physiol, 147, 1-24.

Ai, H., Kumaraswamy, A., Kohashi, T., Ikeno, H. and Wachtler, T. (2018) Inhibitory Pathways for Processing the Temporal Structure of Sensory Signals in the Insect Brain. Frontiers in psychology, 9, 1517-1517.

Alonso, M., Lepousez, G., Wagner, S., Bardy, C., Gabellec, M. M., Torquet, N. and Lledo, P. M. (2012) Activation of adult-born neurons facilitates learning and memory. Nature Neuroscience, 15, 897-U127.

Anselmi, F., Ventalon, C., Bègue, A., Ogden, D. and Emiliani, V. (2011) Three-dimensional imaging and photostimulation by remote-focusing and holographic light patterning. Proceedings of the National Academy of Sciences, 108, 19504-19509.

Antic, S. D., Zhou, W. L., Moore, A. R., Short, S. M. and Ikonomu, K. D. (2010) The decade of the dendritic NMDA spike. Journal of neuroscience research, 88, 2991-3001.

Araneda, R. C., Kini, A. D. and Firestein, S. (2000) The molecular receptive range of an odorant receptor. Nat Neurosci, 3, 1248-1255.

Arevian, A. C., Kapoor, V. and Urban, N. N. (2008) Activity-dependent gating of lateral inhibition in the mouse olfactory bulb. Nature Neuroscience, 11, 80-87.

Ashley, C. C. and Ridgway, E. B. (1968) Simultaneous recording of membrane potential, calcium transient and tension in single muscle fibers. Nature, 219, 1168-1169.

Ballesteros-Yáñez, I., Benavides-Piccione, R., Elston, G. N., Yuste, R. and DeFelipe, J. (2006) Density and morphology of dendritic spines in mouse neocortex. Neuroscience, 138, 403-409.

Balu, R., Pressler, R. T. and Strowbridge, B. W. (2007) Multiple Modes of Synaptic Excitation of Olfactory Bulb Granule Cells. The Journal of Neuroscience, 27, 5621-5632.

Banerjee, A., Marbach, F., Anselmi, F., Koh, Matthew S., Davis, Martin B., Garcia da Silva, P., Delevich, K., Oyibo, Hassana K., Gupta, P., Li, B. and Albeanu, Dinu F. (2015) An Interglomerular Circuit Gates Glomerular Output and Implements Gain Control in the Mouse Olfactory Bulb. Neuron, 87, 193-207.

Berridge, M. J., Lipp, P. and Bootman, M. D. (2000) The versatility and universality of calcium signalling. Nat Rev Mol Cell Biol, 1, 11-21.

Birnbaumer, L. (2009) The TRPC Class of Ion Channels: A Critical Review of Their Roles in Slow, Sustained Increases in Intracellular Ca2+ Concentrations. Annual Review of Pharmacology and Toxicology, 49, 395-426.

Born, M. and Wolf, E. (1980) Principles of optics : electromagnetic theory of propagation, interference and diffraction of light, Pergamon Press, Oxford ; New York.

Boyd, Alison M., Sturgill, James F., Poo, C. and Isaacson, Jeffry S. (2012) Cortical Feedback Control of Olfactory Bulb Circuits. Neuron, 76, 1161-1174.

Branco, T., Clark, B. A. and Häusser, M. (2010) Dendritic Discrimination of Temporal Input Sequences in Cortical Neurons. Science, 329, 1671-1675.

Branco, T. and Hausser, M. (2011) Synaptic integration gradients in single cortical pyramidal cell dendrites. Neuron, 69, 885-892.

Brennan, P. A. and Zufall, F. (2006) Pheromonal communication in vertebrates. Nature, 444, 308-315.

Buck, L. and Axel, R. (1991) A novel multigene family may encode odorant receptors: a molecular basis for odor recognition. Cell, 65, 175-187.

Burnashev, N., Monyer, H., Seeburg, P. H. and Sakmann, B. (1992) Divalent ion permeability of AMPA receptor channels is dominated by the edited form of a single subunit. Neuron, 8, 189-198.

Burton, S. D. (2017) Inhibitory circuits of the mammalian main olfactory bulb. J Neurophysiol, 118, 2034-2051.

Burton, S. D., LaRocca, G., Liu, A., Cheetham, C. E. J. and Urban, N. N. (2017) Olfactory Bulb Deep Short-Axon Cells Mediate Widespread Inhibition of Tufted Cell Apical Dendrites. The Journal of Neuroscience, 37, 1117.

Burton, S. D. and Urban, N. N. (2015) Rapid Feedforward Inhibition and Asynchronous Excitation Regulate Granule Cell Activity in the Mammalian Main Olfactory Bulb. J Neurosci, 35, 14103-14122.

Bushdid, C., Magnasco, M. O., Vosshall, L. B. and Keller, A. (2014) Humans can discriminate more than 1 trillion olfactory stimuli. Science, 343, 1370-1372.

Bywalez, W. G., Ona-Jodar, T., Lukas, M., Ninkovic, J. and Egger, V. (2016) Dendritic Arborization Patterns of Small Juxtaglomerular Cell Subtypes within the Rodent Olfactory Bulb. Front Neuroanat, 10, 127.

Bywalez, W. G., Patirniche, D., Rupprecht, V., Stemmler, M., Herz, A. V., Palfi, D., Rozsa, B. and Egger, V. (2015) Local postsynaptic voltage-gated sodium channel activation in dendritic spines of olfactory bulb granule cells. Neuron, 85, 590-601.

Cai, X., Liang, C. W., Muralidharan, S., Kao, J. P., Tang, C. M. and Thompson, S. M. (2004) Unique roles of SK and Kv4.2 potassium channels in dendritic integration. Neuron, 44, 351-364.

Callaway, E. M. (2005) Structure and function of parallel pathways in the primate early visual system. The Journal of physiology, 566, 13-19.

Cang, J. and Isaacson, J. S. (2003) *In vivo* Whole-Cell Recording of Odor-Evoked Synaptic Transmission in the Rat Olfactory Bulb. The Journal of Neuroscience, 23, 4108-4116.

Cash, S. and Yuste, R. (1999) Linear summation of excitatory inputs by CA1 pyramidal neurons. Neuron, 22, 383-394.

Catterall, W. A. (2000) Structure and regulation of voltage-gated Ca2+ channels. Annu Rev Cell Dev Biol, 16, 521-555.

Chatterjee, M., Perez de Los Cobos Pallares, F., Loebel, A., Lukas, M. and Egger, V. (2016) Sniff-Like Patterned Input Results in Long-Term Plasticity at the Rat Olfactory Bulb Mitral and Tufted Cell to Granule Cell Synapse. Neural Plast, 2016, 9124986.

Chiovini, B., Turi, G. F., Katona, G., Kaszas, A., Palfi, D., Maak, P., Szalay, G., Szabo, M. F., Szabo, G., Szadai, Z., Kali, S. and Rozsa, B. (2014) Dendritic spikes induce ripples in parvalbumin interneurons during hippocampal sharp waves. Neuron, 82, 908-924.

Choy, J. M. C., Sané, S. S., Lee, W. M., Stricker, C., Bachor, H. A. and Daria, V. R. (2017) Improving Focal Photostimulation of Cortical Neurons with Pre-derived Wavefront Correction. Frontiers in Cellular Neuroscience, 11.

Cockerham, R. E., Margolis, F. L. and Munger, S. D. (2009) Afferent activity to necklace glomeruli is dependent on external stimuli. BMC research notes, 2, 31-31.

Connelly, W. M., Crunelli, V. and Errington, A. C. (2015) The Global Spike: Conserved Dendritic Properties Enable Unique Ca2+ Spike Generation in Low-Threshold Spiking Neurons. J Neurosci, 35, 15505-15522.

Contreras, D. and Steriade, M. (1996) Spindle oscillation in cats: the role of corticothalamic feedback in a thalamically generated rhythm. The Journal of Physiology, 490, 159-179.

Crespo, C., Liberia, T., Blasco-Ibáñez, J. M., Nácher, J. and Varea, E. (2013) The Circuits of the Olfactory Bulb. The Exception as a Rule. The Anatomical Record, 296, 1401-1412.

Croy, I. and Hummel, T. (2017) Olfaction as a marker for depression. Journal of Neurology, 264, 631-638.

Curtis, J. E., Koss, B. A. and Grier, D. G. (2002) Dynamic holographic optical tweezers. Optics Communications, 207, 169-175.

Dal Maschio, M., Difato, F., Beltramo, R., Blau, A., Benfenati, F. and Fellin, T. (2010) Simultaneous two-photon imaging and photo-stimulation with structured light illumination. Opt. Express, 18, 18720-18731.

Daria, V. R., Stricker, C., Bowman, R., Redman, S. and Bachor, H.-A. (2009) Arbitrary multisite two-photon excitation in four dimensions. Applied Physics Letters, 95, 093701.

Denk, W., Delaney, K. R., Gelperin, A., Kleinfeld, D., Strowbridge, B. W., Tank, D. W. and Yuste, R. (1994) Anatomical and functional imaging of neurons using 2-photon laser scanning microscopy. J Neurosci Methods, 54, 151-162.

Denk, W., Strickler, J. H. and Webb, W. W. (1990) Two-photon laser scanning fluorescence microscopy. Science, 248, 73-76.

Dewell, R. B. and Gabbiani, F. (2018) Active membrane conductances and morphology of a collision detection neuron broaden its impedance profile and improve membrane synchrony. bioRxiv, 454702.

Dietz, S. B. and Murthy, V. N. (2005) Contrasting short-term plasticity at two sides of the mitral–granule reciprocal synapse in the mammalian olfactory bulb. The Journal of Physiology, 569, 475-488.

Dong, H.-W., Heinbockel, T., Hamilton, K. A., Hayar, A. and Ennis, M. (2009) Metabotropic glutamate receptors and dendrodendritic synapses in the main olfactory bulb. Annals of the New York Academy of Sciences, 1170, 224-238.

Doty, R. L. (2017) Olfactory dysfunction in neurodegenerative diseases: is there a common pathological substrate? The Lancet Neurology, 16, 478-488.

Doty, R. L., Brugger, W. E., Jurs, P. C., Orndorff, M. A., Snyder, P. J. and Lowry, L. D. (1978) Intranasal trigeminal stimulation from odorous volatiles: Psychometric responses from anosmic and normal humans. Physiology & Behavior, 20, 175-185.

Duemani Reddy, G., Kelleher, K., Fink, R. and Saggau, P. (2008) Three-dimensional random access multiphoton microscopy for functional imaging of neuronal activity. Nature Neuroscience, 11, 713-720.

Economo, M. N., Hansen, K. R. and Wachowiak, M. (2016) Control of Mitral/Tufted Cell Output by Selective Inhibition among Olfactory Bulb Glomeruli. Neuron, 91, 397-411.

Egger, V. (2008) Synaptic sodium spikes trigger long-lasting depolarizations and slow calcium entry in rat olfactory bulb granule cells. Eur J Neurosci, 27, 2066-2075.

Egger, V. and Stroh, O. (2009) Calcium buffering in rodent olfactory bulb granule cells and mitral cells. J Physiol, 587, 4467-4479.

Egger, V., Svoboda, K. and Mainen, Z. F. (2003) Mechanisms of lateral inhibition in the olfactory bulb: Efficiency and modulation of spike-evoked calcium influx into granule cells. J Neurosci, 23, 7551-7558.

Egger, V., Svoboda, K. and Mainen, Z. F. (2005) Dendrodendritic synaptic signals in olfactory bulb granule cells: local spine boost and global low-threshold spike. Journal of Neuroscience, 25, 3521-3530.

Egger, V. and Urban, N. N. (2006) Dynamic connectivity in the mitral cell-granule cell microcircuit. Semin Cell Dev Biol, 17, 424-432.

Ellis-Davies, G. C. R. (2007) Caged compounds: photorelease technology for control of cellular chemistry and physiology. Nature Methods, 4, 619-628.

Epsztein, J., Lee, A. K., Chorev, E. and Brecht, M. (2010) Impact of spikelets on hippocampal CA1 pyramidal cell activity during spatial exploration. Science, 327, 474-477.

Eyre, M. D., Antal, M. and Nusser, Z. (2008) Distinct deep short-axon cell subtypes of the main olfactory bulb provide novel intrabulbar and extrabulbar GABAergic connections. J Neurosci, 28, 8217-8229.

Eyre, M. D., Kerti, K. and Nusser, Z. (2009) Molecular diversity of deep short-axon cells of the rat main olfactory bulb. Eur J Neurosci, 29, 1397-1407.

Fan, G. Y., Fujisaki, H., Miyawaki, A., Tsay, R. K., Tsien, R. Y. and Ellisman, M. H. (1999) Video-rate scanning two-photon excitation fluorescence microscopy and ratio imaging with cameleons. Biophys J, 76, 2412-2420.

Fisher, J. A. and Salzberg, B. M. (2015) Two-Photon Excitation of Fluorescent Voltage-Sensitive Dyes: Monitoring Membrane Potential in the Infrared. Adv Exp Med Biol, 859, 427-453.

Fox, D. M., Tseng, H. A., Smolinski, T. G., Rotstein, H. G. and Nadim, F. (2017) Mechanisms of generation of membrane potential resonance in a neuron with multiple resonant ionic currents. PLoS Comput Biol, 13, e1005565.

Friedrich, R. W., Habermann, C. J. and Laurent, G. (2004) Multiplexing using synchrony in the zebrafish olfactory bulb. Nature Neuroscience, 7, 862-871.

Fukunaga, I., Berning, M., Kollo, M., Schmaltz, A. and Schaefer, A. T. (2012) Two distinct channels of olfactory bulb output. Neuron, 75, 320-329.

Fukunaga, I., Herb, J. T., Kollo, M., Boyden, E. S. and Schaefer, A. T. (2014) Independent control of gamma and theta activity by distinct interneuron networks in the olfactory bulb. Nat Neurosci, 17, 1208-1216.

Gabor, D. (1948) A New Microscopic Principle. Nature, 161, 777-778.

Galizia, C. G. and Lledo, P.-M. (2013) Neurosciences : from molecule to behavior : a university textbook, Springer Spektrum, Heidelberg ; New York.

Geramita, M. and Urban, N. N. (2017) Differences in Glomerular-Layer-Mediated Feedforward Inhibition onto Mitral and Tufted Cells Lead to Distinct Modes of Intensity Coding. J Neurosci, 37, 1428-1438.

Geramita, M. A., Burton, S. D. and Urban, N. N. (2016) Distinct lateral inhibitory circuits drive parallel processing of sensory information in the mammalian olfactory bulb. Elife, 5.

Gibbs, R. A., Weinstock, G. M., Metzker, M. L., Muzny, D. M., Sodergren, E. J., Scherer, S., Scott, G., Steffen, D., Worley, K. C., Burch, P. E., Okwuonu, G., Hines, S., Lewis, L., DeRamo, C., Delgado, O., Dugan-Rocha, S., Miner, G., Morgan, M., Hawes, A., Gill, R., Celera, Holt, R. A., Adams, M. D., Amanatides, P. G., Baden-Tillson, H., Barnstead, M., Chin, S., Evans, C. A., Ferriera, S., Fosler, C., Glodek, A., Gu, Z., Jennings, D., Kraft, C. L., Nguyen, T., Pfannkoch, C. M., Sitter, C., Sutton, G. G., Venter, J. C., Woodage, T., Smith, D., Lee, H. M., Gustafson, E., Cahill, P., Kana, A., Doucette-Stamm, L., Weinstock, K., Fechtel, K., Weiss, R. B., Dunn, D. M., Green, E. D., Blakesley, R. W., Bouffard, G. G., De Jong, P. J., Osoegawa, K., Zhu, B., Marra, M., Schein, J., Bosdet, I., Fjell, C., Jones, S., Krzywinski, M., Mathewson, C., Siddiqui, A., Wye, N., McPherson, J., Zhao, S., Fraser, C. M., Shetty, J., Shatsman, S., Geer, K., Chen, Y., Abramzon, S., Nierman, W. C., Havlak, P. H., Chen, R., Durbin, K. J., Egan, A., Ren, Y., Song, X. Z., Li, B., Liu, Y., Qin, X., Cawley, S., Worley, K. C., Cooney, A. J., D'Souza, L. M., Martin, K., Wu, J. Q., Gonzalez-Garay, M. L., Jackson, A. R., Kalafus, K. J., McLeod, M. P., Milosavljevic, A., Virk, D., Volkov, A., Wheeler, D. A., Zhang, Z., Bailey, J. A., Eichler, E. E., et al.

(2004) Genome sequence of the Brown Norway rat yields insights into mammalian evolution. Nature, 428, 493-521.

Gire, D. H., Franks, K. M., Zak, J. D., Tanaka, K. F., Whitesell, J. D., Mulligan, A. A., Hen, R. and Schoppa, N. E. (2012) Mitral Cells in the Olfactory Bulb Are Mainly Excited through a Multistep Signaling Path. The Journal of Neuroscience, 32, 2964.

Giridhar, S., Doiron, B. and Urban, N. N. (2011) Timescale-dependent shaping of correlation by olfactory bulb lateral inhibition. Proceedings of the National Academy of Sciences, 108, 5843-5848.

Go, M. A., Mueller, M., Castañares, M. L., Egger, V. and Daria, V. R. (2019) A compact holographic projector module for high-resolution 3D multi-site two-photon photostimulation. Plos One, 14, e0210564.

Go, M. A., Stricker, C., Redman, S., Bachor, H.-A. and Daria, V. R. (2012) Simultaneous multi-site two-photon photostimulation in three dimensions. Journal of Biophotonics, 5, 745-753.

Go, M. A., To, M.-S., Stricker, C., Redman, S., Bachor, H.-A., Stuart, G. and Daria, V. (2013) Four-dimensional multi-site photolysis of caged neurotransmitters. Frontiers in Cellular Neuroscience, 7.

Golan, L., Reutsky, I., Farah, N. and Shoham, S. (2009) Design and characteristics of holographic neural photo-stimulation systems. Journal of Neural Engineering, 6, 066004.

Golding, N. L. and Spruston, N. (1998) Dendritic sodium spikes are variable triggers of axonal action potentials in hippocampal CA1 pyramidal neurons. Neuron, 21.

Grabe, V. and Sachse, S. (2018) Fundamental principles of the olfactory code. Biosystems, 164, 94-101.

Gracia-Llanes, F. J., Crespo, C., Blasco-Ibáñez, J. M., Nacher, J., Varea, E., Rovira-Esteban, L. and Martínez-Guijarro, F. J. (2010) GABAergic basal forebrain afferents innervate selectively GABAergic targets in the main olfactory bulb. Neuroscience, 170, 913-922.

Grienberger, C., Chen, X. and Konnerth, A. (2014) NMDA receptor-dependent multidendrite Ca(2+) spikes required for hippocampal burst firing in vivo. Neuron, 81, 1274-1281.

Grienberger, C. and Konnerth, A. (2012) Imaging calcium in neurons. Neuron, 73, 862-885.

Grimes, W. N., Zhang, J., Graydon, C. W., Kachar, B. and Diamond, J. S. (2010) Retinal parallel processors: more than 100 independent microcircuits operate within a single interneuron. Neuron, 65, 873-885.

Gschwend, O., Abraham, N. M., Lagier, S., Begnaud, F., Rodriguez, I. and Carleton, A. (2015) Neuronal pattern separation in the olfactory bulb improves odor discrimination learning. Nature Neuroscience, 18, 1474-+.

Halabisky, B. and Strowbridge, B. W. (2003) γ-Frequency Excitatory Input to Granule Cells Facilitates Dendrodendritic Inhibition in the Rat Olfactory Bulb. Journal of Neurophysiology, 90, 644-654.

Hall, B. J. and Delaney, K. R. (2002) Contribution of a calcium-activated non-specific conductance to NMDA receptor-mediated synaptic potentials in granule cells of the frog olfactory bulb. J Physiol, 543, 819-834.

Harris, K. and Stevens, J. (1989) Dendritic spines of CA 1 pyramidal cells in the rat hippocampus: serial electron microscopy with reference to their biophysical characteristics. The Journal of Neuroscience, 9, 2982-2997.

Harvey, C. D. and Svoboda, K. (2007) Locally dynamic synaptic learning rules in pyramidal neuron dendrites. Nature, 450, 1195-1200.

Hausser, M. (2001) Synaptic function: dendritic democracy. Curr Biol, 11, R10-12.

Hernandez, O., Papagiakoumou, E., Tanese, D., Fidelin, K., Wyart, C. and Emiliani, V. (2016) Three-dimensional spatiotemporal focusing of holographic patterns. Nature Communications, 7, 11928.

Hille, B. (2001) Ion channels of excitable membranes, Sinauer, Sunderland, Mass.

Horst, A. v. d. and Forde, N. R. (2008) Calibration of dynamic holographic optical tweezers for force measurements on biomaterials. Opt. Express, 16, 20987-21003.

Igarashi, K. M., Ieki, N., An, M., Yamaguchi, Y., Nagayama, S., Kobayakawa, K., Kobayakawa, R., Tanifuji, M., Sakano, H., Chen, W. R. and Mori, K. (2012) Parallel Mitral and Tufted Cell Pathways Route Distinct Odor Information to Different Targets in the Olfactory Cortex. Journal of Neuroscience, 32, 7970-7985.

Imai, T. (2014) Construction of functional neuronal circuitry in the olfactory bulb. Semin Cell Dev Biol, 35, 180-188.

Imai, T. and Sakano, H. (2007) Roles of odorant receptors in projecting axons in the mouse olfactory system. Curr Opin Neurobiol, 17, 507-515.

Imai, T. and Sakano, H. (2008) Odorant receptor-mediated signaling in the mouse. Curr Opin Neurobiol, 18, 251-260.

Inanobe, A., Fujita, A., Ito, M., Tomoike, H., Inageda, K. and Kurachi, Y. (2002) Inward rectifier K+ channel Kir2.3 is localized at the postsynaptic membrane of excitatory synapses. American Journal of Physiology-Cell Physiology, 282, C1396-C1403.

Isaacson, J. S. (1999) Glutamate spillover mediates excitatory transmission in the rat olfactory bulb. Neuron, 23, 377-384.

Isaacson, J. S. (2001) Mechanisms governing dendritic γ-aminobutyric acid (GABA) release in the rat olfactory bulb. Proceedings of the National Academy of Sciences, 98, 337-342.

Isaacson, J. S. and Strowbridge, B. W. (1998) Olfactory Reciprocal Synapses: Dendritic Signaling in the CNS. Neuron, 20, 749-761.

Isaacson, J. S. and Vitten, H. (2003) GABA(B) receptors inhibit dendrodendritic transmission in the rat olfactory bulb. J Neurosci, 23, 2032-2039.

Jerome, J. and Heck, D. (2011) The Age of Enlightenment: Evolving Opportunities in Brain Research Through Optical Manipulation of Neuronal Activity. Frontiers in Systems Neuroscience, 5.

Jonas, P., Racca, C., Sakmann, B., Seeburg, P. H. and Monyer, H. (1994) Differences in Ca2+ permeability of AMPA-type glutamate receptor channels in neocortical neurons caused by differential GluR-B subunit expression. Neuron, 12, 1281-1289.

Judkewitz, B., Roth, A. and Häusser, M. (2006) Dendritic Enlightenment: Using Patterned Two-Photon Uncaging to Reveal the Secrets of the Brain's Smallest Dendrites. Neuron, 50, 180-183.

Kamondi, A., Acsády, L. and Buzsáki, G. (1998) Dendritic Spikes Are Enhanced by Cooperative Network Activity in the Intact Hippocampus. The Journal of Neuroscience, 18, 3919-3928.

Kantevari, S., Matsuzaki, M., Kanemoto, Y., Kasai, H. and Ellis-Davies, G. C. (2010) Two-color, two-photon uncaging of glutamate and GABA. Nat Methods, 7, 123-125.

Kato, Hiroyuki K., Chu, Monica W., Isaacson, Jeffry S. and Komiyama, T. (2012) Dynamic Sensory Representations in the Olfactory Bulb: Modulation by Wakefulness and Experience. Neuron, 76, 962-975.

Kato, Hiroyuki K., Gillet, Shea N., Peters, Andrew J., Isaacson, Jeffry S. and Komiyama, T. (2013) Parvalbumin-Expressing Interneurons Linearly Control Olfactory Bulb Output. Neuron, 80, 1218-1231.

Katz, Y., Kath, W. L., Spruston, N. and Hasselmo, M. E. (2007) Coincidence detection of place and temporal context in a network model of spiking hippocampal neurons. PLoS Comput Biol, 3, e234.

Kawaguchi, Y., Karube, F. and Kubota, Y. (2005) Dendritic Branch Typing and Spine Expression Patterns in Cortical Nonpyramidal Cells. Cerebral Cortex, 16, 696-711.

Kay, L. M., Beshel, J., Brea, J., Martin, C., Rojas-Líbano, D. and Kopell, N. (2009) Olfactory oscillations: the what, how and what for. Trends in Neurosciences, 32, 207-214.

Kim, D. H., Chang, A. Y., McTavish, T. S., Patel, H. K. and Willhite, D. C. (2012a) Center-surround vs. distance-independent lateral connectivity in the olfactory bulb. Front Neural Circuits, 6, 34.

Kim, S., Guzman, S. J., Hu, H. and Jonas, P. (2012b) Active dendrites support efficient initiation of dendritic spikes in hippocampal CA3 pyramidal neurons. Nat Neurosci, 15, 600-606.

Kirkby, P. A., Srinivas Nadella, K. M. N. and Silver, R. A. (2010) A compact acousto-optic lens for 2D and 3D femtosecond based 2-photon microscopy. Opt. Express, 18, 13720-13744.

Klausberger, T., Márton, L. F., Baude, A., Roberts, J. D. B., Magill, P. J. and Somogyi, P. (2004) Spike timing of dendrite-targeting bistratified cells during hippocampal network oscillations in vivo. Nature Neuroscience, 7, 41-47.

Kollo, M., Holderith, N., Antal, M. and Nusser, Z. (2008) Unique clustering of A-type potassium channels on different cell types of the main olfactory bulb. Eur J Neurosci, 27, 1686-1699.

Kramer, R. H., Fortin, D. L. and Trauner, D. (2009) New photochemical tools for controlling neuronal activity. Current Opinion in Neurobiology, 19, 544-552.

Krueppel, R., Remy, S. and Beck, H. (2011) Dendritic integration in hippocampal dentate granule cells. Neuron, 71, 512-528.

Labarrera, C., London, M. and Angelo, K. (2013) Tonic inhibition sets the state of excitability in olfactory bulb granule cells. J Physiol, 591, 1841-1850.

Lage-Rupprecht, V., Zhou, L., Bianchini, G., Aghvami, S. S., Rózsa, B., Sassoé-Pognetto, M. and Egger, V. (2019) Local reciprocal release of GABA from olfactory bulb granule cell spines: Cooperation of conventional release mechanisms and NMDA receptors. bioRxiv, 440198.

Lagier, S., Carleton, A. and Lledo, P.-M. (2004) Interplay between Local GABAergic Interneurons and Relay Neurons Generates γ Oscillations in the Rat Olfactory Bulb. The Journal of Neuroscience, 24, 4382-4392.

Larkum, M. E., Nevian, T., Sandler, M., Polsky, A. and Schiller, J. (2009) Synaptic integration in tuft dendrites of layer 5 pyramidal neurons: a new unifying principle. Science, 325, 756-760.

Larkum, M. E., Waters, J., Sakmann, B. and Helmchen, F. (2007) Dendritic spikes in apical dendrites of neocortical layer 2/3 pyramidal neurons. J Neurosci, 27, 8999-9008.

Liesener, J., Reicherter, M., Haist, T. and Tiziani, H. J. (2000) Multi-functional optical tweezers using computer-generated holograms. Optics Communications, 185, 77-82.

Lillis, K. P., Eng, A., White, J. A. and Mertz, J. (2008) Two-photon imaging of spatially extended neuronal network dynamics with high temporal resolution. J Neurosci Methods, 172, 178-184.

Liu, A., Savya, S. and Urban, N. N. (2016a) Early Odorant Exposure Increases the Number of Mitral and Tufted Cells Associated with a Single Glomerulus. The Journal of Neuroscience, 36, 11646.

Liu, S., Puche, A. C. and Shipley, M. T. (2016b) The Interglomerular Circuit Potently Inhibits Olfactory Bulb Output Neurons by Both Direct and Indirect Pathways. The Journal of Neuroscience, 36, 9604.

Llinas, R. and Nicholson, C. (1971) Electrophysiological properties of dendrites and somata in alligator Purkinje cells. J Neurophysiol, 34, 532-551.

Lorincz, A. and Nusser, Z. (2010) Molecular identity of dendritic voltage-gated sodium channels. Science, 328, 906-909.

Losavio, B. E., Iyer, V. and Saggau, P. (2009) Two-photon microscope for multisite microphotolysis of caged neurotransmitters in acute brain slices. J Biomed Opt, 14, 064033.

Losonczy, A. and Magee, J. C. (2006) Integrative properties of radial oblique Dendrites in hippocampal CA1 pyramidal neurons. Neuron, 50, 291-307.

Losonczy, A., Makara, J. K. and Magee, J. C. (2008) Compartmentalized dendritic plasticity and input feature storage in neurons. Nature, 452, 436-441.

Ludwig, M. (2005) Dendritic neurotransmitter release, Springer, New York, NY.

Ludwig, M., Apps, D., Menzies, J., Patel, J. C. and Rice, M. E. (2016) Dendritic Release of Neurotransmitters. Compr Physiol, 7, 235-252.

Ludwig, M. and Pittman, Q. J. (2003) Talking back: dendritic neurotransmitter release. Trends Neurosci, 26, 255-261.

Lukas, M., Suyama, H. and Egger, V. (2019) Vasopressin Cells in the Rodent Olfactory Bulb Resemble Non-Bursting Superficial Tufted Cells and Are Primarily Inhibited upon Olfactory Nerve Stimulation. eNeuro, 6.

Luo, M. and Katz, L. C. (2001) Response Correlation Maps of Neurons in the Mammalian Olfactory Bulb. Neuron, 32, 1165-1179.

Lutz, C., Otis, T. S., DeSars, V., Charpak, S., DiGregorio, D. A. and Emiliani, V. (2008) Holographic photolysis of caged neurotransmitters. Nature Methods, 5, 821-827.

Maccaferri, G. and Dingledine, R. (2002) Control of Feedforward Dendritic Inhibition by NMDA Receptor-Dependent Spike Timing in Hippocampal Interneurons. The Journal of Neuroscience, 22, 5462-5472.

Macrides, F. and Schneider, S. P. (1982) Laminar organization of mitral and tufted cells in the main olfactory bulb of the adult hamster. J Comp Neurol, 208, 419-430.

Magee, J. C. and Cook, E. P. (2000) Somatic EPSP amplitude is independent of synapse location in hippocampal pyramidal neurons. Nat Neurosci, 3, 895-903.

Major, G., Larkum, M. E. and Schiller, J. (2013) Active properties of neocortical pyramidal neuron dendrites. Annu Rev Neurosci, 36, 1-24.

Makara, Judit K. and Magee, Jeffrey C. (2013) Variable Dendritic Integration in Hippocampal CA3 Pyramidal Neurons. Neuron, 80, 1438-1450.

Malnic, B., Godfrey, P. A. and Buck, L. B. (2004) The human olfactory receptor gene family. P Natl Acad Sci USA, 101, 2584-2589.

Malvaut, S., Gribaudo, S., Hardy, D., David, L. S., Daroles, L., Labrecque, S., Lebel-Cormier, M. A., Chaker, Z., Cote, D., De Koninck, P., Holzenberger, M., Trembleau, A., Caille, I. and Saghatelyan, A. (2017) CaMKII alpha Expression Defines Two Functionally Distinct Populations of Granule Cells Involved in Different Types of Odor Behavior. Current Biology, 27, 3315-+.

Manabe, H. and Mori, K. (2013) Sniff rhythm-paced fast and slow gamma-oscillations in the olfactory bulb: relation to tufted and mitral cells and behavioral states. Journal of Neurophysiology, 110, 1593-1599.

Manita, S., Miyakawa, H., Kitamura, K. and Murayama, M. (2017) Dendritic Spikes in Sensory Perception. Front Cell Neurosci, 11, 29.

Margrie, T. W., Sakmann, B. and Urban, N. N. (2001) Action potential propagation in mitral cell lateral dendrites is decremental and controls recurrent and lateral inhibition in the mammalian olfactory bulb. Proc Natl Acad Sci U S A, 98, 319-324.

Margrie, T. W. and Schaefer, A. T. (2003) Theta oscillation coupled spike latencies yield computational vigour in a mammalian sensory system. The Journal of physiology, 546, 363-374.

Markopoulos, F., Rokni, D., Gire, David H. and Murthy, Venkatesh N. (2012) Functional Properties of Cortical Feedback Projections to the Olfactory Bulb. Neuron, 76, 1175-1188.

Matsuzaki, M., Honkura, N., Ellis-Davies, G. C. and Kasai, H. (2004) Structural basis of long-term potentiation in single dendritic spines. Nature, 429, 761-766.

Mayer, M. L., Westbrook, G. L. and Guthrie, P. B. (1984) Voltage-dependent block by Mg2+ of NMDA responses in spinal cord neurones. Nature, 309, 261-263.

McGann, J. P. (2017) Poor human olfaction is a 19th-century myth. Science, 356, eaam7263.

Memmesheimer, R.-M. (2010) Quantitative prediction of intermittent high-frequency oscillations in neural networks with supralinear dendritic interactions. Proceedings of the National Academy of Sciences, 107, 11092-11097.

Meredith, M. (1988) Trigeminal Response to Odors. In Sensory Systems: II Springer, pp. 139-139.

Merkle, F. T., Fuentealba, L. C., Sanders, T. A., Magno, L., Kessaris, N. and Alvarez-Buylla, A. (2014) Adult neural stem cells in distinct microdomains generate previously unknown interneuron types. Nature Neuroscience, 17, 207-214.

Middendorf, W. H. (1965) Introductory network analysis, Allyn and Bacon.

Miyawaki, A., Llopis, J., Heim, R., McCaffery, J. M., Adams, J. A., Ikura, M. and Tsien, R. Y. (1997) Fluorescent indicators for Ca2+ based on green fluorescent proteins and calmodulin. Nature, 388, 882-887.

Moine, F., Brechbühl, J., Nenniger Tosato, M., Beaumann, M. and Broillet, M.-C. (2018) Alarm pheromone and kairomone detection via bitter taste receptors in the mouse Grueneberg ganglion. BMC Biology, 16, 12.

Mori, K., Manabe, H., Narikiyo, K. and Onisawa, N. (2013) Olfactory consciousness and gamma oscillation couplings across the olfactory bulb, olfactory cortex, and orbitofrontal cortex. Front Psychol, 4, 743.

Mori, K. and Sakano, H. (2011) How is the olfactory map formed and interpreted in the mammalian brain? Annu Rev Neurosci, 34, 467-499.

Mori, K. and Takagi, S. F. (1978) Activation and inhibition of olfactory bulb neurones by anterior commissure volleys in the rabbit. J Physiol, 279, 589-604.

Mori, K., Takahashi, Y. K., Igarashi, K. M. and Yamaguchi, M. (2006) Maps of odorant molecular features in the Mammalian olfactory bulb. Physiol Rev, 86, 409-433.

Nadella, K. M. N. S., Roš, H., Baragli, C., Griffiths, V. A., Konstantinou, G., Koimtzis, T., Evans, G. J., Kirkby, P. A. and Silver, R. A. (2016) Random-access scanning microscopy for 3D imaging in awake behaving animals. Nature Methods, 13, 1001-1004.

Nagayama, S., Homma, R. and Imamura, F. (2014) Neuronal organization of olfactory bulb circuits. Front Neural Circuits, 8, 98.

Nai, Q., Dong, H. W., Linster, C. and Ennis, M. (2010) Activation of α1 and α2 noradrenergic receptors exert opposing effects on excitability of main olfactory bulb granule cells. Neuroscience, 169, 882-892.

Najac, M., Sanz Diez, A., Kumar, A., Benito, N., Charpak, S. and De Saint Jan, D. (2015) Intraglomerular Lateral Inhibition Promotes Spike Timing Variability in Principal Neurons of the Olfactory Bulb. The Journal of Neuroscience, 35, 4319.

Naritsuka, H., Sakai, K., Hashikawa, T., Mori, K. and Yamaguchi, M. (2009) Perisomatic-Targeting Granule Cells in the Mouse Olfactory Bulb. Journal of Comparative Neurology, 515, 409-426.

Neant-Fery, M., Peres, E., Nasrallah, C., Kessner, M., Gribaudo, S., Greer, C., Didier, A., Trembleau, A. and Caille, I. (2012) A role for dendritic translation of CaMKIIalpha mRNA in olfactory plasticity. PLoS One, 7, e40133.

Nikolenko, V., Poskanzer, K. E. and Yuste, R. (2007) Two-photon photostimulation and imaging of neural circuits. Nature Methods, 4, 943-950.

Nikolenko, V., Watson, B., Araya, R., Woodruff, A., Peterka, D. and Yuste, R. (2008) SLM microscopy: scanless two-photon imaging and photostimulation using spatial light modulators. Frontiers in Neural Circuits, 2.

Nowak, L., Bregestovski, P., Ascher, P., Herbet, A. and Prochiantz, A. (1984) Magnesium gates glutamate-activated channels in mouse central neurones. Nature, 307, 462-465.

Nunes, D. and Kuner, T. (2015) Disinhibition of olfactory bulb granule cells accelerates odour discrimination in mice. Nature Communications, 6.

Nunes, D. and Kuner, T. (2018) Axonal sodium channel Na(V)1.2 drives granule cell dendritic GABA release and rapid odor discrimination. Plos Biology, 16.

Oettl, L.-L., Ravi, N., Schneider, M., Scheller, Max F., Schneider, P., Mitre, M., da Silva Gouveia, M., Froemke, Robert C., Chao, Moses V., Young, W. S., Meyer-Lindenberg, A., Grinevich, V., Shusterman, R. and Kelsch, W. (2016) Oxytocin Enhances Social Recognition by Modulating Cortical Control of Early Olfactory Processing. Neuron, 90, 609-621.

Ona-Jodar, T., Gerkau, N. J., Aghvami, S. S., Rose, C. R. and Egger, V. (2017) Two-Photon Na+ Imaging Reports Somatically Evoked Action Potentials in Rat Olfactory Bulb Mitral and Granule Cell Neurites. Frontiers in Cellular Neuroscience, 11.

Oron, D., Tal, E. and Silberberg, Y. (2005) Scanningless depth-resolved microscopy. Opt. Express, 13, 1468-1476.

Orona, E., Rainer, E. C. and Scott, J. W. (1984) Dendritic and Axonal Organization of Mitral and Tufted Cells in the Rat Olfactory-Bulb. Journal of Comparative Neurology, 226, 346-356.

Otopalik, A. G., Pipkin, J. and Marder, E. (2019) Neuronal morphologies built for reliable physiology in a rhythmic motor circuit. Elife, 8.

Palfi, D., Chiovini, B., Szalay, G., Kaszas, A., Turi, G. F., Katona, G., Abranyi-Balogh, P., Szori, M., Potor, A., Frigyesi, O., Haveland, C. L., Szadai, Z., Madarasz, M., Vasanits-Zsigrai, A., Molnar-Perl, I., Viskolcz, B., Csizmadia, I. G., Mucsi, Z. and Rozsa, B. (2018) High efficiency two-photon uncaging coupled by the correction of spontaneous hydrolysis. Org Biomol Chem, 16, 1958-1970.

Panhuber, H., Laing, D. G., Willcox, M. E., Eagleson, G. K. and Pittman, E. A. (1985) The distribution of the size and number of mitral cells in the olfactory bulb of the rat. J Anat, 140 (Pt 2), 297-308.

Payeur, A., Beique, J. C. and Naud, R. (2019) Classes of dendritic information processing. Curr Opin Neurobiol, 58, 78-85.

Peace, S. T., Johnson, B. C., Li, G., Kaiser, M. E., Fukunaga, I., Schaefer, A. T., Molnar, A. C. and Cleland, T. A. (2017) Coherent olfactory bulb gamma oscillations arise from coupling independent columnar oscillators. BioRxiv, 213827.

Pinato, G. and Midtgaard, J. (2005) Dendritic sodium spikelets and low-threshold calcium spikes in turtle olfactory bulb granule cells. J Neurophysiol, 93, 1285-1294.

Piskorowski, R. A. and Chevaleyre, V. (2012) Synaptic integration by different dendritic compartments of hippocampal CA1 and CA2 pyramidal neurons. Cell Mol Life Sci, 69, 75-88.

Poleg-Polsky, A., Ding, H. and Diamond, J. S. (2018) Functional Compartmentalization within Starburst Amacrine Cell Dendrites in the Retina. Cell Rep, 22, 2898-2908.

Pouille, F., McTavish, T. S., Hunter, L. E., Restrepo, D. and Schoppa, N. E. (2017) Intraglomerular gap junctions enhance interglomerular synchrony in a sparsely connected olfactory bulb network. The Journal of Physiology, 595, 5965-5986.

Pressler, R. T., Inoue, T. and Strowbridge, B. W. (2007) Muscarinic receptor activation modulates granule cell excitability and potentiates inhibition onto mitral cells in the rat olfactory bulb. Journal of Neuroscience, 27, 10969-10981.

Pressler, R. T. and Strowbridge, B. W. (2017) Direct Recording of Dendrodendritic Excitation in the Olfactory Bulb: Divergent Properties of Local and External Glutamatergic Inputs Govern Synaptic Integration in Granule Cells. J Neurosci, 37, 11774-11788.

Pressler, R. T. and Strowbridge, B. W. (2019) Functional specialization of interneuron dendrites: Identification of action potential initiation zone in axonless olfactory bulb granule cells. J Neurosci.

Price, J. L. and Powell, T. P. (1970a) An electron-microscopic study of the termination of the afferent fibres to the olfactory bulb from the cerebral hemisphere. J Cell Sci, 7, 157-187.

Price, J. L. and Powell, T. P. S. (1970b) Morphology of Granule Cells of Olfactory Bulb. J Cell Sci, 7, 91-&.

Quignon, P., Giraud, M., Rimbault, M., Lavigne, P., Tacher, S., Morin, E., Retout, E., Valin, A. S., Lindblad-Toh, K., Nicolas, J. and Galibert, F. (2005) The dog and rat olfactory receptor repertoires. Genome Biol, 6, R83.

Rall, W. (1969) Time Constants and Electrotonic Length of Membrane Cylinders and Neurons. Biophysical Journal, 9, 1483-1508.

Remy, S., Csicsvari, J. and Beck, H. (2009) Activity-dependent control of neuronal output by local and global dendritic spike attenuation. Neuron, 61, 906-916.

Rickgauer, J. P. and Tank, D. W. (2009) Two-photon excitation of channelrhodopsin-2 at saturation. Proceedings of the National Academy of Sciences, 106, 15025-15030.

Rinberg, D., Koulakov, A. and Gelperin, A. (2006) Speed-Accuracy Tradeoff in Olfaction. Neuron, 51, 351-358.

Rothermel, M. and Wachowiak, M. (2014) Functional imaging of cortical feedback projections to the olfactory bulb. Frontiers in neural circuits, 8, 73-73.

Royet, J. P., Distel, H., Hudson, R. and Gervais, R. (1998) A re-estimation of the number of glomeruli and mitral cells in the olfactory bulb of rabbit. Brain Research, 788, 35-42.

Saghatelyan, A., Roux, P., Migliore, M., Rochefort, C., Desmaisons, D., Charneau, P., Shepherd, G. M. and Lledo, P. M. (2005) Activity-dependent adjustments of the inhibitory network in the olfactory bulb following early postnatal deprivation. Neuron, 46, 103-116.

Sahay, A., Wilson, Donald A. and Hen, R. (2011) Pattern Separation: A Common Function for New Neurons in Hippocampus and Olfactory Bulb. Neuron, 70, 582-588.

Sakamoto, M., Ieki, N., Miyoshi, G., Mochimaru, D., Miyachi, H., Imura, T., Yamaguchi, M., Fishell, G., Mori, K., Kageyama, R. and Imayoshi, I. (2014) Continuous postnatal neurogenesis contributes to formation of the olfactory bulb neural circuits and flexible olfactory associative learning. J Neurosci, 34, 5788-5799.

Sato, K., Pellegrino, M., Nakagawa, T., Nakagawa, T., Vosshall, L. B. and Touhara, K. (2008) Insect olfactory receptors are heteromeric ligand-gated ion channels. Nature, 452, 1002-1006.

Scheuss, V. and Bonhoeffer, T. (2014) Function of dendritic spines on hippocampal inhibitory neurons. Cereb Cortex, 24, 3142-3153.

Schiller, J., Major, G., Koester, H. J. and Schiller, Y. (2000) NMDA spikes in basal dendrites of cortical pyramidal neurons. Nature, 404, 285-289.

Schoppa, N. E. (2006a) AMPA/Kainate Receptors Drive Rapid Output and Precise Synchrony in Olfactory Bulb Granule Cells. The Journal of Neuroscience, 26, 12996-13006.

Schoppa, N. E. (2006b) Synchronization of Olfactory Bulb Mitral Cells by Precisely Timed Inhibitory Inputs. Neuron, 49, 271-283.

Schoppa, N. E., Kinzie, J. M., Sahara, Y., Segerson, T. P. and Westbrook, G. L. (1998) Dendrodendritic Inhibition in the Olfactory Bulb Is Driven by NMDA Receptors. The Journal of Neuroscience, 18, 6790.

Schoppa, N. E. and Westbrook, G. L. (1999) Regulation of synaptic timing in the olfactory bulb by an A-type potassium current. Nat Neurosci, 2, 1106-1113.

Serizawa, S., Miyamichi, K. and Sakano, H. (2004) One neuron-one receptor rule in the mouse olfactory system. Trends Genet, 20, 648-653.

Shepherd, G. M. (1972) Synaptic organization of the mammalian olfactory bulb. Physiological Reviews, 52, 864-917.

Shepherd, G. M., Chen, W. R., Willhite, D., Migliore, M. and Greer, C. A. (2007) The olfactory granule cell: from classical enigma to central role in olfactory processing. Brain research reviews, 55, 373-382.

Shimomura, O., Johnson, F. H. and Saiga, Y. (1962) Extraction, purification and properties of aequorin, a bioluminescent protein from the luminous hydromedusan, Aequorea. J Cell Comp Physiol, 59, 223-239.

Shusterman, R., Smear, M. C., Koulakov, A. A. and Rinberg, D. (2011) Precise olfactory responses tile the sniff cycle. Nat Neurosci, 14, 1039-1044.

Skilling, H. H. (1965) Electrical engineering circuits.

Smith, S. L., Smith, I. T., Branco, T. and Hausser, M. (2013) Dendritic spikes enhance stimulus selectivity in cortical neurons in vivo. Nature, 503, 115-120.

Spruston, N. and Johnston, D. (1992) Perforated patch-clamp analysis of the passive membrane properties of three classes of hippocampal neurons. Journal of Neurophysiology, 67, 508-529.

Stroh, O., Freichel, M., Kretz, O., Birnbaumer, L., Hartmann, J. and Egger, V. (2012) NMDA receptor-dependent synaptic activation of TRPC channels in olfactory bulb granule cells. J Neurosci, 32, 5737-5746.

Stuart, G., Spruston, N. and Häusser, M. (2007) Dendrites, Oxford University Press, Oxford ; New York.

Stuart, G., Spruston, N. and Häusser, M. (2016) Dendrites, Oxford University Press, Oxford ;.

Stuart, G. J. and Spruston, N. (2015) Dendritic integration: 60 years of progress. Nat Neurosci, 18, 1713-1721.

Svoboda, K. and Yasuda, R. (2006) Principles of two-photon excitation microscopy and its applications to neuroscience. Neuron, 50, 823-839.

Tada, M., Takeuchi, A., Hashizume, M., Kitamura, K. and Kano, M. (2014) A highly sensitive fluorescent indicator dye for calcium imaging of neural activity in vitro and in vivo. European Journal of Neuroscience, 39, 1720-1728.

Takahashi, H., Yoshihara, S. and Tsuboi, A. (2018) The Functional Role of Olfactory Bulb Granule Cell Subtypes Derived From Embryonic and Postnatal Neurogenesis. Front Mol Neurosci, 11.

Tan, J., Savigner, A., Ma, M. and Luo, M. (2010) Odor Information Processing by the Olfactory Bulb Analyzed in Gene-Targeted Mice. Neuron, 65, 912-926.

Tanese, D., Weng, J. Y., Zampini, V., De Sars, V., Canepari, M., Rozsa, B., Emiliani, V. and Zecevic, D. (2017) Imaging membrane potential changes from dendritic spines using computer-generated holography. Neurophotonics, 4, 031211.

Thomas, D., Tovey, S. C., Collins, T. J., Bootman, M. D., Berridge, M. J. and Lipp, P. (2000) A comparison of fluorescent Ca2+ indicator properties and their use in measuring elementary and global Ca2+ signals. Cell Calcium, 28, 213-223.

Tran-Van-Minh, A., Abrahamsson, T., Cathala, L. and DiGregorio, D. A. (2016) Differential Dendritic Integration of Synaptic Potentials and Calcium in Cerebellar Interneurons. Neuron, 91, 837-850.

Tran-Van-Minh, A., Caze, R. D., Abrahamsson, T., Cathala, L., Gutkin, B. S. and DiGregorio, D. A. (2015) Contribution of sublinear and supralinear dendritic integration to neuronal computations. Front Cell Neurosci, 9, 67.

Traynelis, S. F., Wollmuth, L. P., McBain, C. J., Menniti, F. S., Vance, K. M., Ogden, K. K., Hansen, K. B., Yuan, H., Myers, S. J. and Dingledine, R. (2010) Glutamate receptor ion channels: structure, regulation, and function. Pharmacol Rev, 62, 405-496.

Trimmer, J. S. and Rhodes, K. J. (2004) Localization of voltage-gated ion channels in mammalian brain. Annu Rev Physiol, 66, 477-519.

Urban, N. N. and Arevian, A. C. (2009) Computing with dendrodendritic synapses in the olfactory bulb. Ann N Y Acad Sci, 1170, 264-269.

Urban, N. N. and Sakmann, B. (2002) Reciprocal intraglomerular excitation and intra- and interglomerular lateral inhibition between mouse olfactory bulb mitral cells. The Journal of Physiology, 542, 355-367.

VanDongen, A. M. (2009) Biology of the NMDA receptor, CRC Press, Boca Raton.

Vicini, S., Wang, J. F., Li, J. H., Zhu, W. J., Wang, Y. H., Luo, J. H., Wolfe, B. B. and Grayson, D. R. (1998) Functional and pharmacological differences between recombinant N-methyl-D-aspartate receptors. J Neurophysiol, 79, 555-566.

Wachowiak, M. (2011) All in a Sniff: Olfaction as a Model for Active Sensing. Neuron, 71, 962-973.

Walker, J. W., McCray, J. A. and Hess, G. P. (1986) Photolabile protecting groups for an acetylcholine receptor ligand. Synthesis and photochemistry of a new class of o-nitrobenzyl derivatives and their effects on receptor function. Biochemistry, 25, 1799-1805.

Wellis, D. P. and Scott, J. W. (1990) Intracellular responses of identified rat olfactory bulb interneurons to electrical and odor stimulation. Journal of Neurophysiology, 64, 932-947.

Whitesell, J. D., Sorensen, K. A., Jarvie, B. C., Hentges, S. T. and Schoppa, N. E. (2013) Interglomerular Lateral Inhibition Targeted on External Tufted Cells in the Olfactory Bulb. The Journal of Neuroscience, 33, 1552-1563.

Wilson, D. A. and Sullivan, R. M. (2011) Cortical processing of odor objects. Neuron, 72, 506-519.

Woolf, T. B. and Greer, C. A. (1994) Local communication within dendritic spines: models of second messenger diffusion in granule cell spines of the mammalian olfactory bulb. Synapse, 17, 247-267.

Woolf, T. B., Shepherd, G. M. and Greer, C. A. (1991a) Local information processing in dendritic trees: subsets of spines in granule cells of the mammalian olfactory bulb. J Neurosci, 11, 1837-1854.

Woolf, T. B., Shepherd, G. M. and Greer, C. A. (1991b) Serial reconstructions of granule cell spines in the mammalian olfactory bulb. Synapse, 7, 181-192.

y Cajal, S. R. (1904) Textura del sistema nervioso del hombre y de los vertebrados, Nicolás Moya.

Yamaguchi, M. and Mori, K. (2005) Critical period for sensory experience-dependent survival of newly generated granule cells in the adult mouse olfactory bulb. Proc Natl Acad Sci U S A, 102, 9697-9702.

Yang, S., Emiliani, V. and Tang, C.-M. (2014a) The kinetics of multibranch integration on the dendritic arbor of CA1 pyramidal neurons. Frontiers in Cellular Neuroscience, 8.

Yang, S., Papagiakoumou, E., Guillon, M., de Sars, V., Tang, C.-M. and Emiliani, V. (2011) Three-dimensional holographic photostimulation of the dendritic arbor. Journal of Neural Engineering, 8, 046002.

Yang, S., Yang, S., Moreira, T., Hoffman, G., Carlson, G. C., Bender, K. J., Alger, B. E. and Tang, C.-M. (2014b) Interlamellar CA1 network in the hippocampus. Proceedings of the National Academy of Sciences, 111, 12919-12924.

Yang, S. J., Allen, W. E., Kauvar, I., Andalman, A. S., Young, N. P., Kim, C. K., Marshel, J. H., Wetzstein, G. and Deisseroth, K. (2015) Extended field-of-view and increased-signal 3D holographic illumination with time-division multiplexing. Opt. Express, 23, 32573-32581.

Yang, W., Carrillo-Reid, L., Bando, Y., Peterka, D. S. and Yuste, R. (2018) Simultaneous two-photon imaging and two-photon optogenetics of cortical circuits in three dimensions. eLife, 7, e32671.

Zelles, T., Boyd, J. D., Hardy, A. B. and Delaney, K. R. (2006) Branch-specific Ca2+ influx from Na+-dependent dendritic spikes in olfactory granule cells. Journal of Neuroscience, 26, 30-40.

Zipfel, W. R., Williams, R. M. and Webb, W. W. (2003) Nonlinear magic: multiphoton microscopy in the biosciences. Nature Biotechnology, 21, 1369-1377.

7 Acknowledgements

First and foremost, I would like to thank my supervisor Prof. Dr. Veronica Egger for her valuable support, guidance, and advice throughout my work. She always had a sympathetic ear and did everything to provide an excellent work atmosphere on the professional as well as on the personal level.

I am no less thankful to every one of our working group AG Egger, namely Michael Lukas, Hajime Suyama, Fernando Perez, Wolfgang Bywalez & Vanessa Lage-Rupprecht for their valuable contributions to this work. I profoundly appreciate the plenty of discussions and conversations on all the topics of my work in the lab meetings and in the office. A very special thank you goes to Anne Pietryga-Krieger for her excellent technical assistance and her dedication to keep the lab running.

I thank my collaboration partners from the Australian National University and University of Teheran, namely Vincent Daria, Mary-Ann Go, Michael Castañares and Sara Aghvami, for the excellent and fruitful cooperation.

I sincerely thank Magdalena Meyer for her multi-site help in the final work on this thesis.

I would like to thank Prof. Dr. Joachim Ruther and Prof. Dr. Marc Spehr who mentored my work in the context of the Regensburg International Graduate School of Life Sciences.

I sincerely thank the whole AG Neumann, AG Flor and AG Egger for the friendly atmosphere in the lab and P.H. for the weekly beers.

I especially thank my mother and my family for all the support throughout my work on this thesis.